

COPERNICUS SPACE COMPONENT SENTINEL OPTICAL IMAGING
MISSION PERFORMANCE CLUSTER SERVICE

Data Quality Report

Sentinel-3 SLSTR - March 2023

OPT-MPC

Copernicus Sentinel



Optical Mission Performance Cluster

Ref.: OMPC.ACR.DQR.04.03-2023

Issue: 1.1

Date: 14/04/2023

Contract: 4000136252/21/I-BG

Customer: ESA	Document Ref.: OMPC.ACR.DQR.04.03-2023
Contract No.: 4000136252/21/I-BG	Date: 14/04/2023
	Issue: 1.1

Project:	COPERNICUS SPACE COMPONENT SENTINEL OPTICAL IMAGING MISSION PERFORMANCE CLUSTER SERVICE		
Title:	Data Quality Report - SLSTR - March 2023		
Author(s):	SLSTR ESL team		
Approved by:	S. Clerc, OPT-MPC ESL Coordinator	Authorized by	C. Henocq, OPT-MPC S3 Technical Manager
Distribution:	ESA, EUMETSAT, published in Sentinel Online		
Accepted by ESA	S. Dransfeld, ESA TO		
Filename	OMPC.ACR.DQR.04.03-2023 - i1r1 - SLSTR Data Quality Report March 2023.docx		

Disclaimer

The views expressed herein can in no way be taken to reflect the official opinion of the European Space Agency or the European Union.





Changes Log

Version	Date	Changes
1.0	12/04/2023	First version
1.1	14/04/2023	Updated version to take into account a few comments from ESA

Table of content

1	EXECUTIVE SUMMARY	1
2	PROCESSING STATUS	3
2.1	PROCESSING BASELINE STATUS	3
2.2	PROCESSING ANOMALIES.....	4
3	EVENTS AND INSTRUMENT ANOMALIES	5
3.1	SLSTR-A	5
3.2	SLSTR-B	6
4	INSTRUMENT STATUS	7
4.1	INSTRUMENT TEMPERATURES.....	8
4.1.1	SLSTR-A.....	8
4.1.2	SLSTR-B.....	9
4.2	DETECTOR TEMPERATURES	10
4.2.1	SLSTR-A.....	10
4.2.2	SLSTR-B.....	11
4.3	SCANNER PERFORMANCE	12
4.3.1	SLSTR-A.....	12
4.3.2	SLSTR-B.....	13
4.4	BLACK-BODIES	14
4.4.1	SLSTR-A.....	15
4.4.2	SLSTR-B.....	16
4.5	DETECTOR NOISE LEVELS	17
4.5.1	SLSTR-A VIS and SWIR channel signal-to-noise	17
4.5.2	SLSTR-B VIS and SWIR channel signal-to-noise	20
4.5.3	SLSTR-A TIR channel NEDT	20
4.5.4	SLSTR-B TIR channel NEDT.....	22
4.6	CALIBRATION FACTORS	25
4.6.1	VIS and SWIR radiometric response	25
4.6.2	SLSTR-A.....	25
4.6.3	SLSTR-B.....	27
5	LEVEL-1 PRODUCT VALIDATION	30
5.1	LEVEL-1 TIR RADIOMETRIC VALIDATION	30
5.2	LEVEL- 1 VIS SWIR RADIOMETRIC VALIDATION	30
5.2.1	S3ETRAC latest mission trend SLSTR-A and SLSTR-B	31
5.2.2	Radiometric validation with DIMITRI	36
5.3	LEVEL-1 GEOMETRIC VALIDATION.....	41
5.3.1	SLSTR-A.....	42
5.3.2	SLSTR-B.....	43
6	LEVEL 2 LST VALIDATION	44
6.1	CATEGORY-A VALIDATION	44
6.2	CATEGORY-C VALIDATION	47
6.3	LEVEL-3C ASSESSMENT	50



6.4 REFERENCES 51

7 LEVEL 2 FRP VALIDATION52

7.1 INTRODUCTION 52

7.2 NIGHT-TIME VALIDATION..... 54

7.3 DAY-TIME VALIDATION..... 61

7.4 BIOME INFLUENCE 67

8 APPENDIX A70

List of Figures

Figure 1: OME temperature trends for SLSTR-A (left) and Baffle temperature trends (right) during March 2023. The OME plot shows the three paraboloid stops and flip baffle (top two plots) and optical bench at different positions (third plots), and scanner and flip assembly (bottom plots). The Baffle plot shows the temperature at different positions on the inner and outer baffles. Each dot represents the average temperature in one orbit. The discontinuity on March 7th is linked to a lunar calibration manoeuvre. ---- 8

Figure 2: SLSTR-B OME temperature trends (left) and Baffle temperature trends (right) during March 2023. The OME plot shows the three paraboloid stops and flip baffle (top two plots) and optical bench at different positions (third plots), and scanner and flip assembly (bottom plots). The Baffle plot shows the temperature at different positions on the inner and outer baffles. Each dot represents the average temperature in one orbit. ----- 9

Figure 3: SLSTR-A detector temperatures for each channel for the last year of operations. The vertical dashed lines indicate the start of each month. Each dot represents the average temperature in one orbit. The different colours indicate different detectors.----- 10

Figure 4: SLSTR-B detector temperatures for each channel for the last year of operations. The vertical dashed lines indicate the start of each month. Each dot represents the average temperature in one orbit. The different colours indicate different detectors. The discontinuity on 24th of February is linked to an on-board anomaly and subsequent decontamination. ----- 11

Figure 5: SLSTR-A scanner and flip jitter for March 2023, showing mean and stddev from expected position per orbit (red and blue respectively) for the nadir view (left) and oblique view (right). The plots show the nadir scanner (top), oblique scanner (middle) and flip mirror (bottom).----- 12

Figure 6: SLSTR-B scanner and flip jitter for March 2023, showing mean and stddev difference from expected position per orbit (red and blue respectively) for the nadir view (left) and oblique view (right). The plots show the nadir scanner (top), oblique scanner (middle) and flip mirror (bottom). ----- 13

Figure 7: SLSTR-A and SLSTR-B long term trends in average +YBB temperature, showing yearly variation. The vertical dashed lines indicate the 1st January in each year.----- 14

Figure 8: SLSTR-A blackbody temperature and baseplate gradient trends during March 2023 measured by different sensors at various positions in the BB and Baseplate. Each dot represents the average temperature in one orbit. ----- 15

Figure 9: SLSTR-B blackbody temperature and baseplate gradient trends during March 2023 measured by different sensors at various positions in the BB and Baseplate. Each dot represents the average temperature in one orbit. ----- 16

Figure 10: VIS channel signal-to-noise of the measured VISICAL signal in each orbit for the last year of operations for SLSTR-A. Different colours indicate different detectors. The vertical dashed lines indicate the start of each month. ----- 18

Figure 11. SWIR channel signal-to-noise of the measured VISICAL signal in each orbit for the last year of operations for SLSTR-A. Different colours indicate different detectors. The vertical dashed lines indicate the start of each month. ----- 19

Figure 12: SLSTR-A NEDT trend for the thermal channels in March 2023. Blue points were calculated from the cold blackbody signal and red points from the hot blackbody. The square symbols show results calculated from the nadir view and crosses show results from the oblique view. Results are plotted for all detectors and integrators, which is why there are several different levels within the same colour points (particularly for S8 and F2). ----- 21

Figure 13: SLSTR-B NEDT trend for the thermal channels in March 2023. Blue points were calculated from the cold blackbody signal and red points from the hot blackbody. The square symbols show results calculated from the nadir view and crosses show results from the oblique view. Results are plotted for all detectors and integrators, which is why there are several different levels within the same colour points (particularly for S8 and F2). ----- 23

Figure 14: Variation of the radiometric gain derived from the VISCAL signals for SLSTR-A VIS channels for the last year of operations (nadir view). Different colours represent different detectors. The vertical dashed lines indicate the start of each month. ----- 26

Figure 15: Variation of the radiometric gain derived from the VISCAL signals for SLSTR-A SWIR channels for the last year of operations (nadir view). Different colours represent different detectors. The vertical dashed lines indicate the start of each month. ----- 27

Figure 16: Variation of the radiometric gain derived from the VISCAL signals for SLSTR-B VIS channels for the past year (nadir view). Different colours represent different detectors. The vertical dashed lines indicate the start of each month. ----- 28

Figure 17: Variation of the radiometric gain derived from the VISCAL signals for SLSTR-B SWIR channels for the past year (nadir view). Different colours represent different detectors. The vertical dashed lines indicate the start of each month. ----- 29

Figure 18: Daytime combined SLSTR-A and SLSTR-B Level-1 image for visible channels on 30th March 2023. ----- 30

Figure 19: Ratio of SLSTR-A and OLCI-A radiances (red) and SLSTR-B and OLCI-B radiances (blue) for the visible channels in Nadir view using combined results for all desert sites. ----- 33

Figure 20: Ratio of SLSTR-A (red) and SLSTR-B (blue) with AATSR radiances in Nadir view using combined results for all desert sites. ----- 34

Figure 21: Ratio of SLSTR-A (red) and SLSTR-B (blue) with MODIS radiances in Nadir view using combined results for all desert sites. ----- 35

Figure 22: Time-series of the elementary ratios (observed/simulated) signal from SLSTR-A for (top to bottom) bands S02 and S03 respectively over March 2017- March 2023 from the six PICS Cal/Val sites. Dashed-green and orange lines indicate the 2% and 5% respectively. Error bars indicate the desert methodology uncertainty. ----- 37

Figure 23: Time-series of the elementary ratios (observed/simulated) signal from SLSTR-B for (top to bottom) bands S02 and S03 respectively over June 2018- March 2023 from the six PICS Cal/Val sites. Dashed-green and orange lines indicate the 2% and 5% respectively. Error bars indicate the desert methodology uncertainty. ----- 38

Figure 24: The estimated gain values for SLSTR-A and SLSTR-B over the 6 PICS sites identified by CEOS over the period March 2017- March 2023 and June 2018- March 2023 respectively as a function of wavelength. Dashed-green and orange lines indicate the 2% and 5% respectively. Error bars indicate the desert methodology uncertainty.----- 39

Figure 25: The estimated gain values for SLSTR-A and SLSTR-B from Glint, Rayleigh and PICS methods over the period March 2016- Feb-March 2023 and June 2018- Feb-March 2023 respectively as a function of wavelength. We use the gain value of S02 from Desert-PICS method as reference gain for Glint method. Dashed-green and orange lines indicate the 2% and 5% respectively. Error bars indicate the method uncertainties. ----- 40

Figure 26: Ratio of observed TOA reflectance to simulated one for (black) MERIS, (pale-green) S2A/MSI, (white) S2B/MSI, (blue) S3A/OLCI, (green) S3B/OLCI, (red) S3A/SLSTR-NADIR, and (cyan) S3B/SLSTR-NADIR averaged over the six PICS test sites over different periods as a function of wavelength.----- 41

Figure 27: SLSTR-A daily offset results in km from the GeoCal Tool analysis for Nadir along- and across-track (top two plots) and Oblique along- and across-track (bottom two plots) for March 2023. The error bars show the standard deviation. ----- 42

Figure 28: SLSTR-B daily offset results in km from the GeoCal Tool analysis for Nadir along- and across-track (top two plots) and Oblique along- and across-track (bottom two plots) for March 2023. The error bars show the standard deviation. ----- 43

Figure 29: Validation of the SL_2_LST product in December 2022 for SLSTR-A (left) and SLSTR-B (right) at seven Gold Standard in situ stations of the SURFRAD network plus two Gold Standard station from the ARM network. The matchups are split between daytime (red) and night-time (blue). ----- 47

Figure 30: Areas of high fire activity selected for the inter-comparison. The base map shows night-time fires detected by SLSTR (top) and MODIS (bottom) for the months of January, February and March 2023. ----- 56

Figure 31: Night-time fires detected by Sentinel 3A (top) and Sentinel 3B (bottom) for the months of January, February and March 2022. ----- 57

Figure 32: Cluster formation for a specific area. See text for details.----- 58

Figure 33: Scatterplot between the number of fires detected by both sensors (night-time). SLSTR values are reported on the x-axis, whereas MODIS ones are on the y-axis. ----- 59

Figure 34: Distribution of the FRP for fire clusters detected by both sensors. The lines represent kernel density estimates (KDE) computed over the bar plot.----- 60

Figure 35: Scatterplot between the FRP of fire clusters detected by both sensors. SLSTR values are reported on the x-axis, whereas MODIS ones are on the y-axis. The regression line (with a shaded 0.05 confidence interval) is obtained with a robust linear method (RLM), which is less affected by outliers. The scatter points are color-coded according to their cluster number, so that they can be traced back to the original datasets. R = 0.940, slope of regression line = 0.875.----- 60

Figure 36: Areas of high fire activity selected for the inter-comparison. The base map shows day-time fires detected by SLSTR (top) and MODIS (bottom) for the months of January, February and March 2023. -- 63

Figure 37: Day-time fires detected by Sentinel 3A (top) and Sentinel 3B (bottom) for the months of January, February and March 2023. ----- 64

Figure 38: Scatterplot between the number of fires clusters detected by both sensors (day-time). SLSTR values are reported on the x-axis, whereas MODIS ones are on the y-axis. ----- 65

Figure 39: Scatterplot between the FRP of fire clusters detected by both sensors. SLSTR values are reported on the x-axis, whereas MODIS ones are on the y-axis. The regression line (with a shaded 0.05 confidence interval) is obtained with a robust linear method (RLM), which is less affected by outliers.- 65

Figure 40: Scatterplot between the FRP of fire clusters detected by both sensors (close-up for FRP < 800 MW). SLSTR values are reported on the x-axis, whereas MODIS ones are on the y-axis. R = 0.810, slope of regression line = 0.775.----- 66

Figure 41: SLSTR vs MODIS clusters (FRP < 200) comparisons with regression line – night-time (left) and day-time (right).----- 66

Figure 42: Global Land Cover 2000 detailed biome definition.----- 69

List of Tables

Table 1: Average SLSTR-A reflectance factor, and signal-to-noise ratio of the measured VISCAL signal for the last 11 months, averaged over all detectors for the nadir view.-----	17
Table 2: Average SLSTR-A reflectance factor, and signal-to-noise ratio of the measured VISCAL signal for the last 11 months, averaged over all detectors for the oblique view. -----	17
Table 3: Average SLSTR-B reflectance factor, and signal-to-noise ratio of the measured VISCAL signal for the last 11 months, averaged over all detectors for the nadir view.-----	20
Table 4: Average SLSTR-B reflectance factor, and signal-to-noise ratio of the measured VISCAL signal for the last 11 months, averaged over all detectors for the oblique view. -----	20
Table 5: NEDT for SLSTR-A in the last 11 months averaged over all detectors for both Earth views towards the hot +YBB (top) and the cold -YBB (bottom). -----	22
Table 6: NEDT for SLSTR-B in the last 11 months averaged over all detectors for both Earth views towards the hot +YBB (top) and the cold -YBB (bottom). -----	24
Table 7. The recommended corrections that should be applied to SLSTR-A and SLSTR-B VIS, SWIR channels.-----	31
Table 8. A year-by-year breakdown of the drift in % since the start of the mission for SLSTR-A Note the trends for S6 are based on comparisons with MODIS-Aqua which are limited to June-July where the geometry matches.-----	31
Table 9. A year-by-year breakdown of the drift in % since the start of the mission for SLSTR-B. Note the trends for S6 are based on comparisons with MODIS-Aqua which are limited to June-July where the geometry matches. Furthermore, the drift for S6 is relative to 2019 comparisons. For SLSTR-B the reference measurements were obtained before an update to the flight calibration coefficients that was performed after the S3B-IOCR. A correction factor of 2.4% has been applied to the drift rates to account for the update. -----	32
Table 10: Average absolute accuracy in K of the SL_2_LST product with respect to Gold Standard stations for December 2022.-----	44
Table 11: Summary of the inter-comparison between night-time SLSTR FRP and MODIS FRP – January, February and March 2023. Results from previous comparison obtained between October and December 2022, July and August 2022, April and May 2022 with FRP V2 have been added respectively in the second, third and fourth column for information and comparison. -----	54
Table 12: Summary of the inter-comparison between SLSTR FRP and MODIS FRP – January, February and March 2023. Results from previous comparison obtained between October and December 2022, July and August 2022, April and May 2022 with FRP V2 have been added respectively in the second, third and fourth column for information and comparison. -----	61
Table 13: Summary of the biome index detection (number of fire clusters and FRP) between SLSTR FRP and MODIS FRP for day-time and night-time data – January, February and March 2023. Detailed definition of the biomes is provided in Figure 42 below.-----	68

1 Executive Summary

This section provides a summary of the data quality for SLSTR-A and SLSTR-B over the month of operation.

Any relevant formal instrument data requirements are added under the subsequent section headers for reference.

Each month the data measured by SLSTR-A and SLSTR-B are checked for quality and it is determined whether they meet the requirements specified in Sentinel-3 Mission Requirements Document, using the methods in the Sentinel-3 Cal-Val Plan.

A summary of the status from each check performed is provided below. A traffic light system is used, where the categories are determined as follows

- ❖ Gray indicates no change over the reporting period
- ❖ Green indicates that aspect is performing optimally
- ❖ Amber indicates there are some issues noted that may affect data quality or availability this month, or a user correction that needs to be applied
- ❖ Red indicates a significant quality issue, or instrument anomaly for some of the month

Follow the link on each topic header for more detailed information contained in this document.

Topic	Instrument	Comments
Processing Baseline Version	S3A	
	S3B	
Event	S3A	Several events occurred this month without impact on data quality
	S3B	Several events occurred this month without impact on data quality
Instrument Status	S3A	
	S3B	
Level-1 TIR Radiometric Validation	S3A	
	S3B	
Level- 1 VIS SWIR Radiometric Validation	S3A	Vicarious validation indicates calibration offsets need to be applied to the VIS/SWIR channels
	S3B	Vicarious validation indicates calibration offsets need to be applied to the VIS/SWIR channels
Level-1 Geometric Validation	S3A	
	S3B	
Level 2 LST validation	S3A	Validation results partially updated
	S3B	Validation results partially updated

**Data Quality Report – Sentinel-3 SLSTR
March 2023**

Topic	Instrument	Comments
Level 2 FRP validation	S3A	Validation results updated for Q1 2023
	S3B	Validation results updated for Q1 2023

2 Processing status

2.1 Processing baseline status

The Processing Baseline Version allows traceability of any changes to the software used to process the SLSTR products, and any updates to the auxiliary data files used to generate them.

The processing baseline identifier is now provided in the manifest file and in the global attributes of each file. The identifier comprises of seven characters (e.g. SL__L1_) which indicates the product type, and seven characters to indicate its version, xxx.yy.zz (e.g. 004.04.00). The version number, xxx indicates baseline collection, yy indicates change due to the IPF or ADF and zz indicates change in system components (e.g. L0, PUG) that do not impact data quality but are included to allow full traceability.

Summary information on the current PB version is provided below. More details of the processing baseline version can be found in the SLSTR Product Notice [[Latest Level-1 Product Notice](#), [Latest L2 Land Surface Temperature Product Notice](#)], which is released each time the processing baseline is updated.

IPF	IPF / Processing Baseline version	Date of deployment
S3A		
SL1	06.20 / SL__L1_.004.05.00	12/12/2022
SL2 LST	06.21 / SL__LST.004.07.00	23/08/2022
SL2 FRP (NTC)	01.08 / FRP_NTC.004.08.00	23/08/2022

IPF	IPF / Processing Baseline version	Date of deployment
S3B		
SL1	06.20 / SL__L1_.004.05.00	10/01/2023
SL2 LST	06.21 / SL__LST.004.07.00	05/09/2022
SL2 FRP (NTC)	01.08 / FRP_NTC.004.08.00	09/09/2022

No delivery or deployment occurred this month. The Processing Baselines of S3A and S3B are aligned with the latest processing baseline version.

 <p>OPT-MPC Copernicus Sentinel Optical Mission Performance Cluster</p>	<p>Optical MPC</p> <p>Data Quality Report – Sentinel-3 SLSTR</p> <p>March 2023</p>	<p>Ref.: OMPC.ACR.DQR.04.03-2023</p> <p>Issue: 1.1</p> <p>Date: 14/04/2023</p> <p>Page: 4</p>
---	---	---

2.2 Processing anomalies

On 4th March, several pointing errors have been detected over a full orbit on S3A SLSTR oblique view. These pointing errors, due to the “Scan Mirror Integrated” test, were affecting around 1.4% of SLSTR pixels over 1 PDU and were not linked to any manoeuvre. However, despite this failed test, data quality was not affected.

There have been no anomalies on data quality within the reported period.

	<p>Optical MPC</p> <p>Data Quality Report – Sentinel-3 SLSTR</p> <p>March 2023</p>	<p>Ref.: OMPC.ACR.DQR.04.03-2023</p> <p>Issue: 1.1</p> <p>Date: 14/04/2023</p> <p>Page: 5</p>
---	---	---

3 Events and instrument anomalies

Any events that have occurred in this month that cause significant data gaps and impact on quality are reported here.

Some background to the typical events that might occur are provided below

- ❖ **RFI Radio Frequency Interference** occurs when another satellite causes the data downlink to the receiving station to be interrupted, and the data is lost.
- ❖ **Scheduled manoeuvres** may take place for Lunar views for calibration purposes, collision avoidance, or to maintain the nominal orbit. Will often result in the pointing flag being raised, and the geolocation accuracy is not nominal during this time.
- ❖ **Blackbody cross over tests** occur approximately once per year and the hot and cold blackbodies are swapped round for instrument testing.
- ❖ **De-icing** occurs when the instrument is heated to remove the build-up of ice.

3.1 SLSTR-A

SLSTR-A was switched on and operating nominally during March 2023, with Scan Unit Electronics (SUE) scanning and autonomous switching between day and night modes, except for the following events:

- ❖ 1st March 2023, 08:28 - 09:09 – pointing flag raised due to in-plane manoeuvre.
- ❖ 7th March 2023, 21:23 – 8th March 2023, 00:42 – pointing flag raised and data gaps due to Lunar calibration.
- ❖ 14th March 2023, 09:47 – 10:04 – pointing flag raised due to in-plane manoeuvre.
- ❖ 16th March 2023, 17:39 – 17:45 – data gaps
- ❖ 17th March 2023, 07:07 – 07:19 – data gaps
- ❖ 26th March 2023, 21:33 – 21:39 – data gaps due to RFI

 <p>OPT-MPC Optical Mission Performance Cluster</p>	<p>Optical MPC</p> <p>Data Quality Report – Sentinel-3 SLSTR</p> <p>March 2023</p>	<p>Ref.: OMPC.ACR.DQR.04.03-2023 Issue: 1.1 Date: 14/04/2023 Page: 6</p>
---	---	---

3.2 SLSTR-B

SLSTR-B was switched on and operating nominally during March 2023, with SUE scanning and autonomous switching between day and night modes, except for the following events.

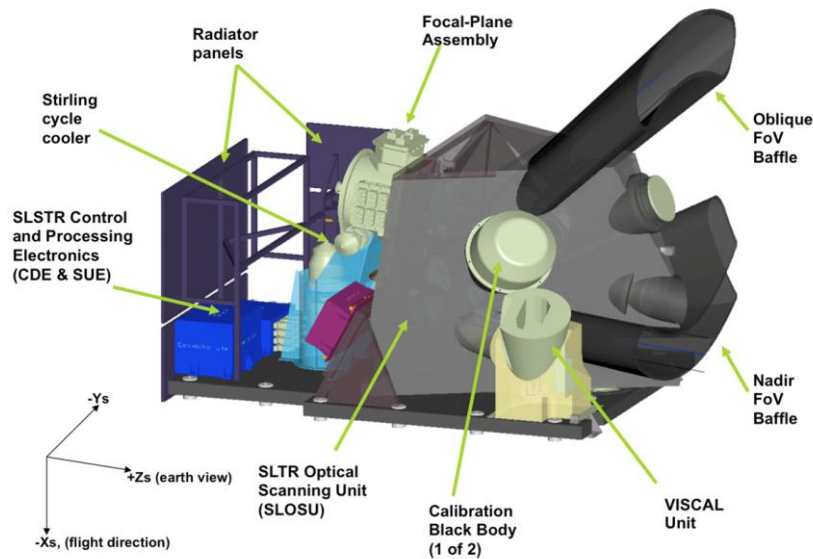
- ❖ 7th March 2023, 07:13 – 07:28 – pointing flag raised due to in-plane manoeuvre.
- ❖ 12th March 2023, 17:28 – 17:31 – data gaps
- ❖ 13th March 2023, 15:53 – 18:11 – pointing flag raised due to in-plane manoeuvre.
- ❖ 14th March 2023, 21:32 – 22:11 – data gaps due to RFI
- ❖ 22nd March 2023, 08:57 – 09:11 – pointing flag raised due to in-plane manoeuvre.
- ❖ 23rd March 2023, 09:27 – 09:33 – data gaps due to RFI
- ❖ 24th March 2023, 03:10 – 03:13 – data gaps
- ❖ 26th March 2023, 17:26 – 17:29 – data gaps
- ❖ 27th March 2023, 09:26 – 09:32 – data gaps due to RFI

4 Instrument Status

The health of the instrument impacts the data quality. This section contains in depth analysis of several instrument parameters over the month of operation, and in some cases, the latest annual and mission trends for context.

SLSTR is a scanning radiometer, and uses two black bodies for thermal calibration, and a VISCAL unit for visible and shortwave IR calibration via the Sun. The key instrument properties that are monitored include:

- ❖ instrument temperature of the baffles
- ❖ instrument temperature of the Optical Mechanical Enclosure (optical bench, flip mirror and scan mirror, internal baffles)
- ❖ detector temperatures
- ❖ scanner and flip mirror performance



A CDE Double Bit Flip anomaly occurred on 24/02 on SLSTR-B. Similar anomalies have been encountered in the past and have no impact on data quality. However, the power cycle and subsequent decontamination led to a 2-day data gap.

SLSTR-A behaved nominally during the reporting period.

4.1 Instrument temperatures

As a thermal infrared instrument, thermal stability and uniformity of the optical mechanical enclosure (OME) is critical to the radiometric calibration. In this section we show the orbital average temperature of the OME and instrument baffles during the month. We expect to see a very small daily variation in temperature superimposed on a stable level over the month.

4.1.1 SLSTR-A

Figure 1 shows the orbital average temperature of the OME and instrument baffles for SLSTR-A during the month. The temperature profiles show a discontinuity on March 7th which can be explained by the lunar calibration manoeuvre occurring at that time.

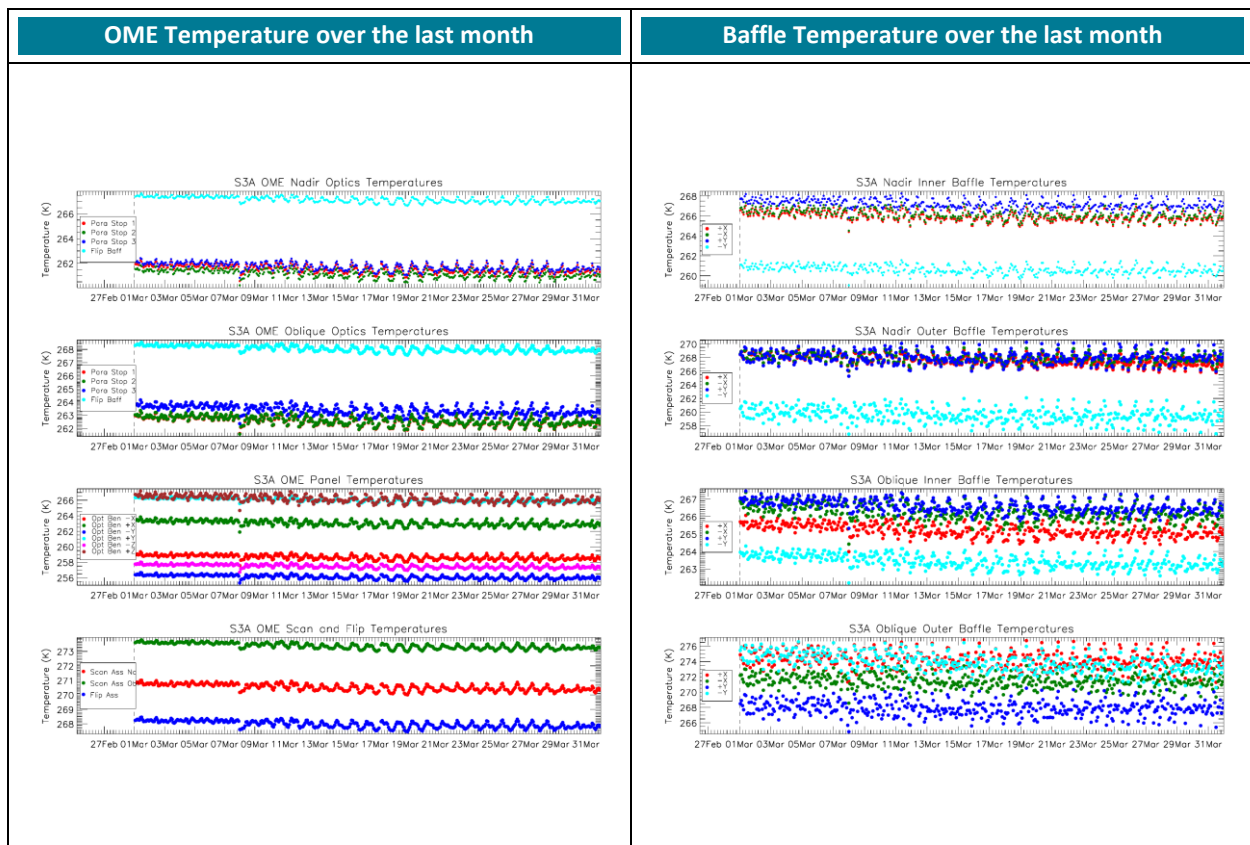


Figure 1: OME temperature trends for SLSTR-A (left) and Baffle temperature trends (right) during March 2023. The OME plot shows the three paraboloid stops and flip baffle (top two plots) and optical bench at different positions (third plots), and scanner and flip assembly (bottom plots). The Baffle plot shows the temperature at different positions on the inner and outer baffles. Each dot represents the average temperature in one orbit. The discontinuity on March 7th is linked to a lunar calibration manoeuvre.

4.1.2 SLSTR-B

Figure 2 shows the orbital average temperature of the OME and instrument baffles for SLSTR-B during the month. The temperatures were stable (on top of a daily variation cycle).

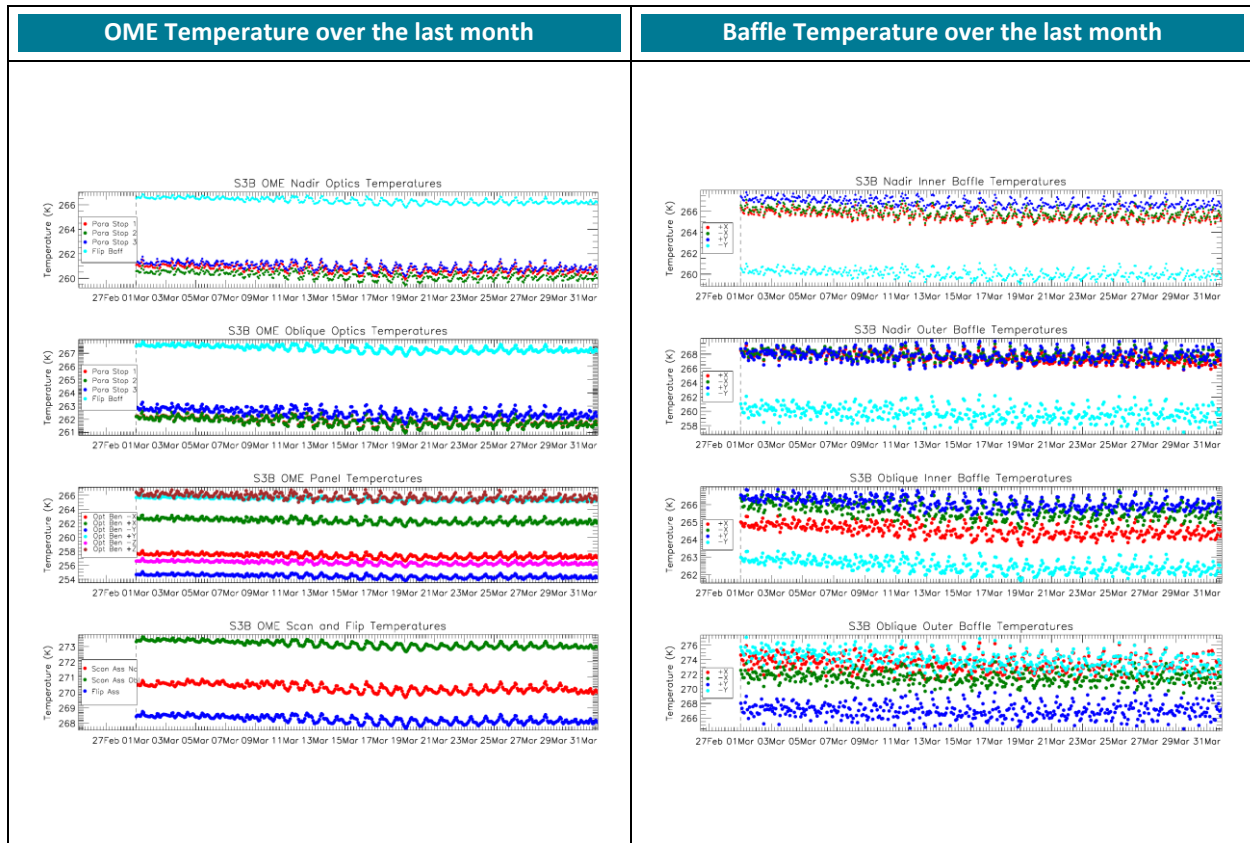


Figure 2: SLSTR-B OME temperature trends (left) and Baffle temperature trends (right) during March 2023. The OME plot shows the three paraboloid stops and flip baffle (top two plots) and optical bench at different positions (third plots), and scanner and flip assembly (bottom plots). The Baffle plot shows the temperature at different positions on the inner and outer baffles. Each dot represents the average temperature in one orbit.

4.2 Detector temperatures

The detector temperatures for both SLSTR-A and SLSTR-B were stable at their expected values over the month.

4.2.1 SLSTR-A

Figure 3 shows the annual trend in SLSTR-A detector temperatures for the past year. The temperatures from this month are consistent with the yearly trend.

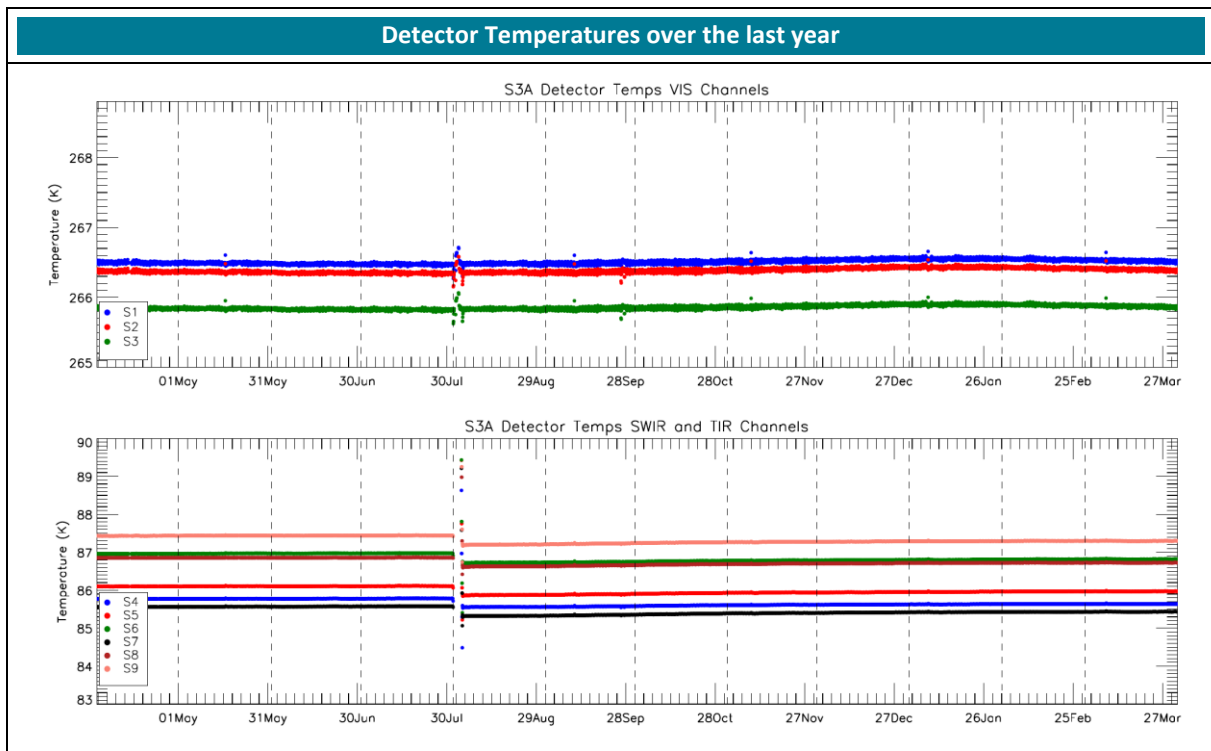


Figure 3: SLSTR-A detector temperatures for each channel for the last year of operations. The vertical dashed lines indicate the start of each month. Each dot represents the average temperature in one orbit. The different colours indicate different detectors.

4.2.2 SLSTR-B

Figure 4 shows the annual trend in SLSTR-B detector temperatures for the past year. The temperatures from this month are consistent with the yearly trend. The impact of the on-board anomaly and decontamination of the 24th of February is visible on the plot.

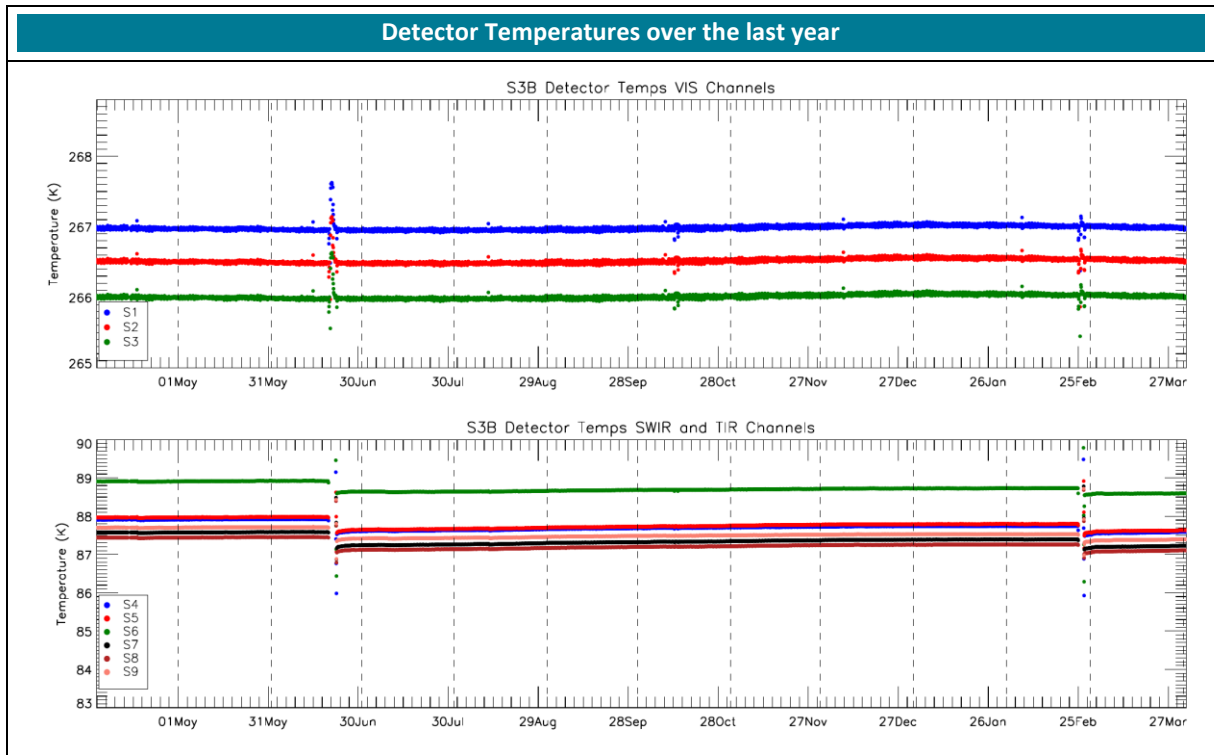


Figure 4: SLSTR-B detector temperatures for each channel for the last year of operations. The vertical dashed lines indicate the start of each month. Each dot represents the average temperature in one orbit. The different colours indicate different detectors. The discontinuity on 24th of February is linked to an on-board anomaly and subsequent decontamination.

4.3 Scanner performance

The actual position of the scan and flip mirrors is measured by the instrument, and in this section we show the statistics of the difference from the expected linear control law for each mirror in each view during March 2023. The performance has been consistent with previous operations and does not appear to be degrading. For reference, one arcsecond corresponds to roughly 4 m on the ground.

4.3.1 SLSTR-A

Figure 5 shows the statistics of the difference from the expected linear control law for each mirror in each view for SLSTR-A during March 2023.

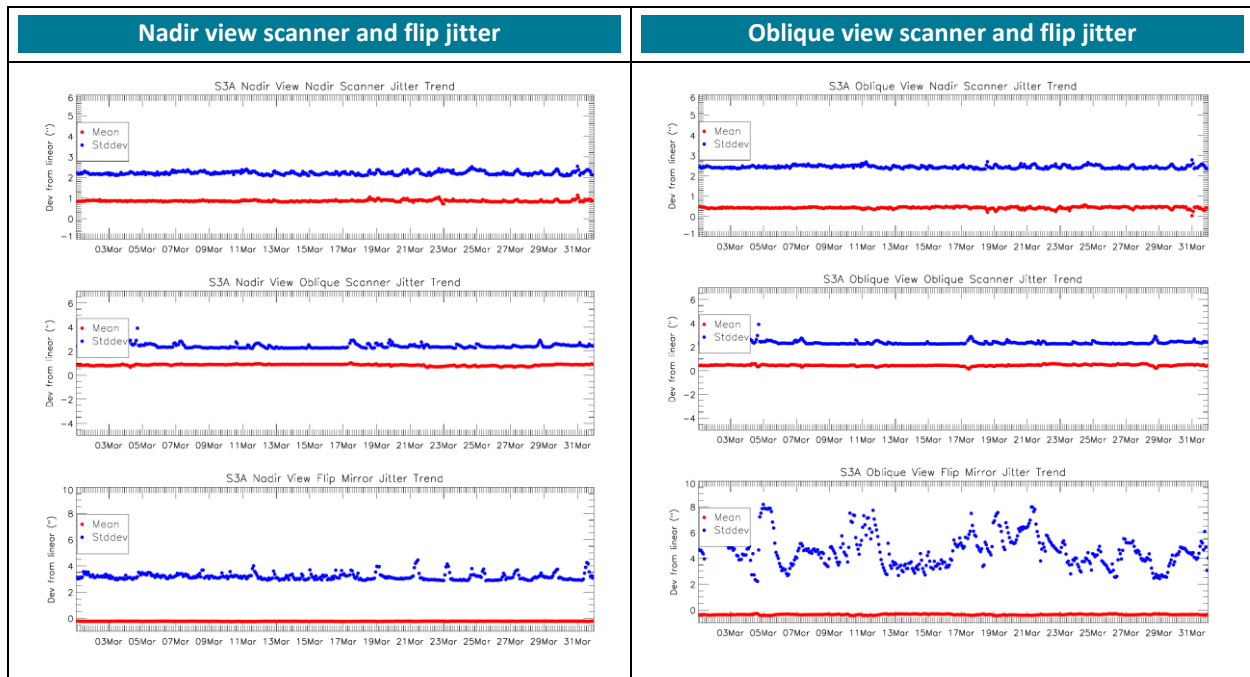


Figure 5: SLSTR-A scanner and flip jitter for March 2023, showing mean and stddev from expected position per orbit (red and blue respectively) for the nadir view (left) and oblique view (right). The plots show the nadir scanner (top), oblique scanner (middle) and flip mirror (bottom).

4.3.2 SLSTR-B

Figure 6 shows the statistics of the difference from the expected linear control law for each mirror in each view for SLSTR-B during March 2023.

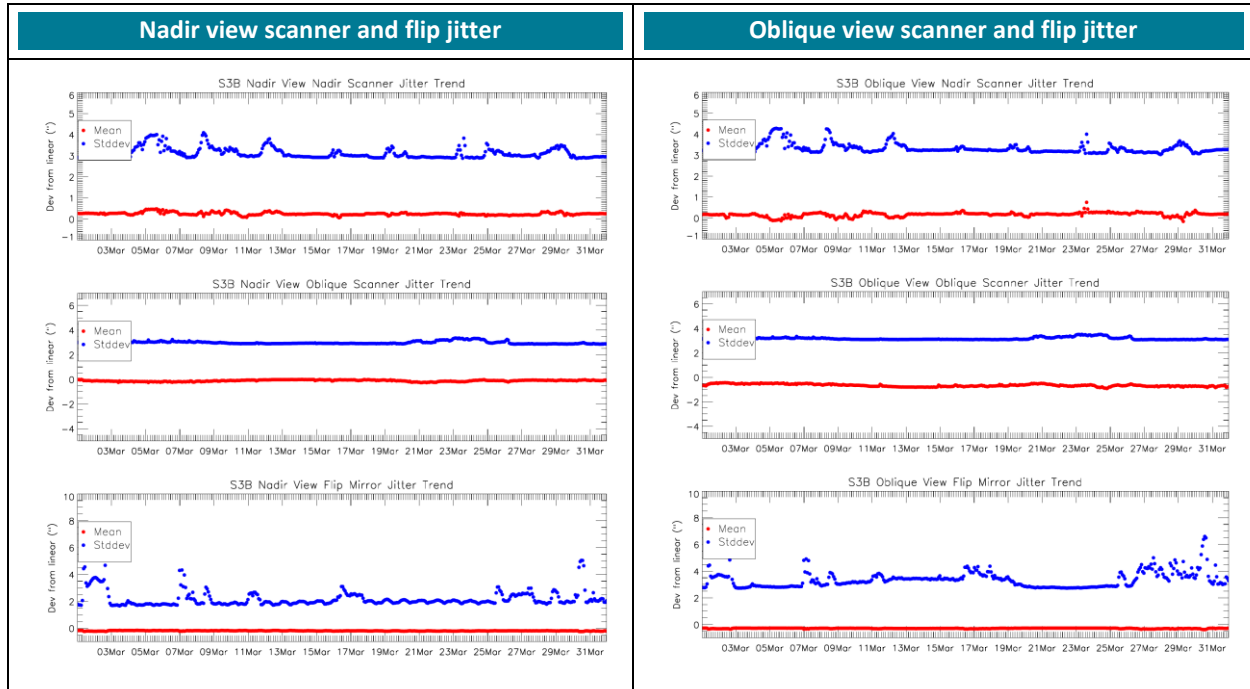


Figure 6: SLSTR-B scanner and flip jitter for March 2023, showing mean and stddev difference from expected position per orbit (red and blue respectively) for the nadir view (left) and oblique view (right). The plots show the nadir scanner (top), oblique scanner (middle) and flip mirror (bottom).

4.4 Black-Bodies

The monthly orbital average blackbody temperatures are shown in this section. The temperatures were stable on top of a daily variation cycle. There are also longer term trends which show a yearly variation, with temperatures rising as the Earth approaches perihelion at the beginning of January – this variation is shown in the monthly averages in Figure 7 and Table 5.

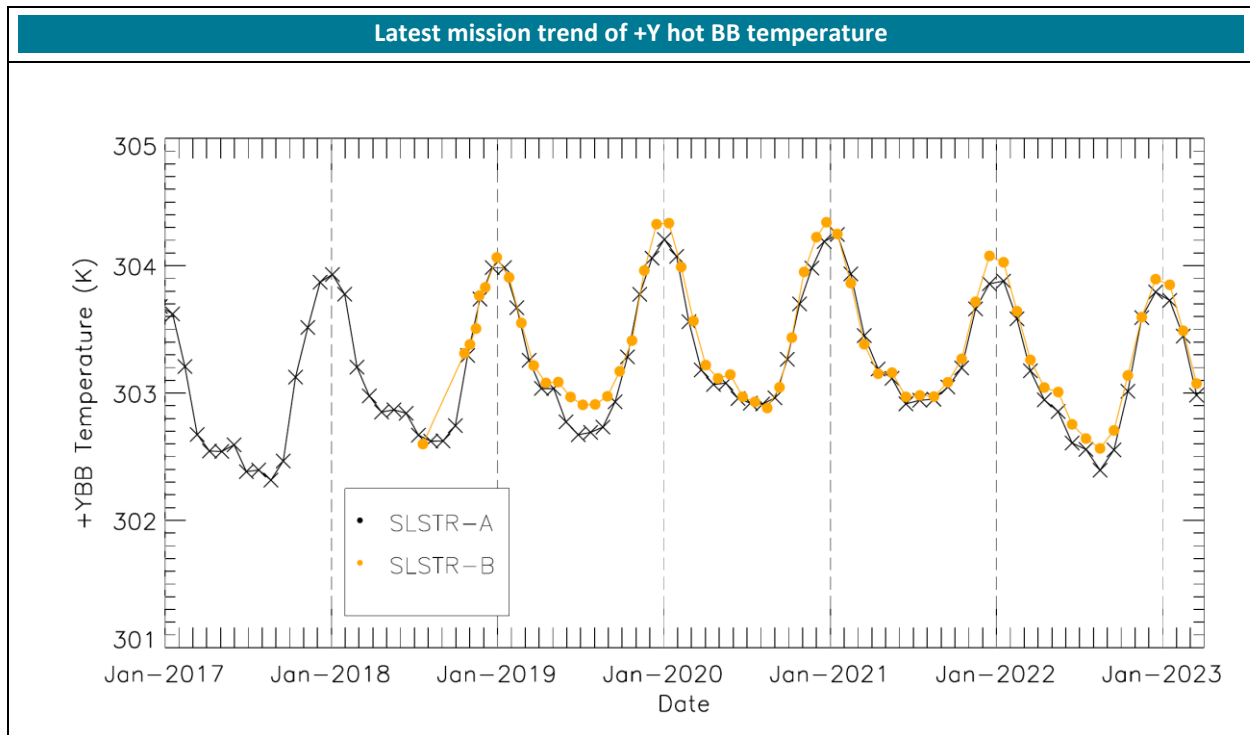


Figure 7: SLSTR-A and SLSTR-B long term trends in average +YBB temperature, showing yearly variation. The vertical dashed lines indicate the 1st January in each year.

4.4.1 SLSTR-A

The monthly orbital average blackbody temperatures for SLSTR-A are shown in Figure 8. The temperatures were stable on top of a daily variation cycle. Figure 8 also shows the gradients across the blackbody baseplate (i.e. each Platinum Resistance Thermometer (PRT) sensor reading relative to the mean). The gradients are stable and within their expected range of $\pm 20\text{mK}$. A small discontinuity can be seen on the 8th of March likely due to the lunar calibration manoeuvre.

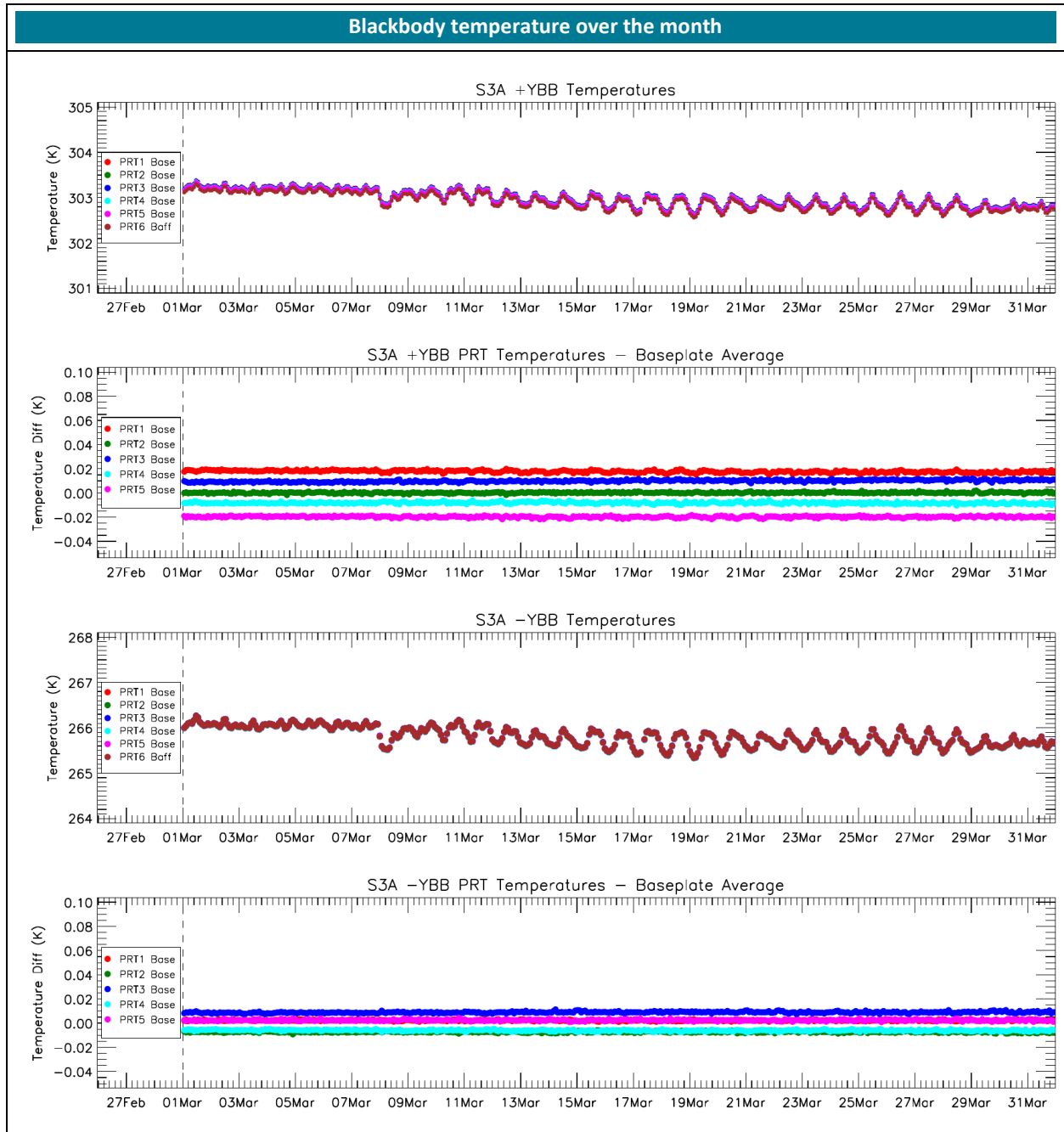


Figure 8: SLSTR-A blackbody temperature and baseplate gradient trends during March 2023 measured by different sensors at various positions in the BB and Baseplate. Each dot represents the average temperature in one orbit.

4.4.2 SLSTR-B

The monthly orbital average blackbody temperatures for SLSTR-B are shown in Figure 9. The temperatures were stable on top of a daily variation cycle. Figure 9 also shows the gradients across the blackbody baseplate (i.e. each Platinum Resistance Thermometer (PRT) sensor reading relative to the mean). The gradients are stable and within their expected range of $\pm 20\text{mK}$, except for the +Y blackbody for SLSTR-B which has a higher gradient. This higher gradient is expected and consistent with measurements made before launch.

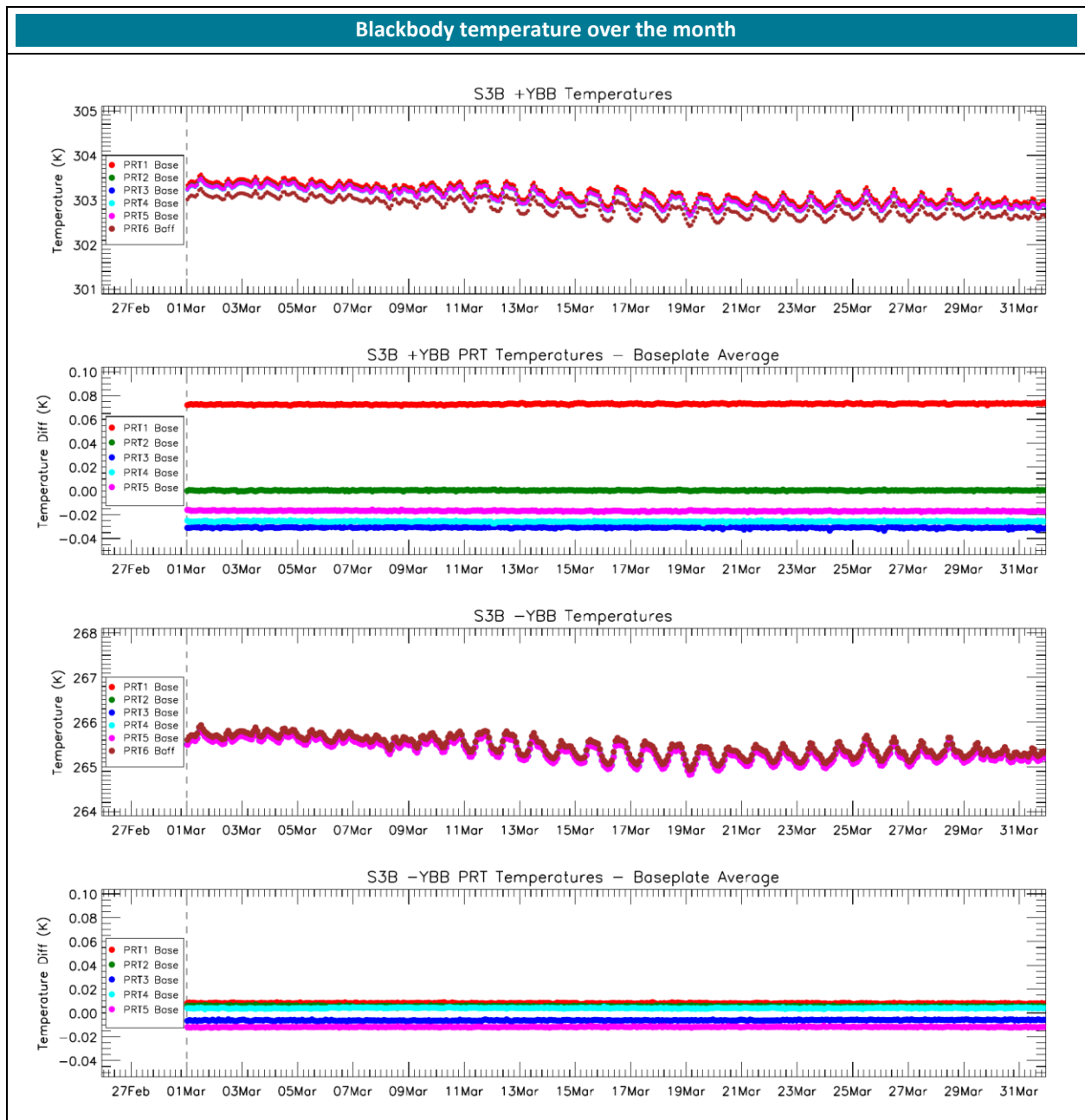


Figure 9: SLSTR-B blackbody temperature and baseplate gradient trends during March 2023 measured by different sensors at various positions in the BB and Baseplate. Each dot represents the average temperature in one orbit.

4.5 Detector noise levels

4.5.1 SLSTR-A VIS and SWIR channel signal-to-noise

The VIS and SWIR channel noise for SLSTR-A during March 2023 was stable and consistent with previous operations - the signal-to-noise ratio of the measured VISCAL signal over the past year is plotted in Figure 10 and Figure 11. Table 1 and Table 2 give the average monthly signal-to-noise (excluding the instrument decontaminations). These values average over the significant detector-detector dispersion for the SWIR channels that is shown in Figure 11. Note that these averages are now calculated for each calendar month, whereas in data quality reports before January 2022 they were aligned to the satellite 27 day repeat cycles.

Table 1: Average SLSTR-A reflectance factor, and signal-to-noise ratio of the measured VISCAL signal for the last 11 months, averaged over all detectors for the nadir view.

	Average Reflectance Factor	Nadir Signal-to-noise ratio										
		May 2022	Jun 2022	Jul 2022	Aug 2022	Sep 2022	Oct 2022	Nov 2022	Dec 2022	Jan 2023	Feb 2023	Mar 2023
S1	0.187	238	234	238	237	239	246	245	239	239	239	242
S2	0.194	243	242	242	241	241	245	248	246	246	243	241
S3	0.190	226	222	221	225	222	224	226	228	231	229	225
S4	0.191	170	167	167	168	171	171	172	173	174	172	171
S5	0.193	282	281	280	281	283	285	286	286	291	289	284
S6	0.175	180	179	179	181	183	183	184	186	187	185	183

Table 2: Average SLSTR-A reflectance factor, and signal-to-noise ratio of the measured VISCAL signal for the last 11 months, averaged over all detectors for the oblique view.

	Average Reflectance Factor	Oblique Signal-to-noise ratio										
		May 2022	Jun 2022	Jul 2022	Aug 2022	Sep 2022	Oct 2022	Nov 2022	Dec 2022	Jan 2023	Feb 2023	Mar 2023
S1	0.166	252	243	248	251	253	264	267	262	259	259	262
S2	0.170	254	249	257	257	256	262	269	271	268	262	260
S3	0.168	229	221	223	227	224	226	231	236	238	235	232
S4	0.166	138	135	137	137	139	139	139	140	139	138	138
S5	0.166	213	207	213	213	216	215	217	215	211	209	214
S6	0.155	131	130	130	131	133	132	133	133	131	129	131

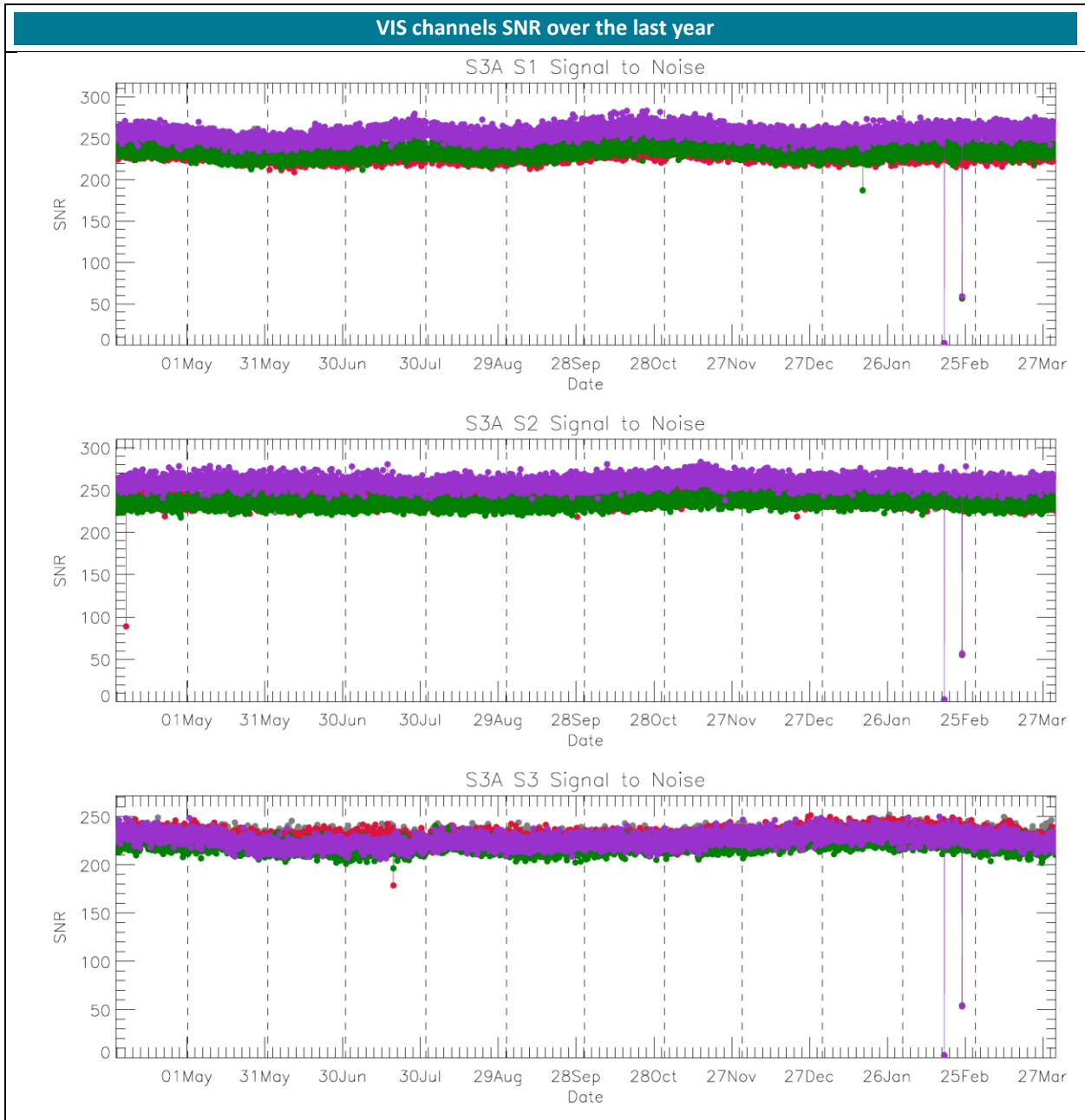


Figure 10: VIS channel signal-to-noise of the measured VISCAL signal in each orbit for the last year of operations for SLSTR-A. Different colours indicate different detectors. The vertical dashed lines indicate the start of each month.

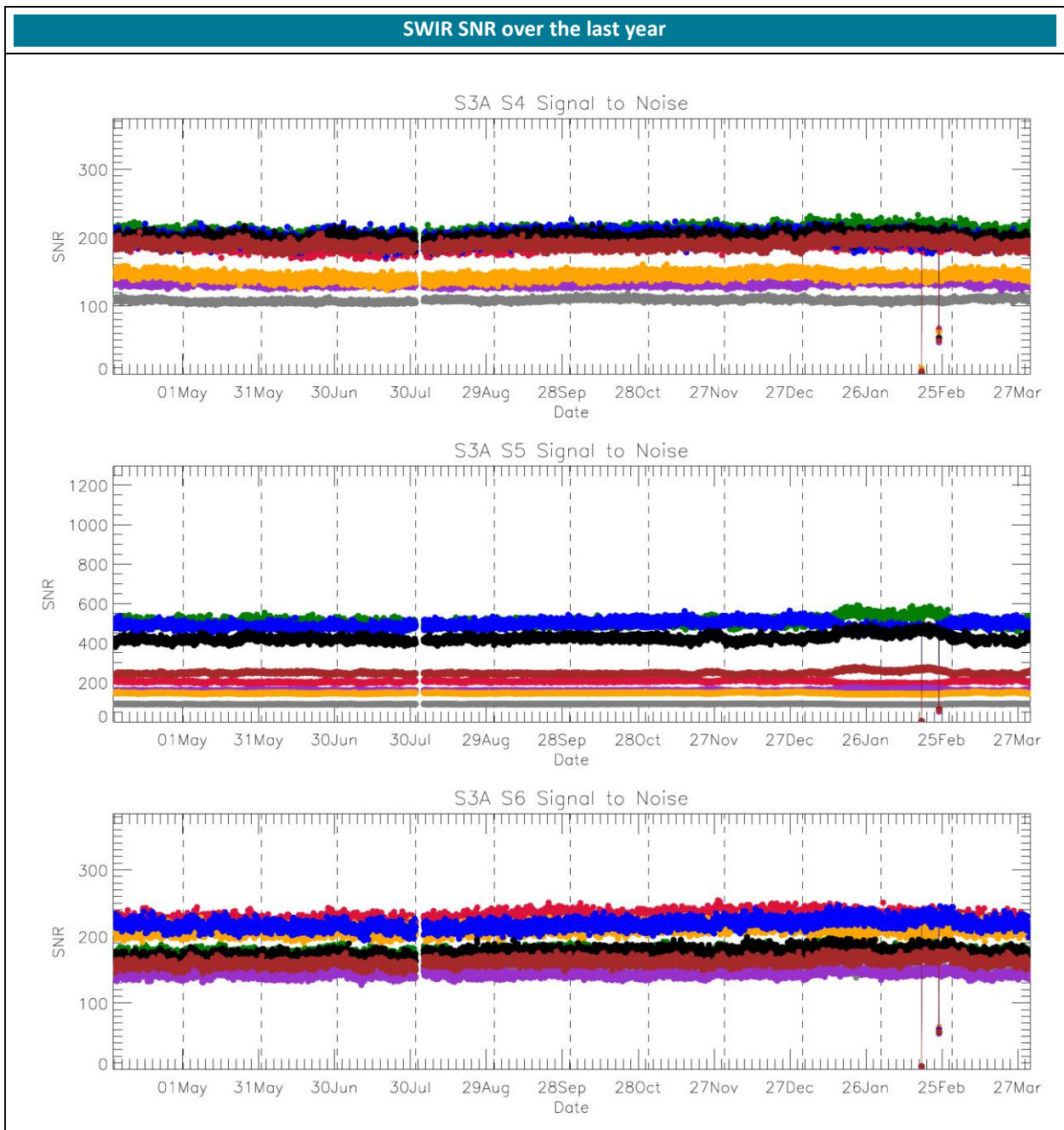


Figure 11. SWIR channel signal-to-noise of the measured VISCAL signal in each orbit for the last year of operations for SLSTR-A. Different colours indicate different detectors. The vertical dashed lines indicate the start of each month.

4.5.2 SLSTR-B VIS and SWIR channel signal-to-noise

The monthly average VIS and SWIR channel signal-to-noise ratios for SLSTR-B are shown in Table 3 and Table 4. These values average over a significant detector-detector dispersion for the SWIR channels.

Table 3: Average SLSTR-B reflectance factor, and signal-to-noise ratio of the measured VISCAL signal for the last 11 months, averaged over all detectors for the nadir view.

	Average Reflectance Factor	Nadir Signal-to-noise ratio										
		May 2022	Jun 2022	Jul 2022	Aug 2022	Sep 2022	Oct 2022	Nov 2022	Dec 2022	Jan 2023	Feb 2023	Mar 2023
S1	0.177	225	221	224	225	226	233	220	232	238	238	223
S2	0.192	215	214	213	218	218	218	256	223	221	221	218
S3	0.194	222	217	214	219	223	224	248	221	223	226	222
S4	0.186	130	127	127	127	127	127	129	131	131	130	129
S5	0.184	241	238	237	239	239	240	251	243	242	243	243
S6	0.162	160	158	157	159	158	157	162	163	165	165	162

Table 4: Average SLSTR-B reflectance factor, and signal-to-noise ratio of the measured VISCAL signal for the last 11 months, averaged over all detectors for the oblique view.

	Average Reflectance Factor	Oblique Signal-to-noise ratio										
		May 2022	Jun 2022	Jul 2022	Aug 2022	Sep 2022	Oct 2022	Nov 2022	Dec 2022	Jan 2023	Feb 2023	Mar 2023
S1	0.157	213	211	214	213	217	224	220	224	228	222	217
S2	0.168	247	243	241	248	246	249	256	257	256	255	251
S3	0.172	242	235	234	243	249	250	248	250	253	253	248
S4	0.168	128	124	126	127	129	129	129	133	132	131	131
S5	0.172	247	246	248	248	248	247	251	252	251	251	251
S6	0.152	181	178	182	183	184	185	187	189	188	186	188

4.5.3 SLSTR-A TIR channel NEDT

The thermal channel NEDT values for SLSTR-A in March 2023 are consistent with previous operations and within the requirements. NEDT trends calculated from the hot and cold blackbody signals are shown in Figure 12. Monthly NEDT values, averaged over all detectors and both Earth views, are shown in Table 5.

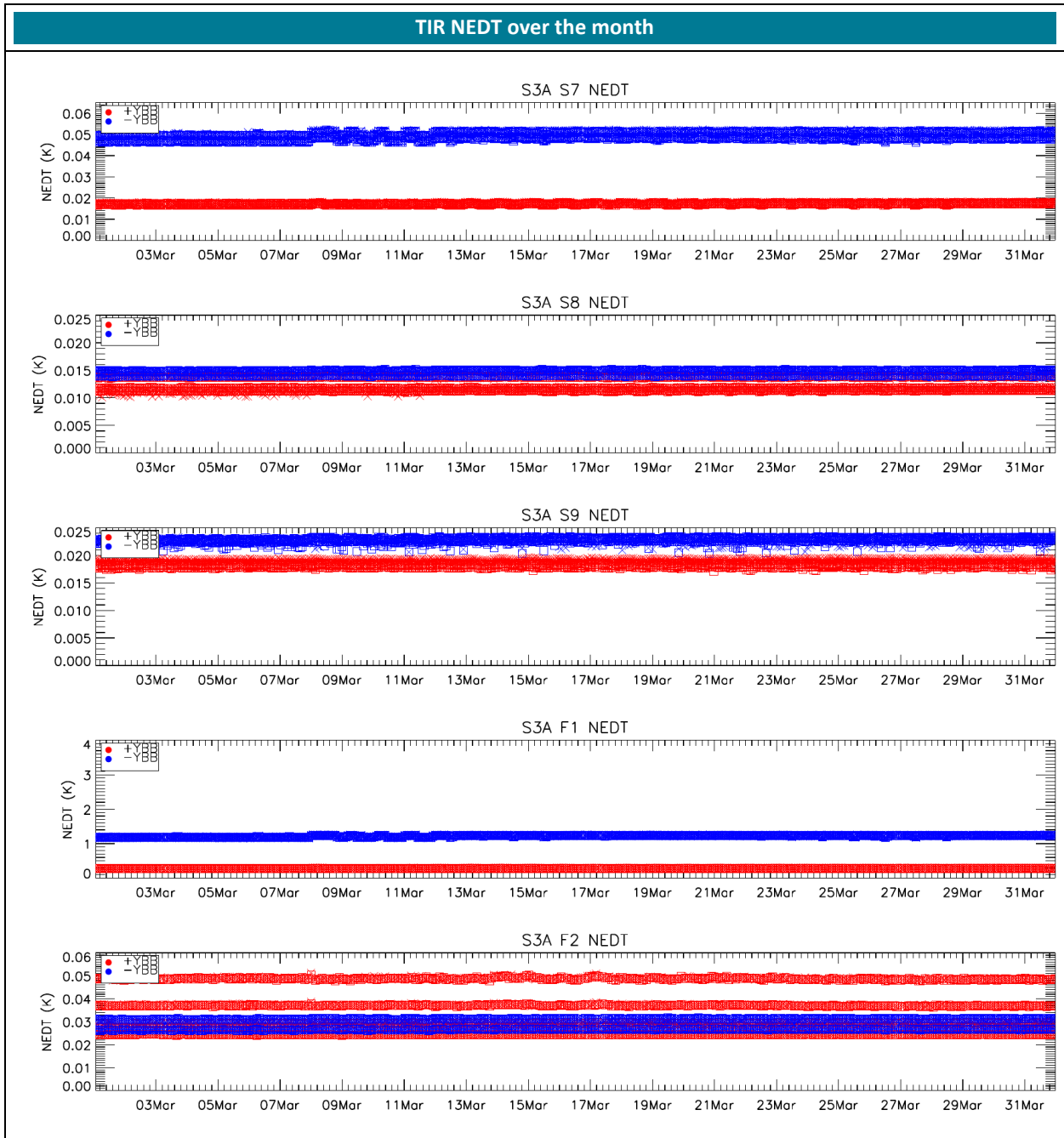


Figure 12: SLSTR-A NEDT trend for the thermal channels in March 2023. Blue points were calculated from the cold blackbody signal and red points from the hot blackbody. The square symbols show results calculated from the nadir view and crosses show results from the oblique view. Results are plotted for all detectors and integrators, which is why there are several different levels within the same colour points (particularly for S8 and F2).

Table 5: NEDT for SLSTR-A in the last 11 months averaged over all detectors for both Earth views towards the hot +YBB (top) and the cold -YBB (bottom).

SLSTR-A	May 2022	Jun 2022	July 2022	Aug 2022	Sep 2022	Oct 2022	Nov 2022	Dec 2022	Jan 2023	Feb 2023	Mar 2023
+YBB temp (K)	302.854	302.607	302.557	302.394	302.553	303.014	303.592	303.793	303.727	303.447	302.983
NEDT (mK)	S7	17.7	17.7	17.7	17.6	83.8	17.4	17.3	17.1	17.2	17.2
	S8	12.1	12.1	12.2	11.9	16.0	12.0	12.0	12.0	12.0	12.0
	S9	18.7	18.8	18.9	18.3	18.5	18.4	18.5	18.4	18.5	18.5
	F1	287	288	289	283	311	282	279	278	279	279
	F2	35.2	35.5	34.7	34.6	53.0	34.9	35.2	35.4	35.3	35.3

SLSTR-A	May 2022	Jun 2022	July 2022	Aug 2022	Sep 2022	Oct 2022	Nov 2022	Dec 2022	Jan 2023	Feb 2023	Mar 2023
-YBB temp (K)	265.942	265.671	265.543	265.185	265.310	265.867	266.569	266.812	266.695	266.319	265.801
NEDT (mK)	S7	50.2	50.9	50.6	50.6	48.9	49.6	48.5	47.6	48.0	48.5
	S8	14.7	14.7	14.8	14.6	14.5	14.6	14.6	14.6	14.6	14.6
	S9	23.1	23.2	23.2	22.6	22.5	22.7	22.7	22.6	22.7	22.7
	F1	1203	1227	1228	1223	1192	1211	1176	1155	1169	1186
	F2	29.0	29.1	29.1	28.6	29.0	28.8	28.8	28.8	28.9	28.9

4.5.4 SLSTR-B TIR channel NEDT

The thermal channel NEDT values for SLSTR-B in March 2023, calculated from the hot and cold blackbody signals are shown in Figure 13 with monthly averages in Table 6. The thermal channel NEDT values for SLSTR-B in March 2023 are consistent with previous operations and within the requirements. Note that these averages are now calculated for each calendar month, whereas in data quality reports before January 2022 they were aligned to the satellite 27 day repeat cycles.

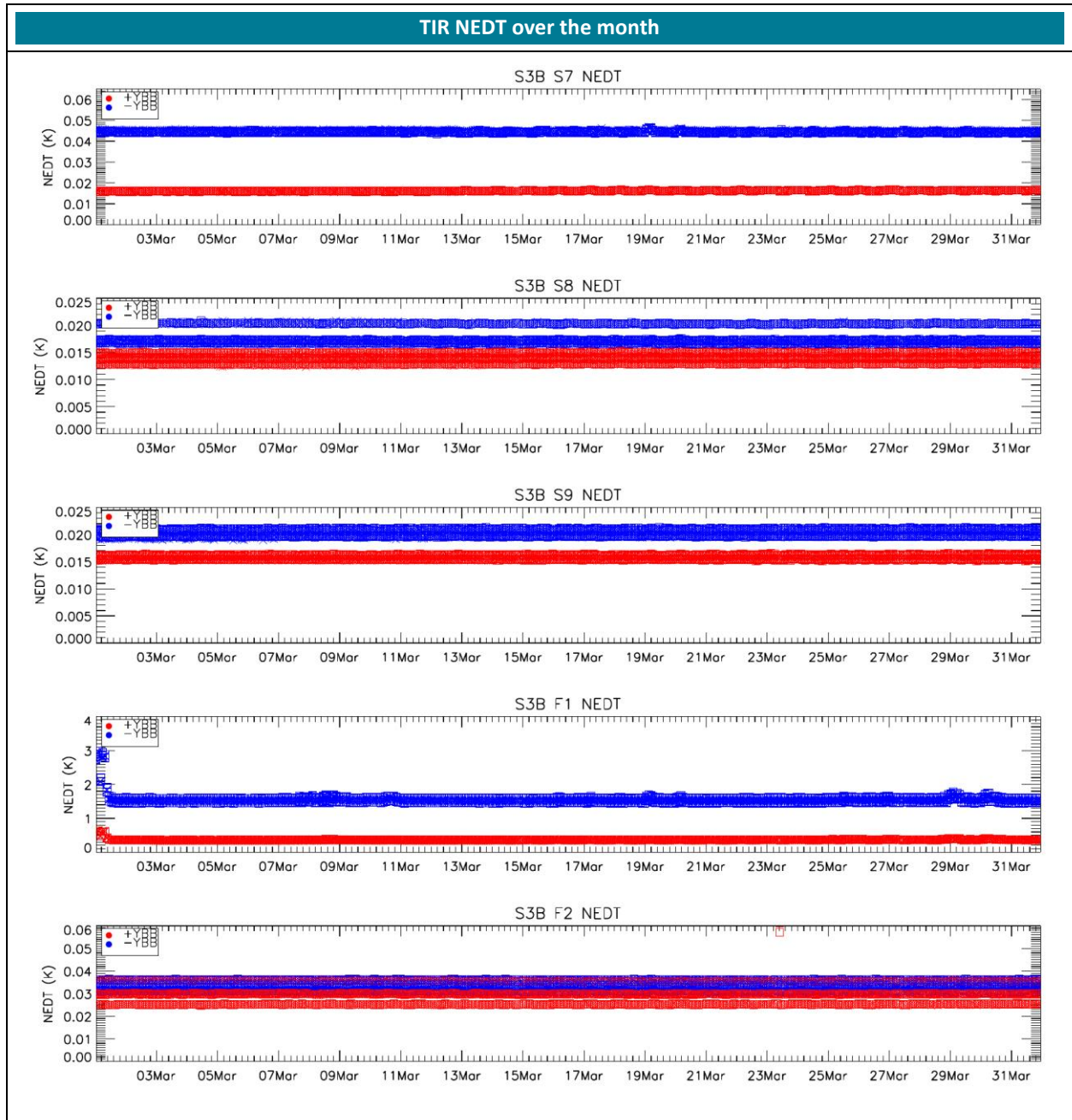


Figure 13: SLSTR-B NEDT trend for the thermal channels in March 2023. Blue points were calculated from the cold blackbody signal and red points from the hot blackbody. The square symbols show results calculated from the nadir view and crosses show results from the oblique view. Results are plotted for all detectors and integrators, which is why there are several different levels within the same colour points (particularly for S8 and F2).

Table 6: NEDT for SLSTR-B in the last 11 months averaged over all detectors for both Earth views towards the hot +YBB (top) and the cold -YBB (bottom).

SLSTR-B	May 2022	Jun 2022	July 2022	Aug 2022	Sep 2022	Oct 2022	Nov 2022	Dec 2022	Jan 2023	Feb 2023	Mar 2023	
+YBB temp (K)	303.008	302.754	302.642	302.565	302.706	303.138	303.596	303.894	303.850	303.489	303.074	
NEDT (mK)	S7	16.2	16.5	16.5	16.5	16.5	16.8	16.2	16.1	16.0	16.1	16.2
	S8	14.3	14.3	14.0	14.0	14.0	14.1	14.0	14.3	13.9	14.0	14.0
	S9	16.5	16.4	15.8	15.8	15.9	16.0	15.9	16.5	15.9	16.0	15.8
	F1	385	395	368	367	362	375	350	345	349	369	367
	F2	30.3	30.3	30.2	30.1	30.1	30.4	30.4	30.6	30.5	30.4	30.2

SLSTR-B	May 2022	Jun 2022	July 2022	Aug 2022	Sep 2022	Oct 2022	Nov 2022	Dec 2022	Jan 2023	Feb 2023	Mar 2023	
-YBB temp (K)	265.661	265.342	265.060	264.868	264.982	265.525	266.220	266.554	266.431	265.924	265.360	
NEDT (mK)	S7	44.3	44.3	44.7	45.6	45.2	43.3	43.2	42.9	42.8	43.7	44.6
	S8	18.3	18.1	17.9	17.9	17.9	17.8	17.9	17.9	18.0	18.0	17.8
	S9	21.4	21.1	20.3	20.3	20.4	20.2	20.4	20.4	20.4	20.5	20.2
	F1	1585	1600	1526	1549	1521	1441	1435	1427	1430	1564	1550
	F2	33.9	33.7	33.1	33.3	33.2	33.1	33.1	33.1	33.2	33.3	33.1

 <p>OPT-MPC Optical Mission Performance Cluster</p>	<p>Optical MPC</p> <p>Data Quality Report – Sentinel-3 SLSTR</p> <p>March 2023</p>	<p>Ref.: OMPC.ACR.DQR.04.03-2023</p> <p>Issue: 1.1</p> <p>Date: 14/04/2023</p> <p>Page: 25</p>
---	---	--

4.6 Calibration factors

4.6.1 VIS and SWIR radiometric response

The radiometric gain derived from the VISCAL signals over the past year are shown in this section. It should be noted that the data from the VISCAL unit and blackbodies calibrates the signal and counteracts the degradation of the optics and other variations in signal observed in the plots.

There are several features that appear in this parameter that can be explained as:

- ❖ The visible channels show oscillations in their radiometric response due to the build-up of ice on the optical path within the focal plane assembly (FPA). Similar oscillations were observed for the corresponding channels on ATSR-2 and AATSR. As described in Section 4.2, periodic decontamination of the infrared FPA is necessary to remove the water ice contamination.
- ❖ The radiometric responses of the SWIR channels appear to be more stable and not affected by the build-up of water ice contamination, although there is a seasonal cycle of the response that could be caused by variations in the solar zenith angle on the diffuser or partial vignetting of the Sun's disc by the VISCAL baffle.
- ❖ Note that the period of the oscillations depends on the rate of build up of the ice layer, which is faster for SLSTR-B because it has had less time to decontaminate.

4.6.2 SLSTR-A

Figure 14 and Figure 15 show the variation of the radiometric gain derived from the VISCAL signals for SLSTR-A over the past year. The data from the last month appears normal and follows the expected trend. The following features in this annual trend plot should be noted:

- ❖ August 2022. An anomaly occurred on the instrument on 1st August, which was recovered with a power cycle and decontamination/cooldown. This causes a discontinuity in the gain due to the reduction in water ice after the decontamination.

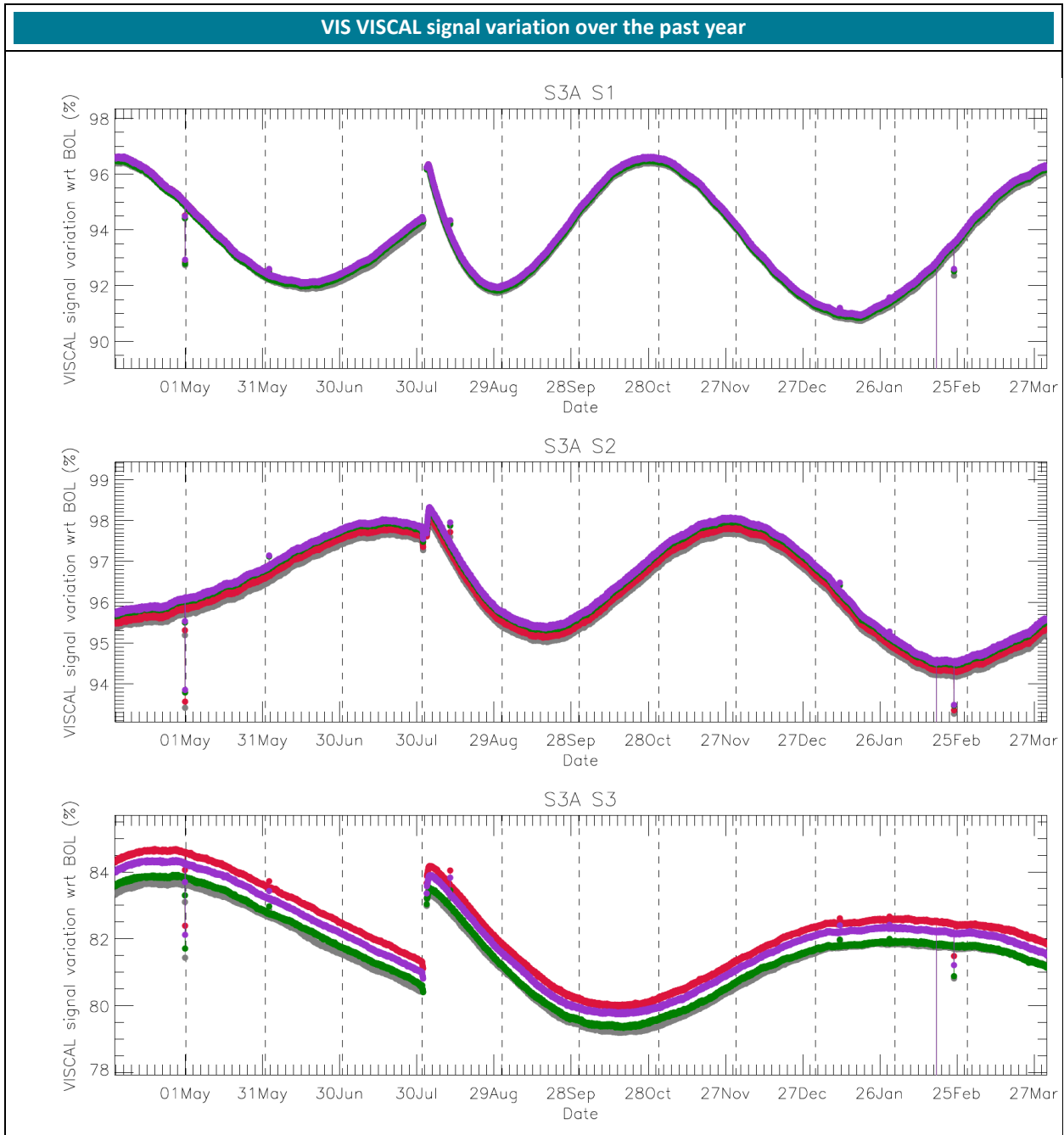


Figure 14: Variation of the radiometric gain derived from the VISCAL signals for SLSTR-A VIS channels for the last year of operations (nadir view). Different colours represent different detectors. The vertical dashed lines indicate the start of each month.

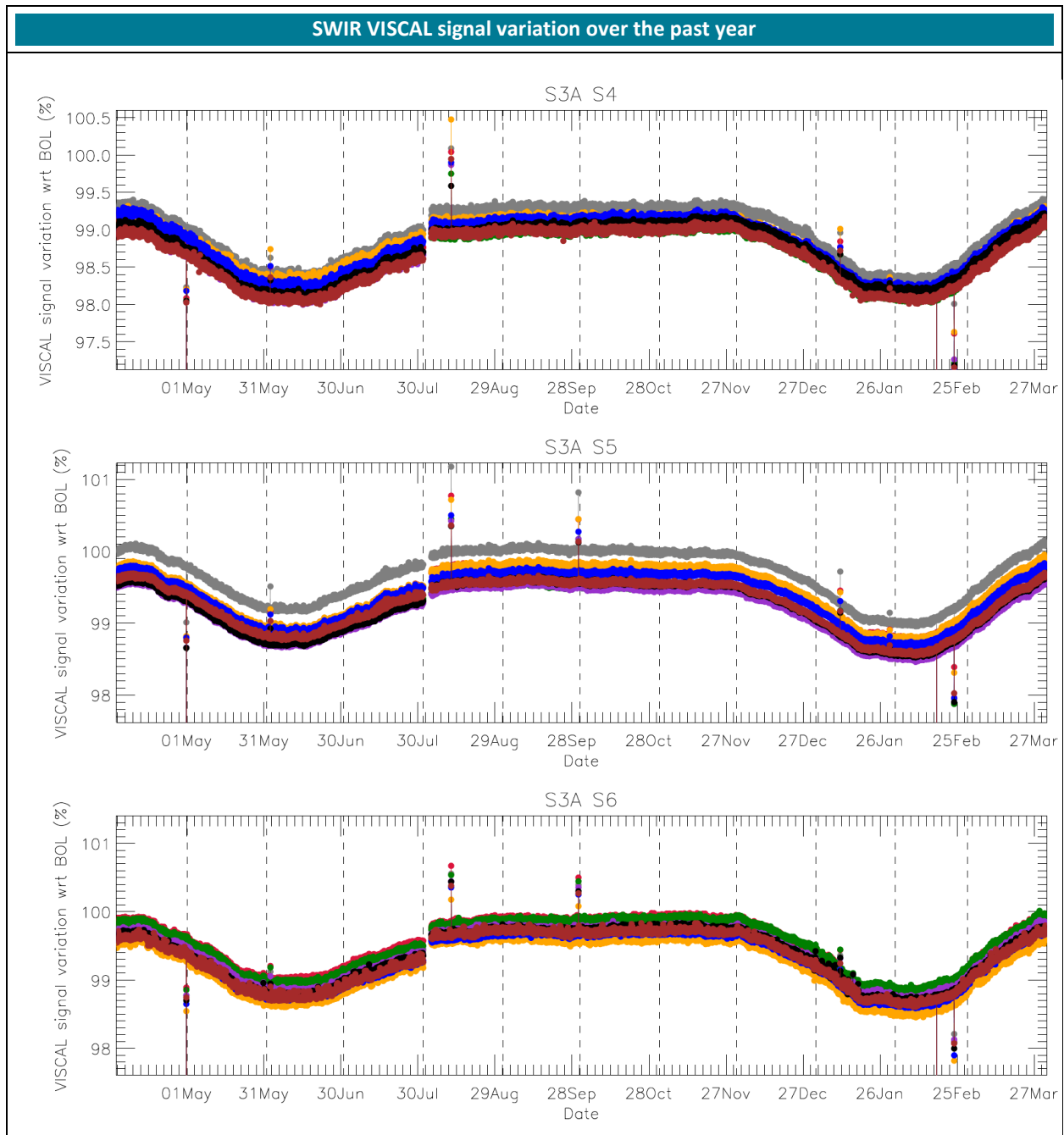


Figure 15: Variation of the radiometric gain derived from the VISCAL signals for SLSTR-A SWIR channels for the last year of operations (nadir view). Different colours represent different detectors. The vertical dashed lines indicate the start of each month.

4.6.3 SLSTR-B

Figure 16 and Figure 17 show the variation of the radiometric gain derived from the VISCAL signals for SLSTR-B over the past year. The data from the last month appears normal and follows the expected trend. There are several features in this annual trend plot to note.

- ❖ There is noisy behaviour and numerous drops in signal in the radiometric gain, especially in channels S1 and S2. This gives 2-3% errors in the radiometric calibration of these channels. A

number of candidate root causes have been identified, with the most likely due to motional chopping of the VIS detectors by an internal aperture in the VIS optical bench. Because the effect appears to be random it is most likely affecting all the data for S1 and S2.

- ❖ The impact of the anomaly reported on 20th June and subsequent decontamination/cool-down can be observed in the data as a discontinuity.

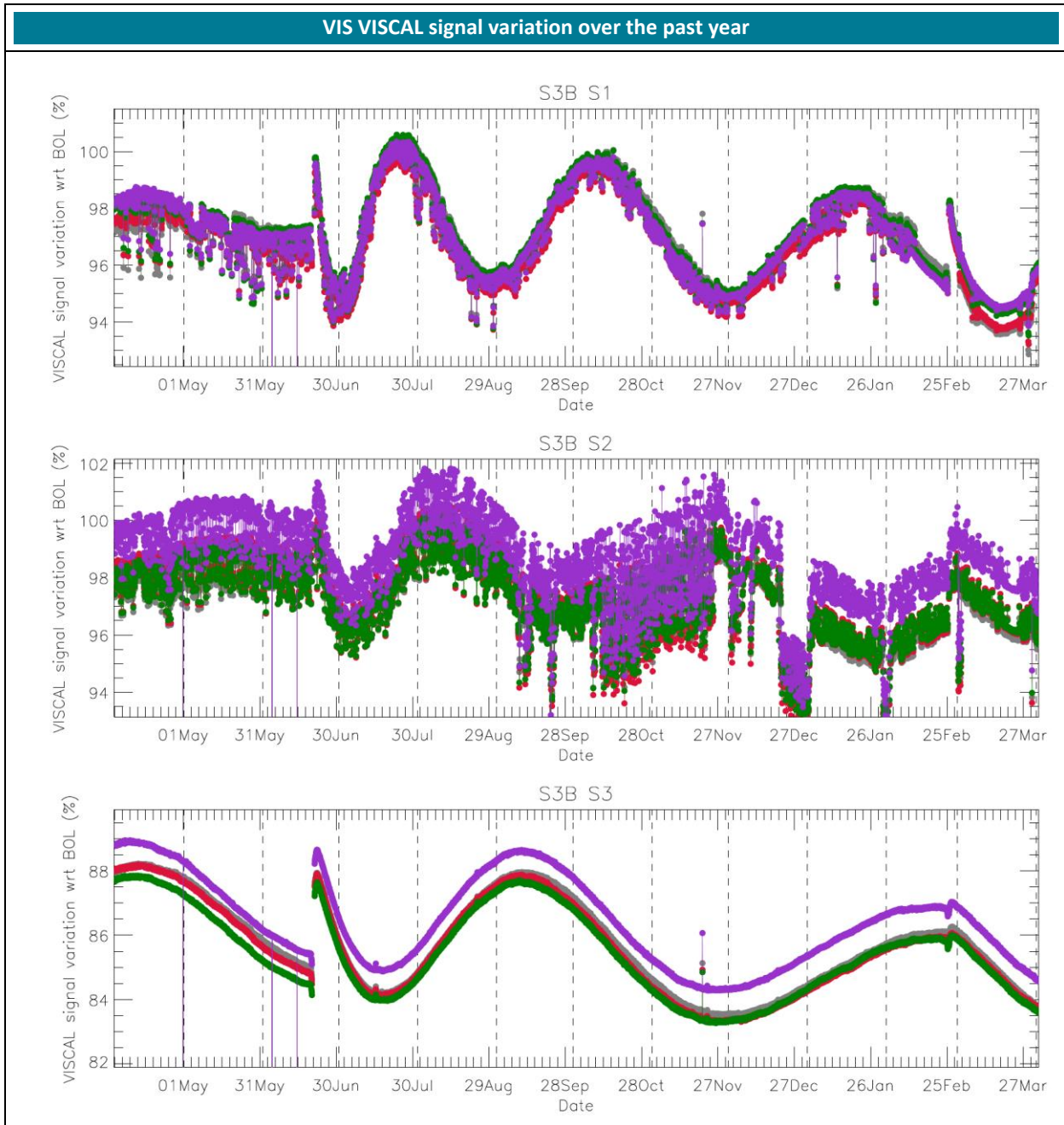


Figure 16: Variation of the radiometric gain derived from the VISCAL signals for SLSTR-B VIS channels for the past year (nadir view). Different colours represent different detectors. The vertical dashed lines indicate the start of each month.

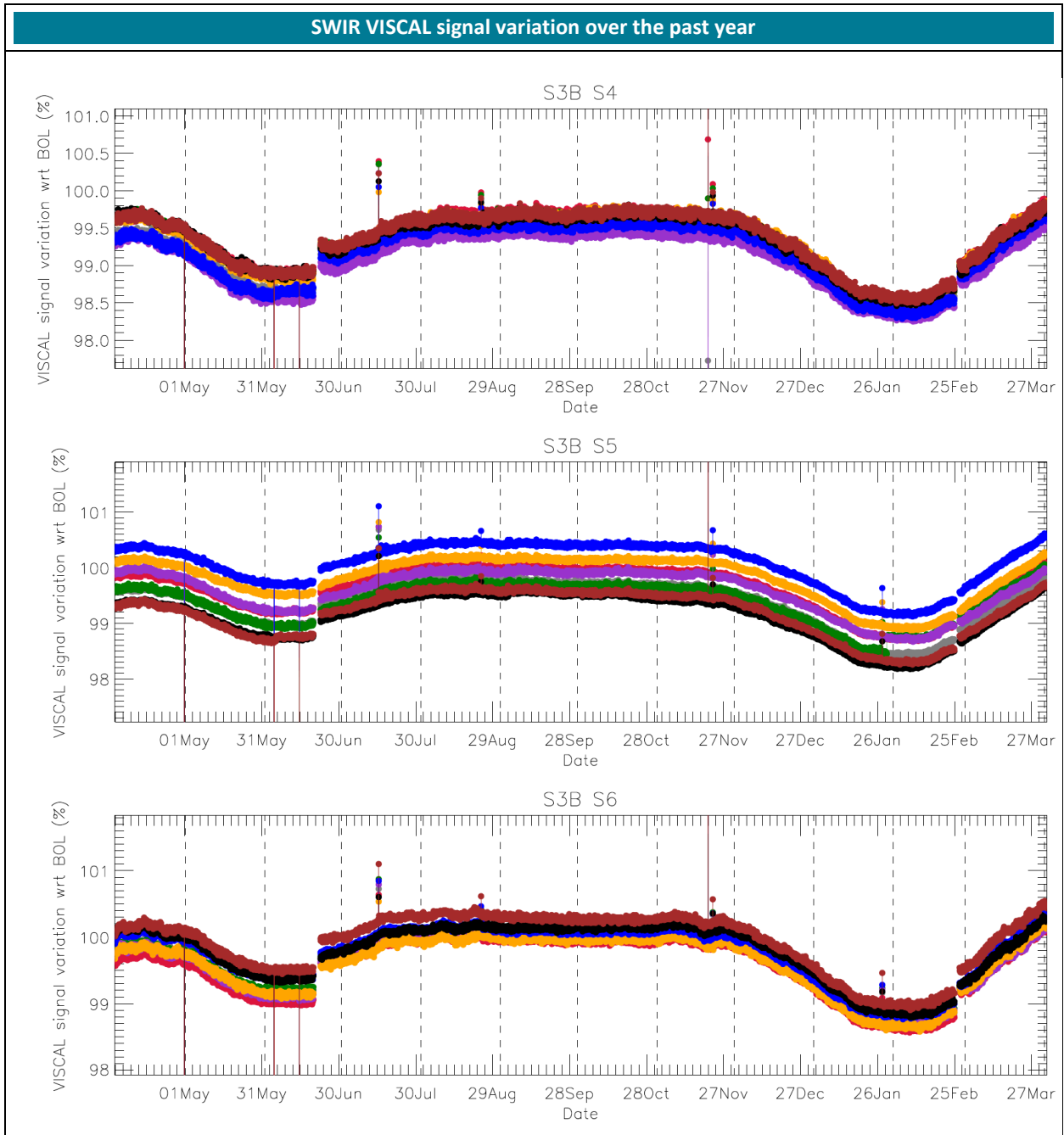


Figure 17: Variation of the radiometric gain derived from the VISCAL signals for SLSTR-B SWIR channels for the past year (nadir view). Different colours represent different detectors. The vertical dashed lines indicate the start of each month.

5 Level-1 product validation

Level-1 product quality is assessed in terms of radiometric and geometric accuracy

The Level-1 image quality is assessed when data are available at the MPC. For example, by combining all granules over one day into a single combined image. The S3A and S3B satellites are configured to be 140 degrees out of phase in order to observe complimentary portions of the earth. Figure 18 shows an example combined SLSTR-A/SLSTR-B image for the visible channels on 30th March 2023 (daytime only).

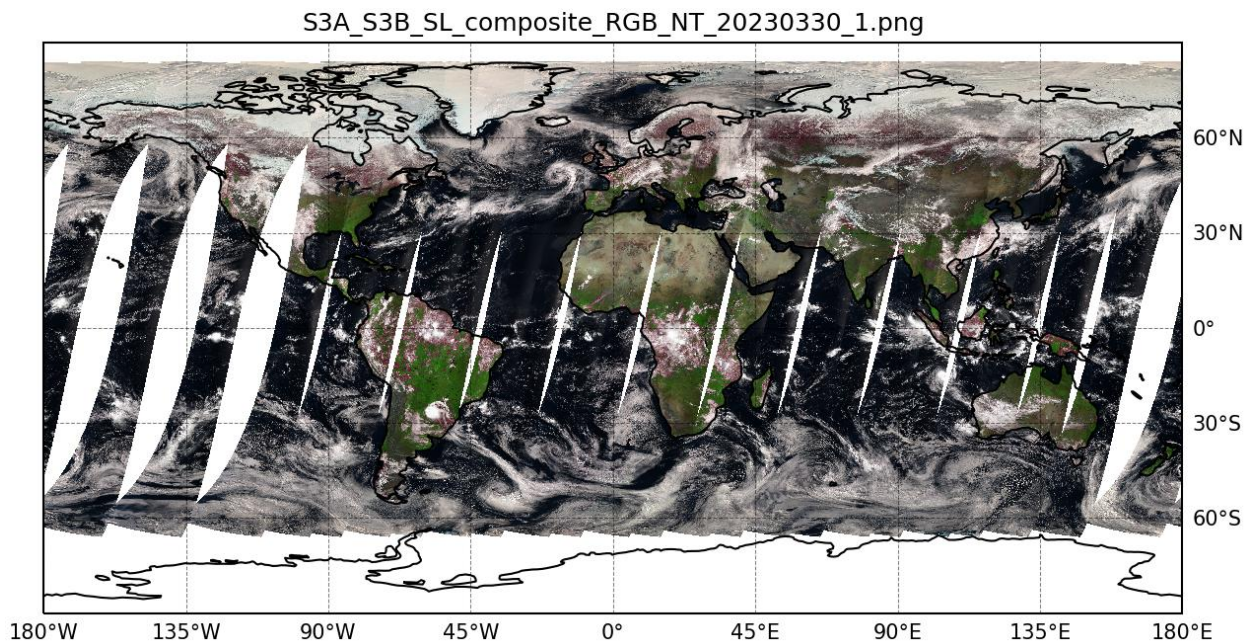


Figure 18: Daytime combined SLSTR-A and SLSTR-B Level-1 image for visible channels on 30th March 2023.

5.1 Level-1 TIR Radiometric Validation

S3_MR_1000 Relative radiometric accuracy: Sentinel-3 infrared channels shall have a relative radiometric accuracy of <0.08K (threshold) with a goal of 0.05 K over a range of 210-350 K expressed as NEDT traceable to international reference standards.

The absolute radiometric calibration of the IR channels is being validated by EUMETSAT using comparisons against IASI-A and B (Tomazic et al 2018). These results confirmed very good performance with almost no bias (< 0.1 K) for channels S8 and S9 in the nadir view over the temperature range 220 – 280 K.

5.2 Level- 1 VIS SWIR Radiometric Validation

A3_MR_1010 Absolution radiometric accuracy: Sentinel-3 VIS reflectance at TO shall have an absolute radiometric accuracy goal of < 2% with reference to the sun for the 400-900 nm wavebands and <5% with reference to the sun for wavebands >900 nm traceable to international reference standards.

Validation of the VIS/SWIR radiometric measurements is performed by various methods to establish the magnitude of any calibration offset. Some activities are routinely performed each month and reported here, and some are less regular and reported in the annual data quality reports.

The results of these different methods have been collated and have been found to agree that there is a calibration offset present in the VIS/SWIR radiances. It is recommended therefore that users apply an offset in-line with the values presented in Table 7. These offsets are stable and apply to the entire mission. Note that uncertainty estimates are at k=1.

Nadir View	S1	S2	S3	S5	S6
Correction	0.97	0.98	0.98	1.11	1.13
Uncertainty	0.03	0.02	0.02	0.02	0.02
Oblique View	S1	S2	S3	S5	S6
Correction	0.94	0.95	0.95	1.04	1.07
Uncertainty	0.05	0.03	0.03	0.03	0.05

Table 7. The recommended corrections that should be applied to SLSTR-A and SLSTR-B VIS, SWIR channels.

5.2.1 S3ETRAC latest mission trend SLSTR-A and SLSTR-B

The radiometric calibration of the visible and SWIR channels is routinely monitored using the S3ETRAC service. SLSTR data is compared to three different satellite instruments over these sites, with average ratios in each case are given in the figures.

- ❖ Figure 19 shows the results of the inter-comparison analysis of SLSTR-A with OLCI-A and SLSTR-B with OLCI-B over desert sites.
- ❖ Figure 20 shows the results of an inter-comparison analysis of SLSTR-A and SLSTR-B with AATSR.
- ❖ Figure 21 shows the results of the inter-comparison analysis with MODIS.

The results presented in the current issue refer to the period of December 2022.

A year-by-year breakdown of the drift in % since the start of the mission for SLSTR-A is provided in Table 8. Uncertainty in the drift rate is estimated at 1%.

Table 8. A year-by-year breakdown of the drift in % since the start of the mission for SLSTR-A Note the trends for S6 are based on comparisons with MODIS-Aqua which are limited to June-July where the geometry matches.

Year	S1		S2		S3		S5a		S5b		S6a		S6b	
	Na	Ob	Na	Ob	Na	Ob	Na	Ob	Na	Ob	Na	Ob	Na	Ob
2017	0.3	0.0	0.2	0.3	0.5	0.5	0.1	0.0	0.2	0.1	0.1	-	0.0	-
2018	0.7	1.0	0.2	0.3	0.8	0.9	0.0	-0.1	0.0	-0.1	-0.6	-	-0.7	-
2019	0.9	0.5	0.4	0.4	1.1	1.2	0.0	0.0	0.0	0.0	-0.2	-	-0.3	-
2020	1.1	0.7	0.6	0.5	1.4	1.6	0.0	-0.1	0.0	-0.1	-0.2	-	-0.3	-
2021	1.4	0.9	0.6	0.6	1.6	1.8	0.0	0.0	0.0	0.0	-0.2	-	-0.3	-
2022	2.2	1.3	1.1	0.7	2.2	2.3	0.2	0.0	0.2	0.0	0.7	-	0.6	-

A year-by-year breakdown of the drift in % since the start of the mission for SLSTR-B is provided in Table 9. Uncertainty in the drift rate is estimated at 1%.

Table 9. A year-by-year breakdown of the drift in % since the start of the mission for SLSTR-B. Note the trends for S6 are based on comparisons with MODIS-Aqua which are limited to June-July where the geometry matches. Furthermore, the drift for S6 is relative to 2019 comparisons. For SLSTR-B the reference measurements were obtained before an update to the flight calibration coefficients that was performed after the S3B-IOCR. A correction factor of 2.4% has been applied to the drift rates to account for the update.

Year	S1		S2		S3		S5a		S5b		S6a		S6b	
	Na	Ob	Na	Ob	Na	Ob	Na	Ob	Na	Ob	Na	Ob	Na	Ob
2019	0.7	-1.2	0.5	-0.3	0.3	0.0	0.2	-0.1	0.3	-1.1	-	-	-	-
2020	0.9	-0.8	0.5	-0.2	0.5	0.4	0.3	-0.3	0.3	-1.3	-0.2	-	-0.2	-
2021	1.3	-0.4	0.7	0.2	0.8	0.7	0.3	-0.3	0.2	-1.3	0.0	-	-0.1	-
2022	2.1	-0.5	1.2	-0.1	1.5	1.2	0.7	-0.2	0.6	-1.2	1.0	-	0.9	-

The S3ETRAC service extracts OLCI and SLSTR Level-1 data and computes associated statistics over 49 sites corresponding to different surface types (desert, snow, ocean maximising Rayleigh signal, and ocean maximising sun-glint scattering). These S3ETRAC products are used for the assessment and monitoring of the VIS and SWIR radiometry by the ESL.

Details of the S3ETRAC/SLSTR statistics are provided on the [S3ETRAC website](#), including:

- ❖ Number of SLSTR products processed by the S3ETRAC service
- ❖ Statistics per type of target (DESERT, SNOW, RAYLEIGH, SUNGLINT)
- ❖ Statistics per site
- ❖ Statistics on the number of records

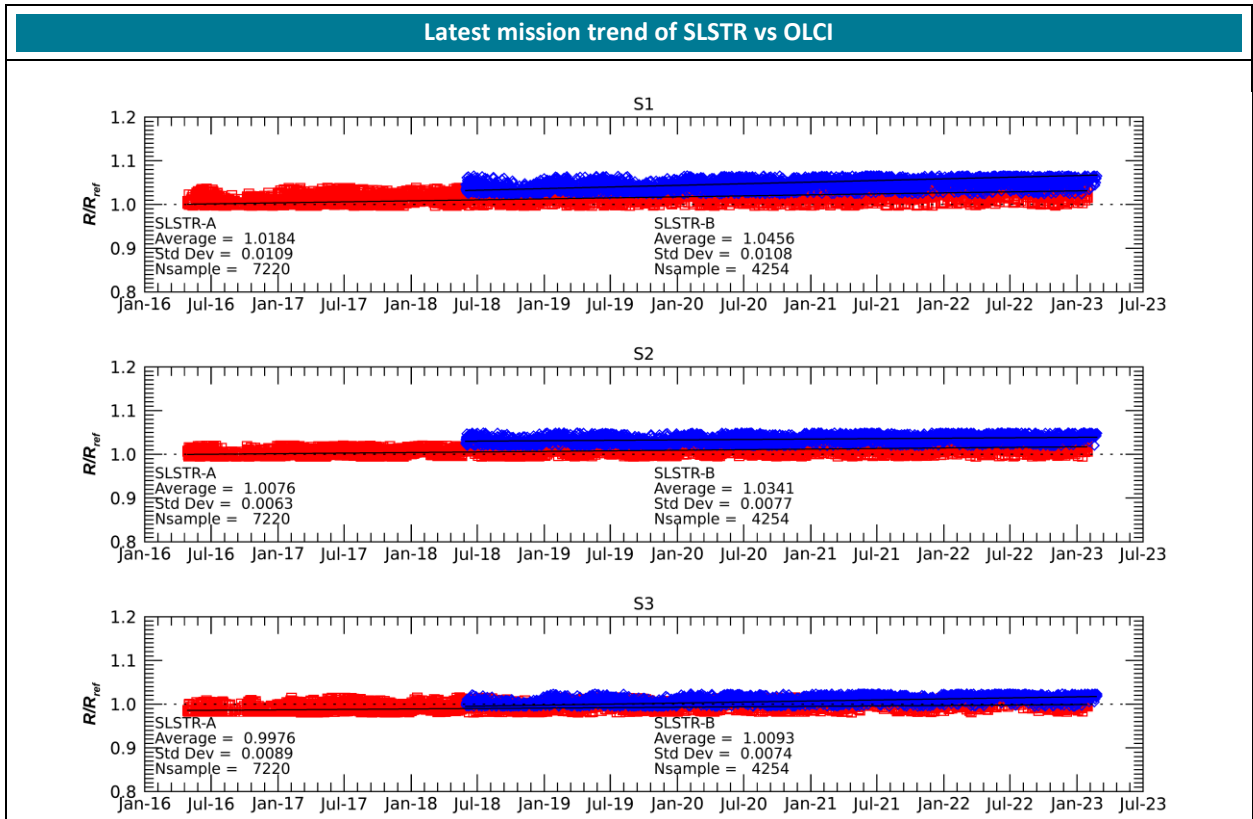


Figure 19: Ratio of SLSTR-A and OLCI-A radiances (red) and SLSTR-B and OLCI-B radiances (blue) for the visible channels in Nadir view using combined results for all desert sites.

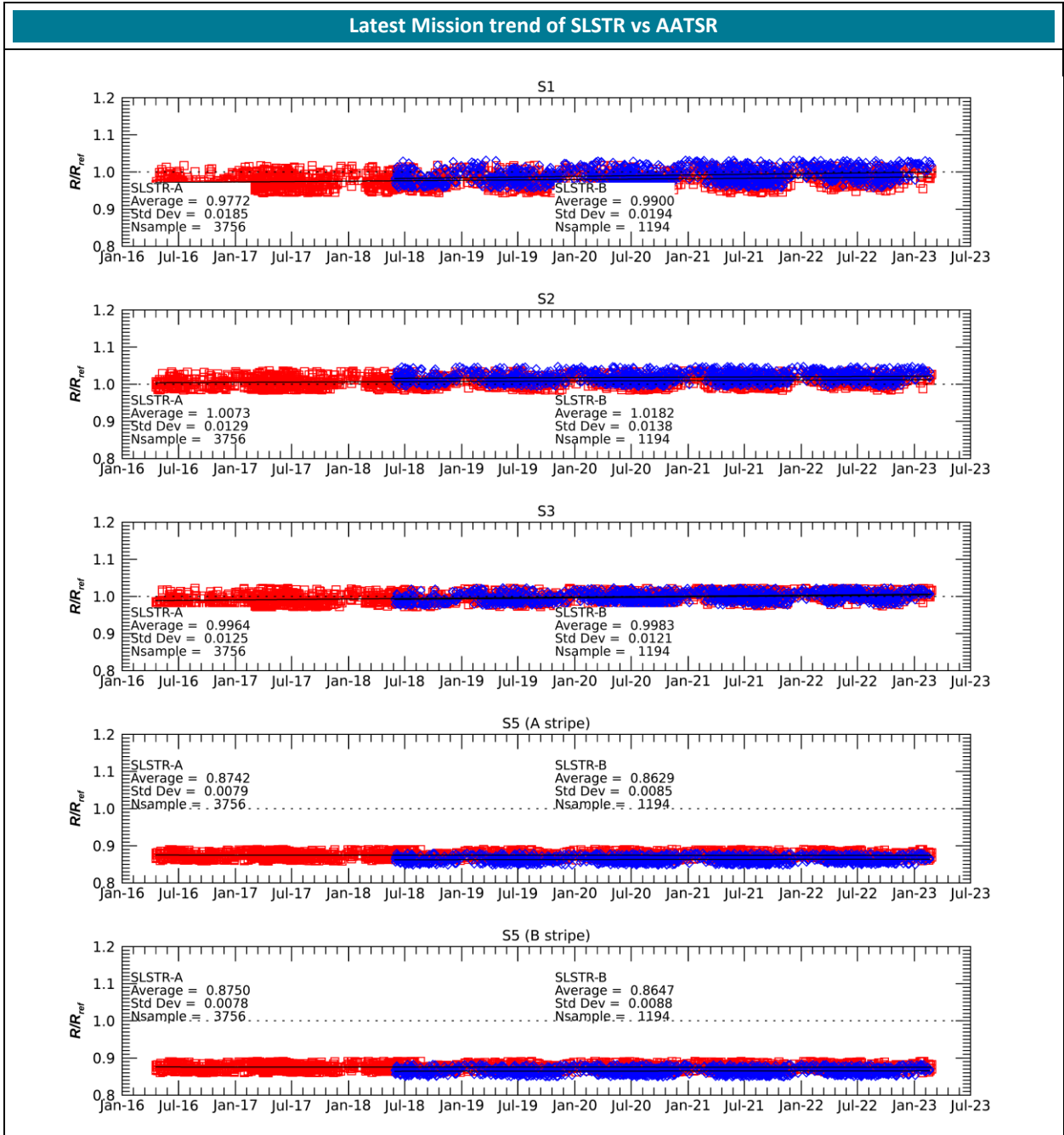


Figure 20: Ratio of SLSTR-A (red) and SLSTR-B (blue) with AATSR radiances in Nadir view using combined results for all desert sites.

Latest Mission trend of SLSTR vs MODIS

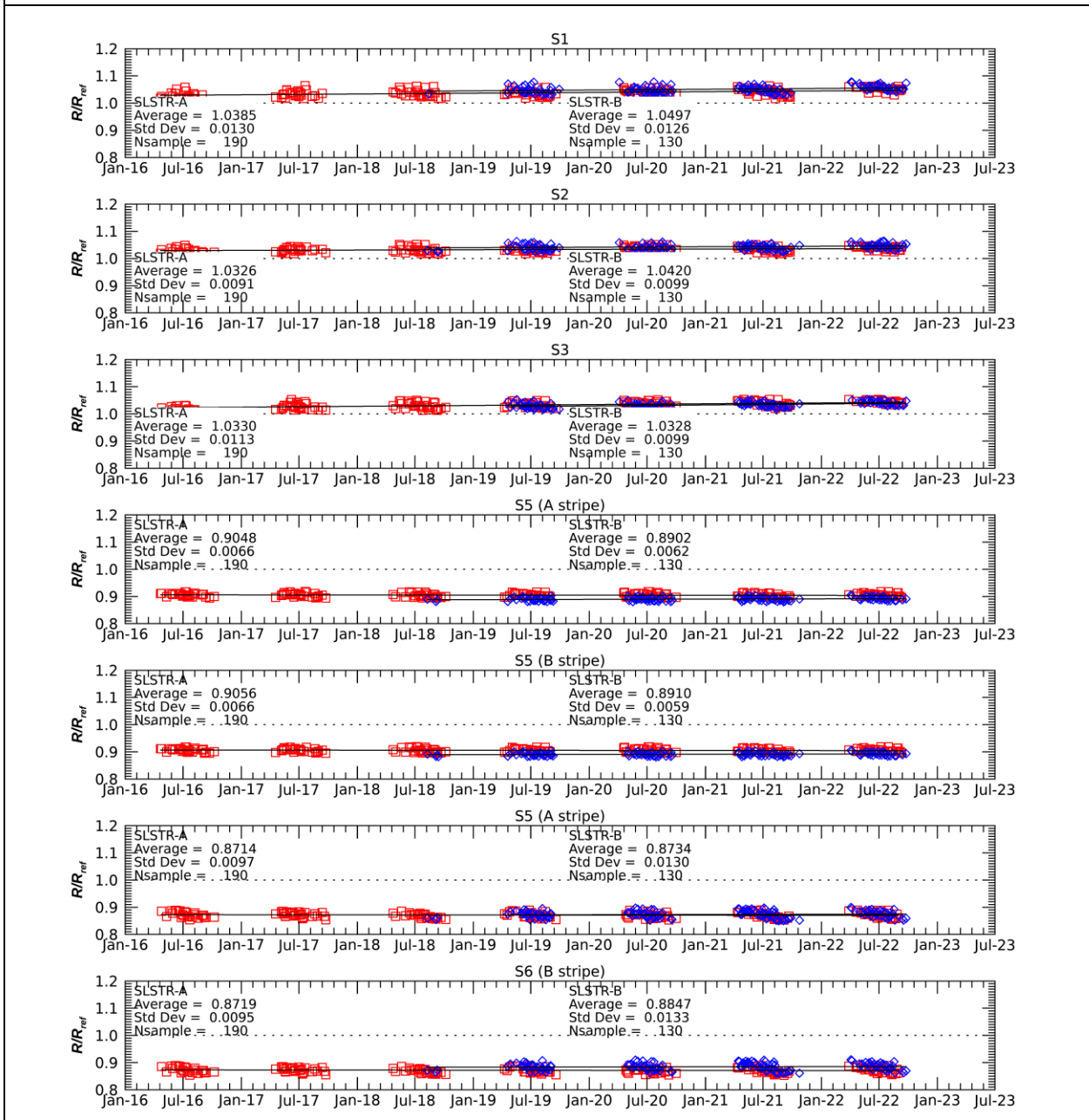
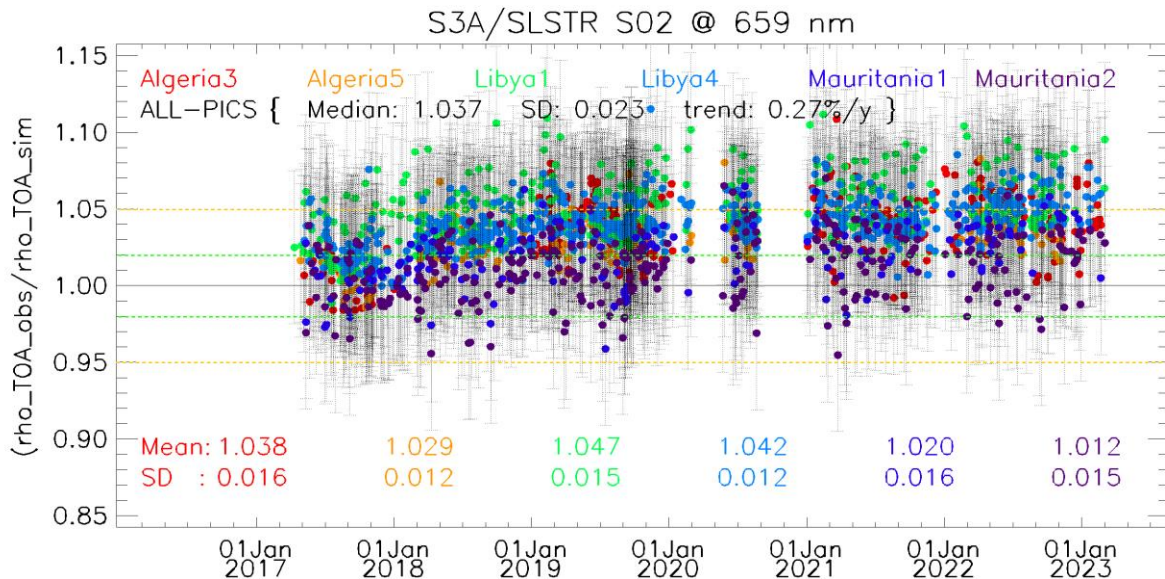


Figure 21: Ratio of SLSTR-A (red) and SLSTR-B (blue) with MODIS radiances in Nadir view using combined results for all desert sites.

5.2.2 Radiometric validation with DIMITRI

Verification and Validation over PICS

1. The ingestion of the available L1-RBT-NT products from SLSTR-A and SLSTR-B over the 6 desert CalVal-sites (Algeria3 & 5, Libya 1 & 4 and Mauritania 1 & 2) has been performed until the **20th March 2023**.
2. The results are consistent over all the six used PICS sites (Figure 22 and Figure 23). Both sensors show a good stability over the analysed period over VNIR bands for the NADIR view, with slight positive trend.
3. The temporal average over the period **March 2017 - 20th March 2023** of the elementary ratios (observed reflectance to the simulated one) for **SLSTR-A** and over the period **June 2018 - 20th March 2023** for **SLSTR-B**.
4. Both sensors show gain values between 2-4% over the VNIR bands S1-S3 (Figure 24).



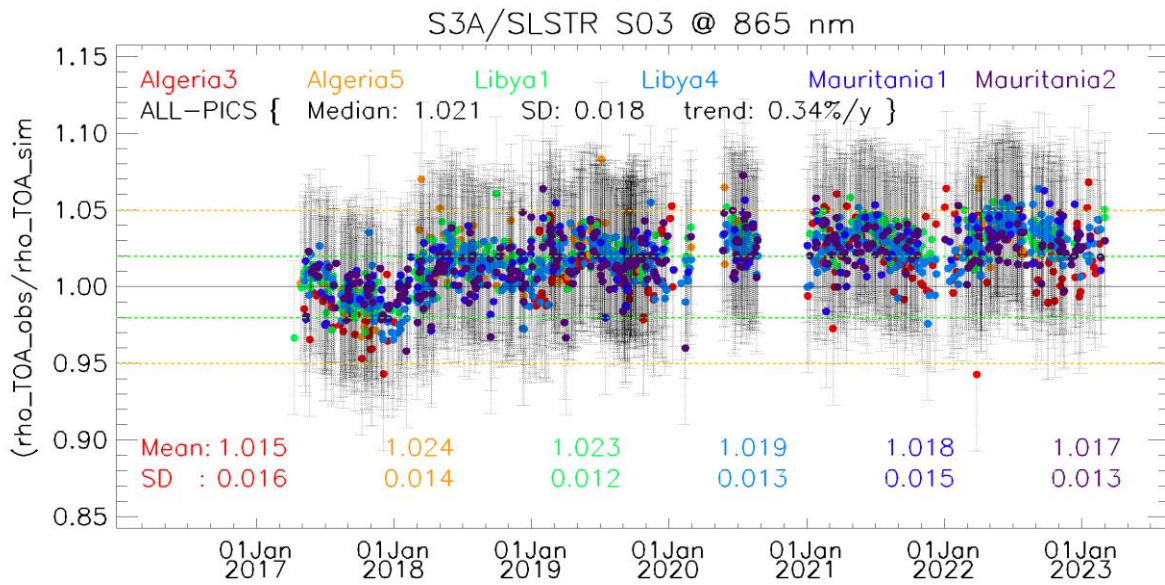


Figure 22: Time-series of the elementary ratios (observed/simulated) signal from SLSTR-A for (top to bottom) bands S02 and S03 respectively over March 2017- March 2023 from the six PICS Cal/Val sites. Dashed-green and orange lines indicate the 2% and 5% respectively. Error bars indicate the desert methodology uncertainty.

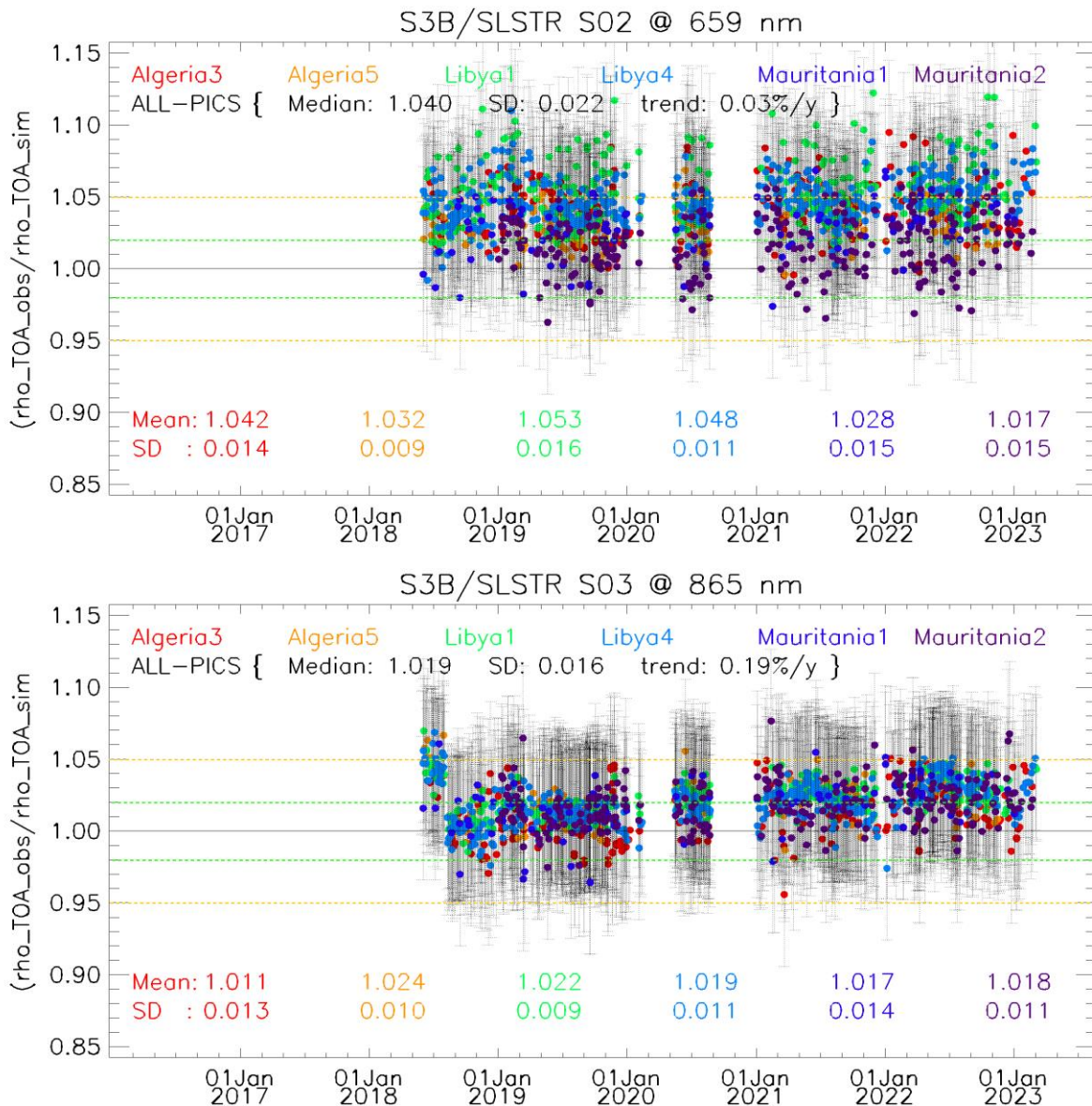


Figure 23: Time-series of the elementary ratios (observed/simulated) signal from SLSTR-B for (top to bottom) bands S02 and S03 respectively over June 2018- March 2023 from the six PICS Cal/Val sites. Dashed-green and orange lines indicate the 2% and 5% respectively. Error bars indicate the desert methodology uncertainty.

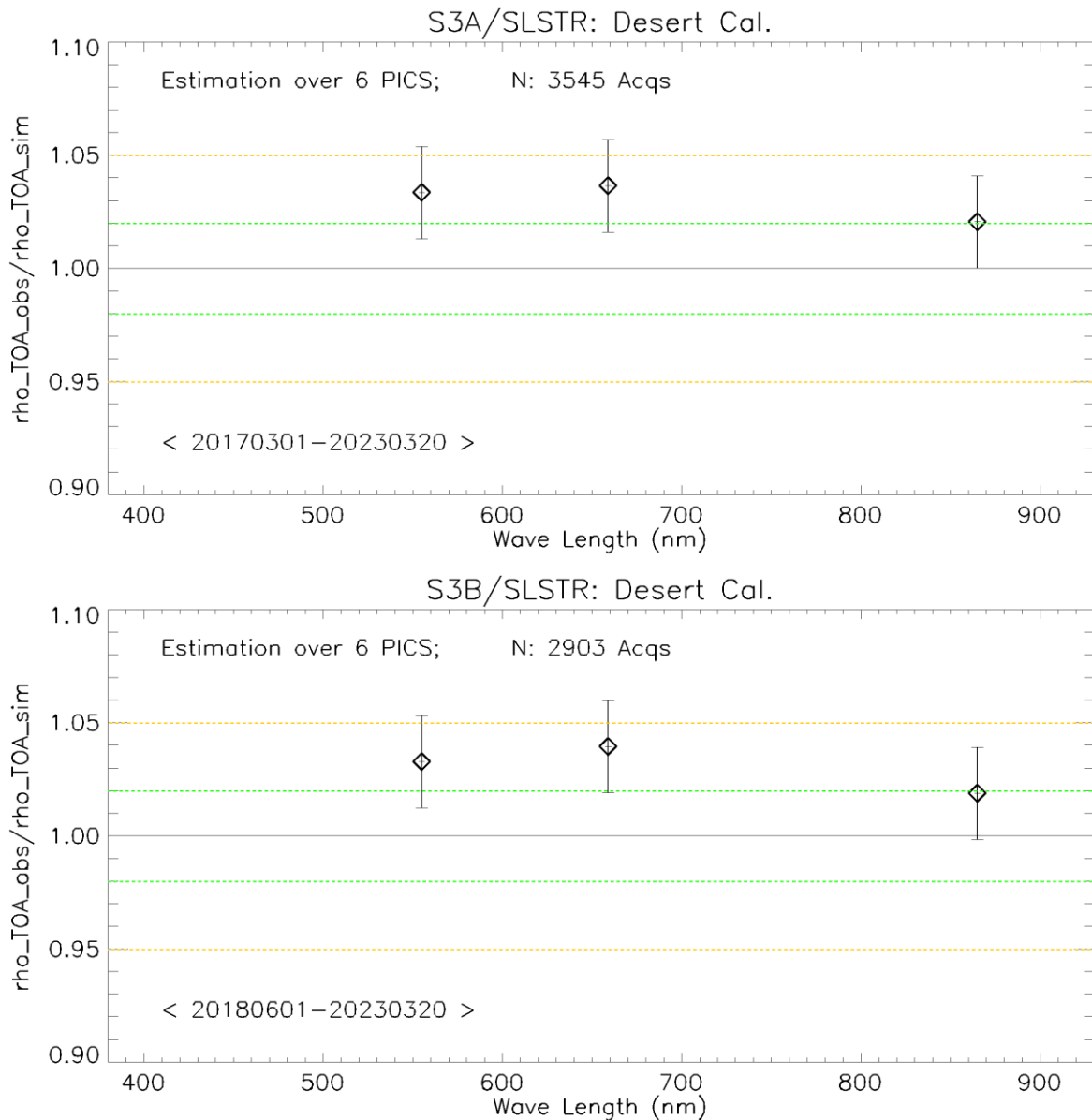


Figure 24: The estimated gain values for SLSTR-A and SLSTR-B over the 6 PICS sites identified by CEOS over the period March 2017- March 2023 and June 2018- March 2023 respectively as a function of wavelength. Dashed-green and orange lines indicate the 2% and 5% respectively. Error bars indicate the desert methodology uncertainty.

Validation over Rayleigh

Rayleigh method has been performed from the available mini-files over the period **March 2017- March 2023** for SLSTR-A and over the period **June 2018- March 2023** for SLSTR-B. The gain coefficients of both sensors are consistent with the previous results (Figure 25).

Validation over Glint

Glint calibration method has been performed over the same period as for Raileigh for SLSTR-A and SLSTR-B. The gain coefficients of both sensors are consistent with previous results (Figure 25).

Validation results synthesis

The results synthesis displayed below on Figure 25.

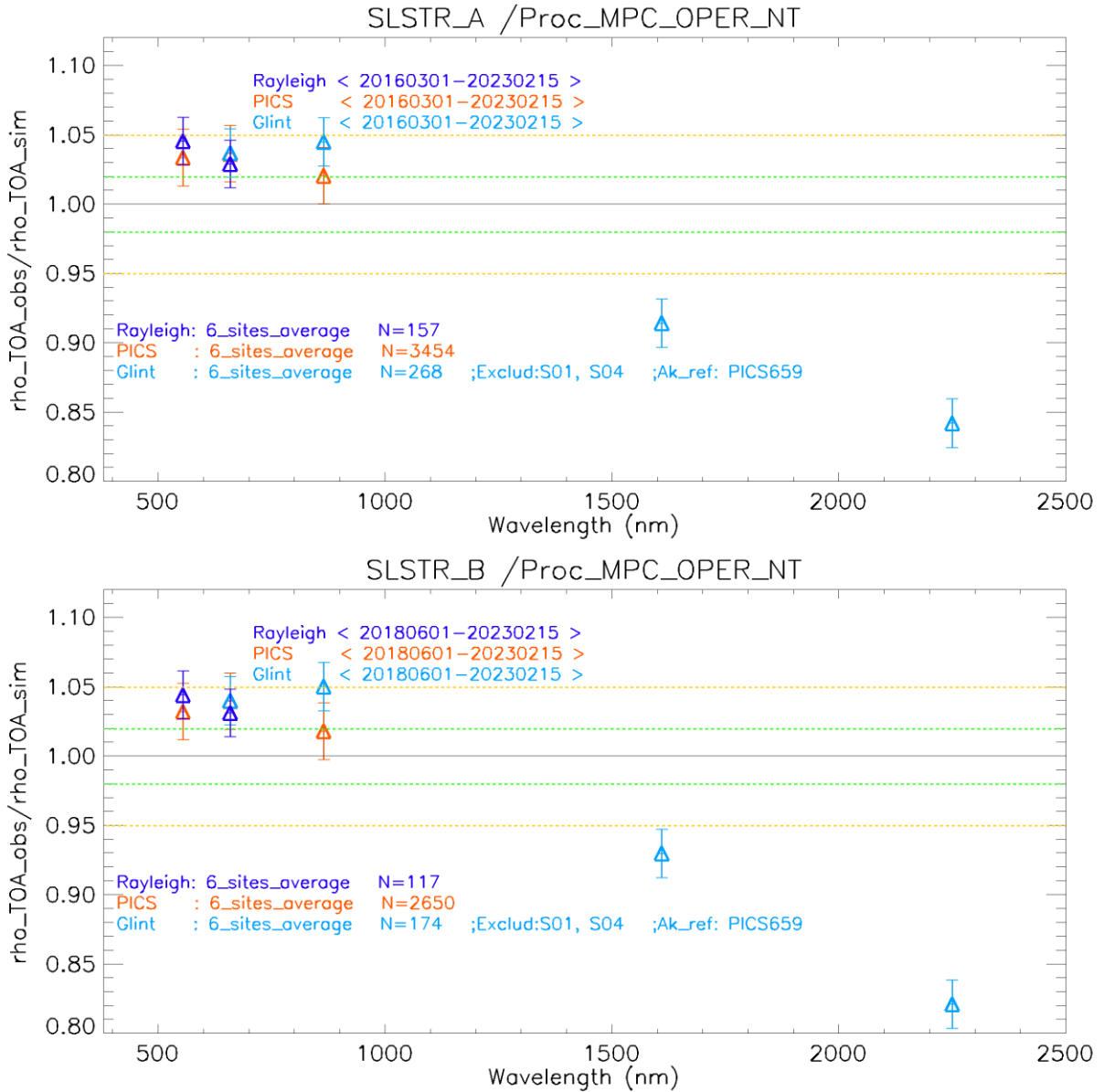


Figure 25: The estimated gain values for SLSTR-A and SLSTR-B from Glint, Rayleigh and PICS methods over the period March 2016- Feb-March 2023 and June 2018- Feb-March 2023 respectively as a function of wavelength. We use the gain value of S02 from Desert-PICS method as reference gain for Glint method. Dashed-green and orange lines indicate the 2% and 5% respectively. Error bars indicate the method uncertainties.

Cross-mission Intercomparison over PICS:

X-mission Intercomparison between SLSTR-A, SLSTR-B, MERIS, MSI-A, MSI-B, OLCI-A and OLCI-B has been performed over the 6 PICS-test-sites. Figure 26 shows the estimated gain over different time-series for different sensors over PICS. The spectral bands with significant absorption of water vapor and O2 are excluded. OLCI-A, SLSTR-A and SLSTR-B seem to have higher gain with respect to the other sensors of about 1-3% over VNIR spectral range.

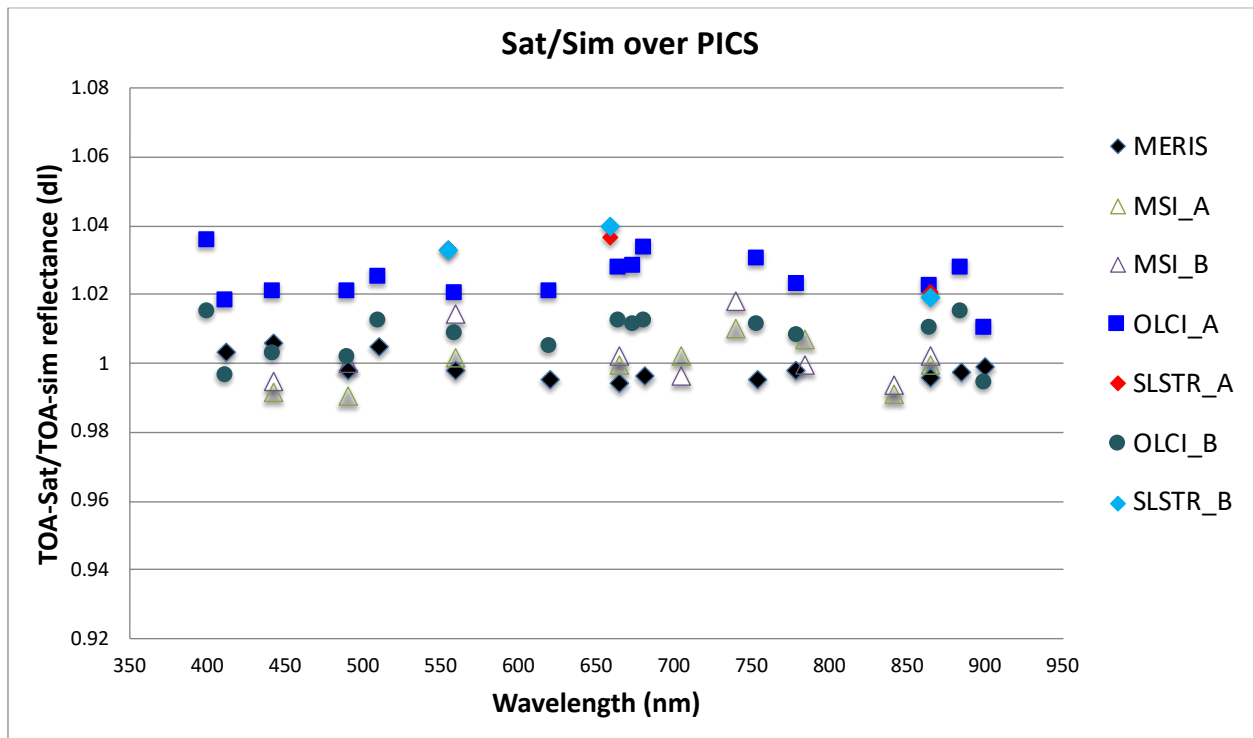


Figure 26: Ratio of observed TOA reflectance to simulated one for (black) MERIS, (pale-green) S2A/MSI, (white) S2B/MSI, (blue) S3A/OLCI, (green) S3B/OLCI, (red) S3A/SLSTR-NADIR, and (cyan) S3B/SLSTR-NADIR averaged over the six PICS test sites over different periods as a function of wavelength.

5.3 Level-1 Geometric Validation

S3_MR_1090 Geolocation accuracy: Improved geo-location accuracy is possible when using ground control points and Sentinel-3 shall be designed to ensure a geolocation accuracy of better than 0.5rm of the spatial resolution of the optical sensor when using ground control points.

S3_MR_1100 Inter channel co-registration. The inter channel spatial co-registration for Sentinel-3 visible measurements shall be < 0.5 of the spatial resolution of the sensor over the full spectral range (goal of 0.3 of the spatial resolution of the sensor)

S3_MR_1100 Inter channel co-registration: The inter channel spatial co-registration for Sentinel-3 SWIR and TIR measurements shall be sufficient to allow these channels to be co registered with visible channels at higher spatial resolution data.

Regular monitoring using the GeoCal Tool implemented at the MPC is normally carried out. On average, the geolocation accuracy of the VIS-SWIR channels meets requirements for SLSTR-A and SLSTR-B.

GeoCal is a tool that monitors the geolocation performance in Level-1 images by correlation of the images with reference features containing ground control points (GCP). Each Level-1 granule typically contains several hundred GCPs if over land, which are filtered based on signal-to-noise to obtain a daily average in the across and along track directions.

The geolocation uncertainty is stable and within requirements during the reporting period.

5.3.1 SLSTR-A

The results for March 2023 are plotted in Figure 27 for SLSTR-A, giving the average positional offsets in kilometres for Nadir and Oblique views.

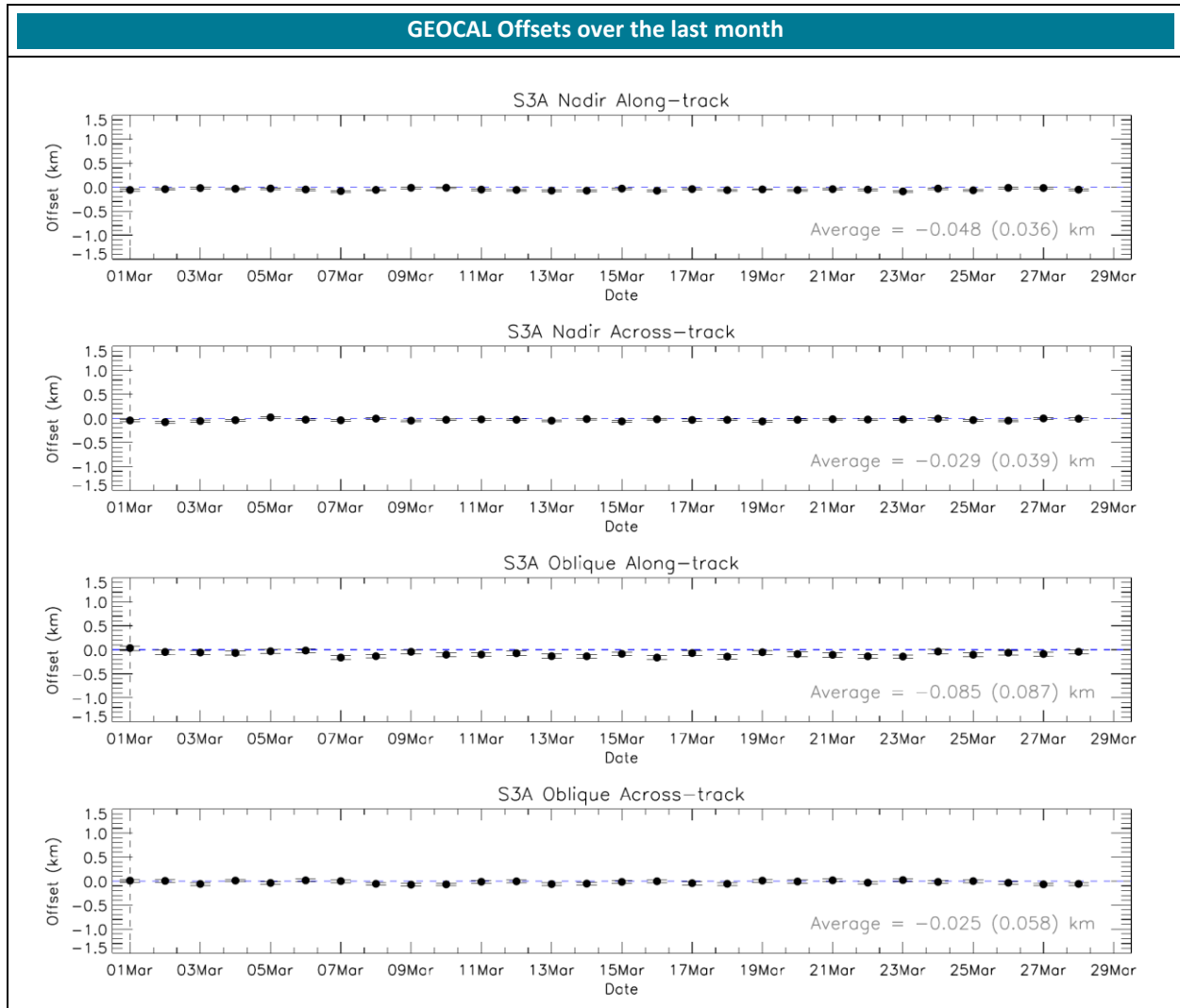


Figure 27: SLSTR-A daily offset results in km from the GeoCal Tool analysis for Nadir along- and across-track (top two plots) and Oblique along- and across-track (bottom two plots) for March 2023. The error bars show the standard deviation.

5.3.2 SLSTR-B

The results for March 2023 are plotted in Figure 28 for SLSTR-B, giving the average positional offsets in kilometres for Nadir and Oblique views.

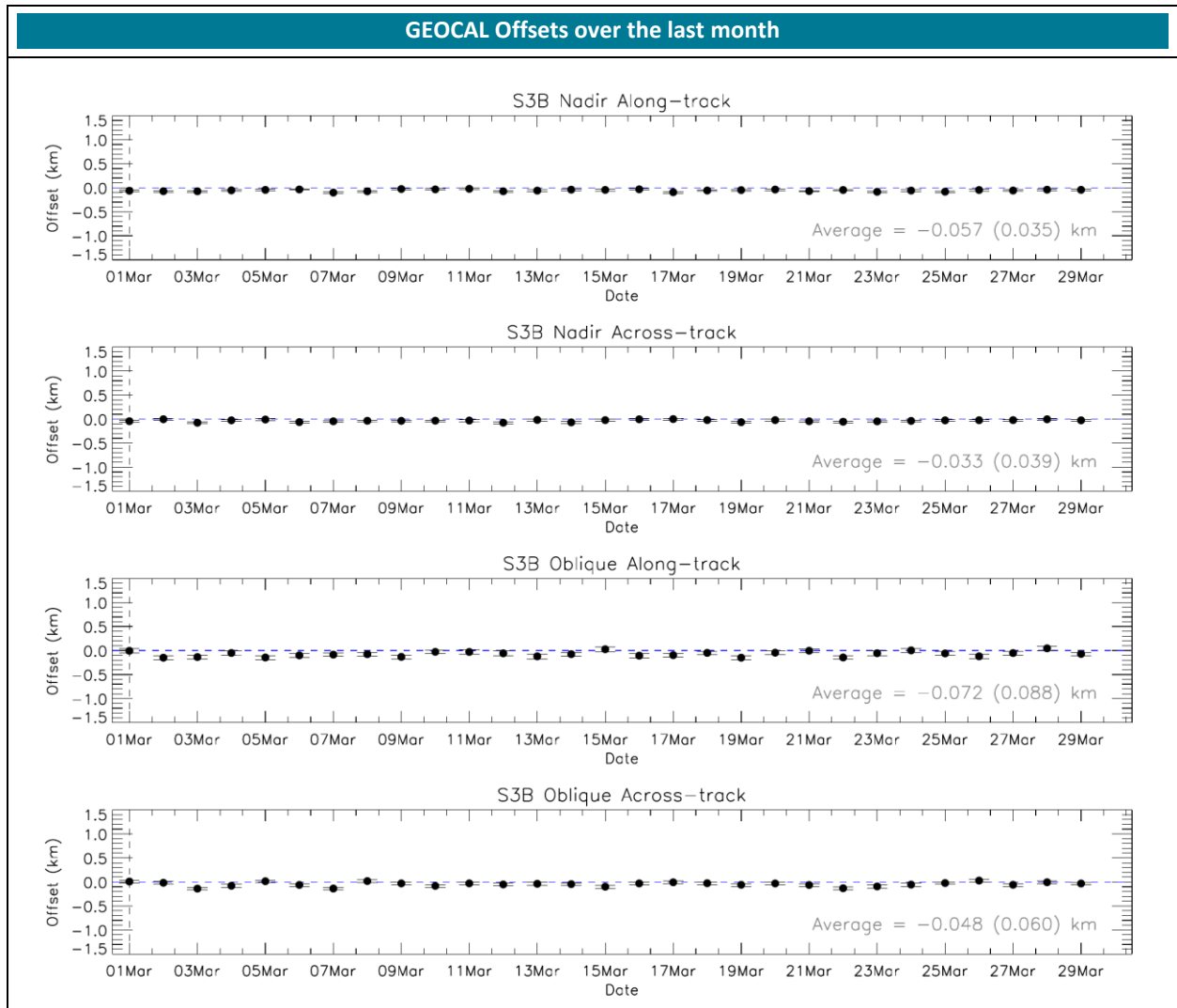


Figure 28: SLSTR-B daily offset results in km from the GeoCal Tool analysis for Nadir along- and across-track (top two plots) and Oblique along- and across-track (bottom two plots) for March 2023. The error bars show the standard deviation.

6 Level 2 LST validation

Level 2 Land Surface Temperature products have been validated against *in situ* observations (Category-A validation) from twelve “Gold Standard” Stations, and intercompared (Category-C validation) with respect to an independent operational reference product (SEVIRI from LSA SAF). The different categories of validation are first described in the LST Validation Protocol (Schneider et al., 2012) and reinforced in the CEOS WGCV-LPV Land Surface Temperature Product Validation Best Practice Protocol (Guillevic et al., 2017). In all cases it is the NTC products that are validated, and the Probabilistic cloud masking implementation is used for all cloud masking. Level-3C products for the full month of December 2023 for SLSTR-A and SLSTR-B are evaluated for identifying any gross problems. Both S3A and S3B L2 products are produced with the updated LST coefficients following the operational release on 25th February 2019. In each case the latest temporal interpolation for the probabilistic cloud mask is applied following the L1 operational release on 15th January 2020. The updated cloud coefficients ADF was applied on 23rd October 2020.

Validation results presented in this issue refer to the period of December 2022.

6.1 Category-A validation

Category-A validation uses a comparison of satellite-retrieved LST with *in situ* measurements collected from radiometers sited at a number of stations spread across the Earth, for which the highest-quality validation can be achieved. Here we concentrate on eight “Gold Standard” stations which are installed with well-calibrated instrumentation: seven from the SURFRAD network (Bondville, Illinois; Desert Rock, Nevada; Fort Peck, Montana; Goodwin Creek, Mississippi; Penn State University, Pennsylvania; Sioux Fall, South Dakota; Table Mountain, Colorado); and one from the ARM network (Barrow, Alaska).

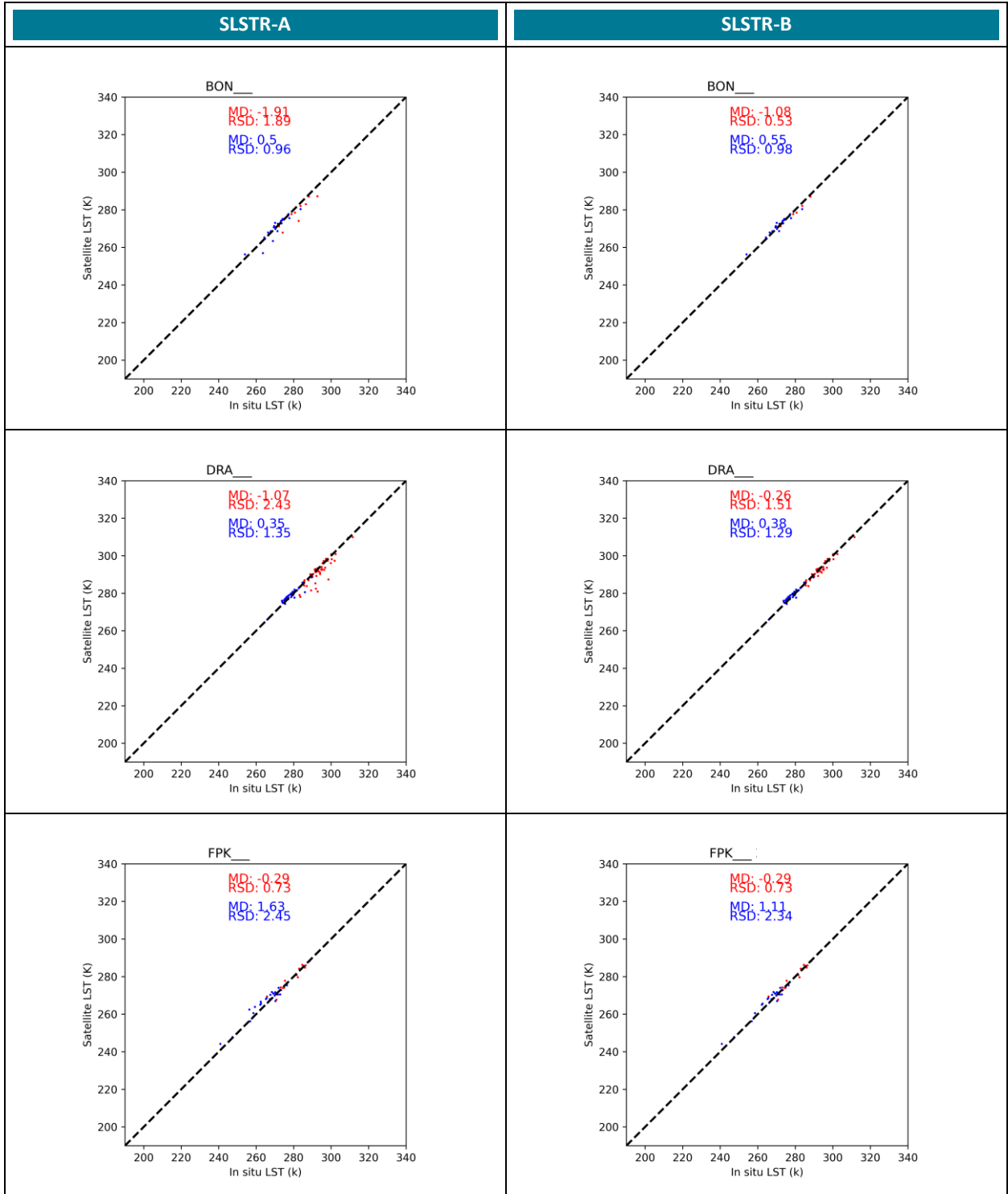
For the SURFRAD field pyrgeometers the uncertainty is estimated to be $\pm 5 \text{ Wm}^{-2}$ (Augustine and Dutton, 2013). For North Slopes Alaska the uncertainty of the IR radiance data was set to $\pm 4 \text{ Wm}^{-2}$ (Stoffel, 2006).

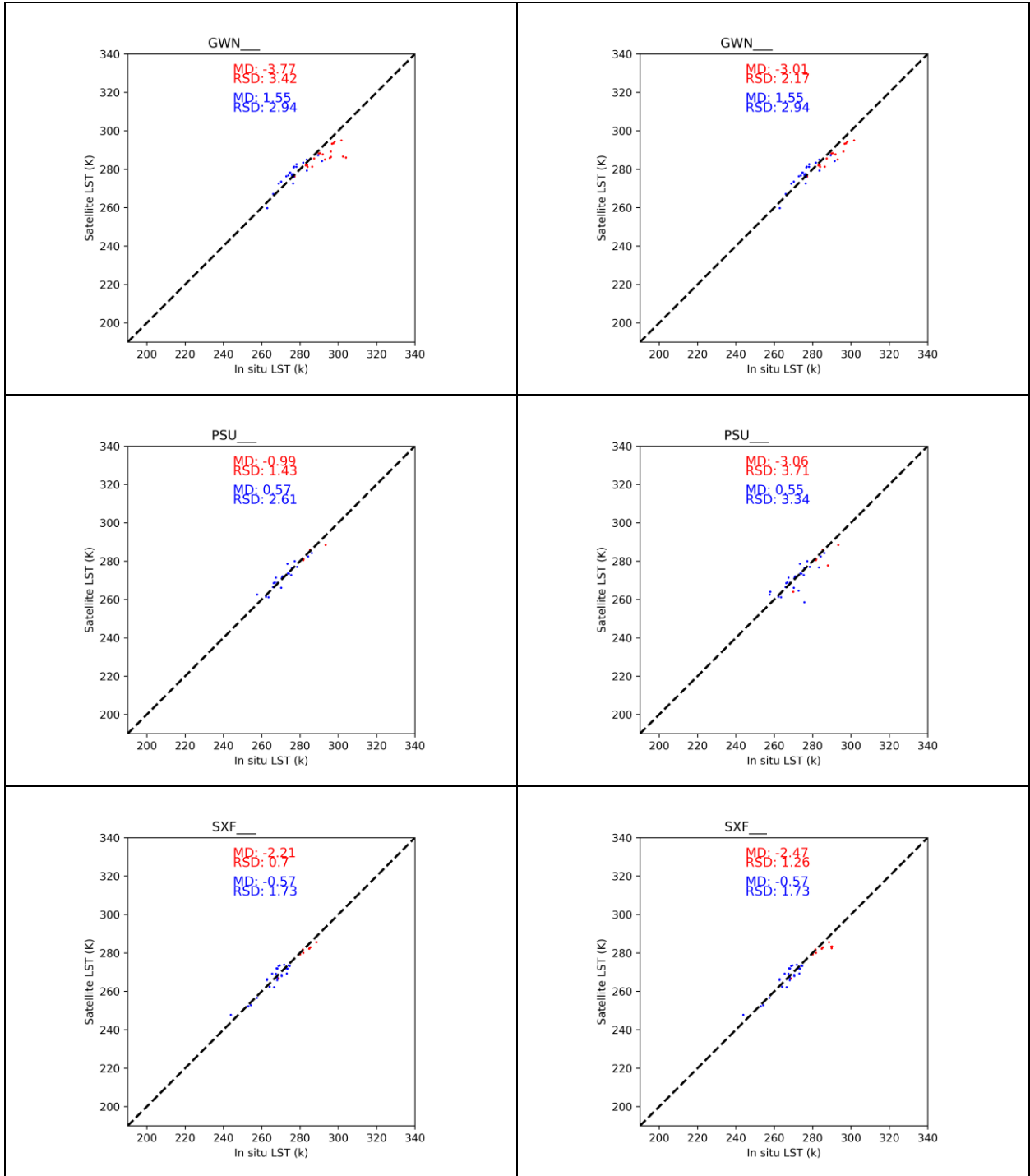
The results can be summarised as follows (accuracy is used as the metric rather than uncertainty as this is then a straight comparison with mission requirements):

Table 10: Average absolute accuracy in K of the SL_2_LST product with respect to Gold Standard stations for December 2022.

Satellite	Day	Night
S3A	-1.5	0.4
S3B	-1.4	0.4

For both SLSTR-A and SLSTR-B both the daytime and night-time absolute accuracies (which are derived from the absolute values of all the mean biases from the individual stations) are close to the mission requirement of 1K. The main impact on accuracy and precision is driven by any errors in the cloud masking.





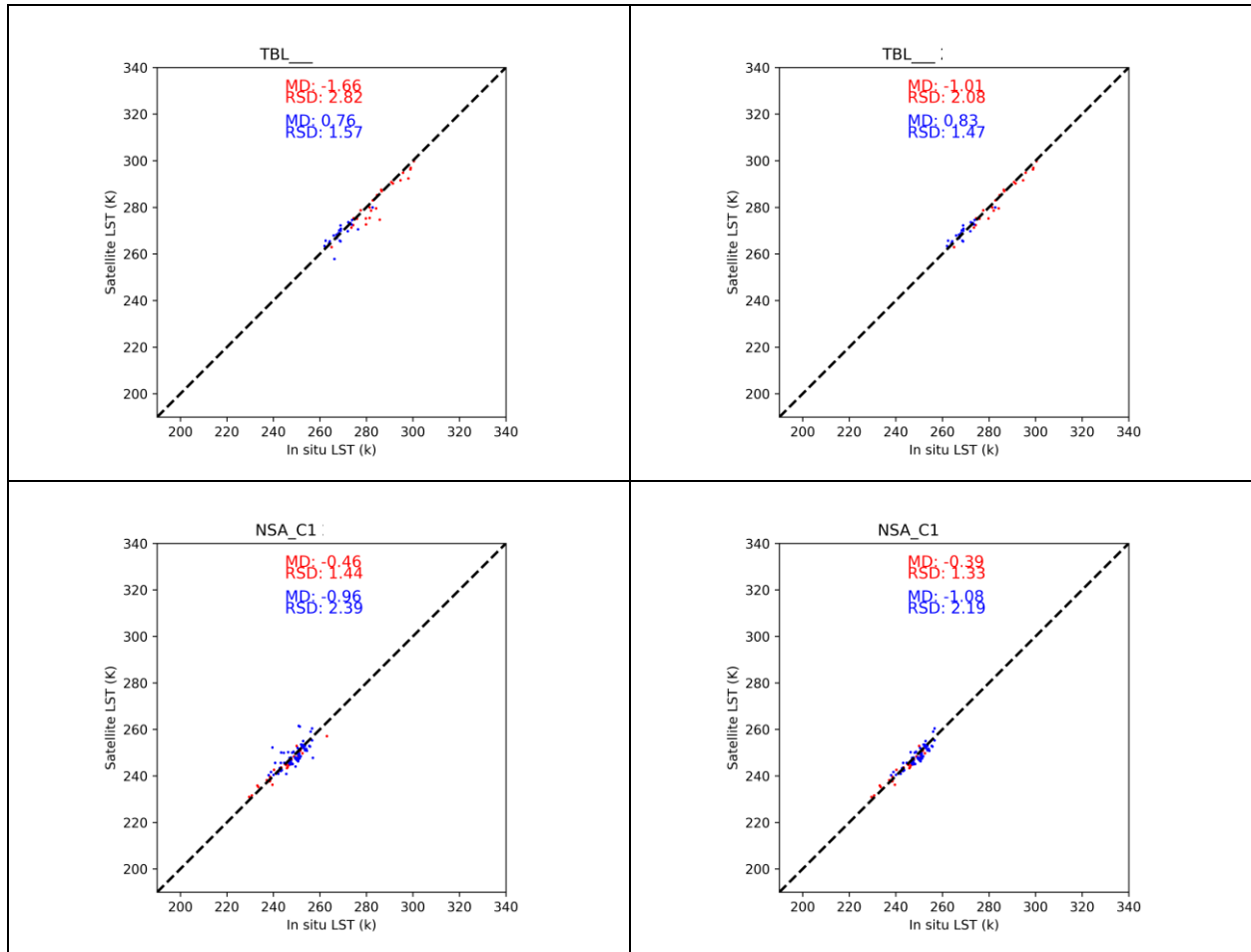


Figure 29: Validation of the SL_2_LST product in December 2022 for SLSTR-A (left) and SLSTR-B (right) at seven Gold Standard in situ stations of the SURFRAD network plus two Gold Standard station from the ARM network. The matchups are split between daytime (red) and night-time (blue).

As with past cycles, cloud has reduced the number of matchups per station to single figures for most stations during day or night, with some missing statistics entirely. It is therefore challenging to determine robust statistics. The cumulative statistics are presented in each Annual Report. Nonetheless, it can be seen that overall the matchups are in general close to the 1:1 line with very few outliers. No systematic bias is evident from these matchups.

6.2 Category-C validation

Category-C validation uses inter-comparisons with similar LST products from other sources such as other satellite sensors, which give important quality information with respect to spatial patterns in LST deviations. Here we compare the SL_2_LST product from both SLSTR-A and SLSTR-B with the operational SEVIRI L2 product available from the LSA SAF. The typical uncertainty of the SEVIRI L2 product ranges between ~1 K over much of Africa and ~3 K over the deserts. The results can be summarised:

Table 11: Median differences in K from the intercomparison of the SL_2_LST product with respect to the operational LSA SAF SEVIRI LST product for December 2022

Continent	SLSTR-A		SLSTR-B	
	Day	Night	Day	Night
Africa	-0.1	-0.1	-0.1	-0.1
Europe	1.1	1.3	1.2	1.3

For both Africa and Europe, the median differences across the continent for both SLSTR-A and SLSTR-B are relatively small, with very few locations with larger differences. The median is used to minimise the impact of any outliers. This is the same for both SLSTR-A and SLSTR-B and is primarily driven by differences in viewing geometry between the SLSTR instruments and SEVIRI and is expected, and in agreement with previous studies of polar orbiting matchups with SEVIRI (Ghent et al., 2017; Trigo et al., 2008). Eastern matchups (such as over the Arabian Peninsula and north-eastern Europe) are towards the edge of the SEVIRI disk and therefore represent large viewing angles. At these extreme viewing angles it is expected that SLSTR LST would be increasingly higher than SEVIRI LST, and the SEVIRI uncertainty increases above 3 K at these extreme angles. For both daytime and night-time the differences are mainly < 1K for Africa for both SLSTR-A and SLSTR-B. During daytime differences are over 1K for Europe as a result of increasing differences due to geometry as days get warmer. Differences are not the same as previous cycles for both Europe and Africa which may indicate responses due to changing seasons.

Other analysis can be summarised as follows:

- ❖ Differences with respect to biomes tend to be larger during the day for surfaces with more heterogeneity and/or higher solar insolation
- ❖ Differences increase for both day and night towards the edge of the SEVIRI disk as the SEVIRI zenith angles become larger

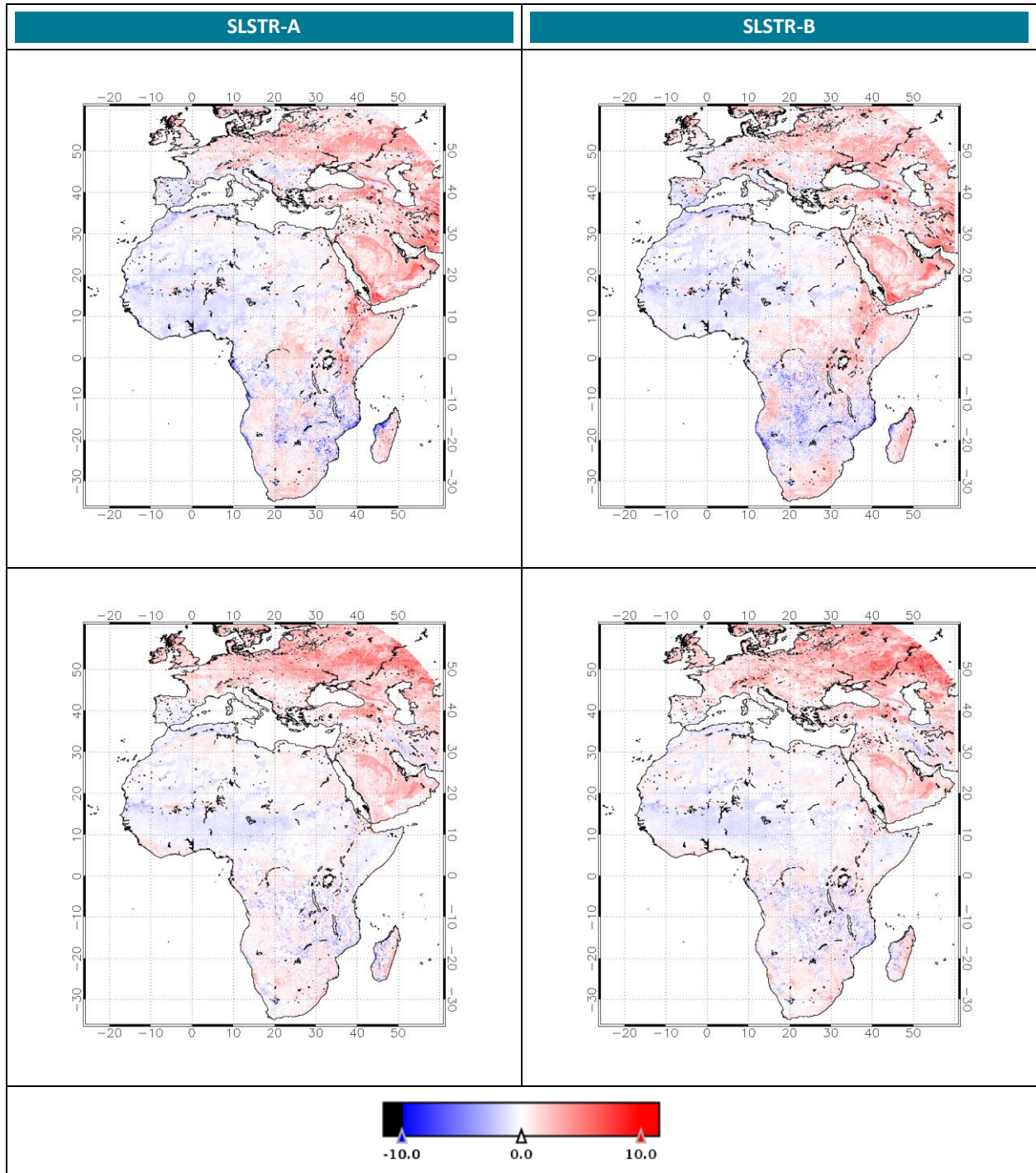


Figure 30: Intercomparison of the SL_2_LST product with respect to the operational LSA SAF SEVIRI LST product for December 2022 for SLSTR-A (left) and SLSTR-B (right). Daytime composites are in the top row and Night-time composites are in the bottom row.

While some of these differences are > 1 K they are all within the corresponding uncertainty of SEVIRI at the pixel-scale (> 2 K), and so the **two products can be assessed as being consistent.**

6.3 Level-3C Assessment

To better understand the global product and identify any gross issues Level-3 evaluation is also performed. Here we generate monthly daytime and night-time 0.05° composites of the LST field and corresponding sampling ratios. The sampling ratios are derived as $\text{clear_pixels} / (\text{clear_pixels} + \text{cloudy_pixels})$.

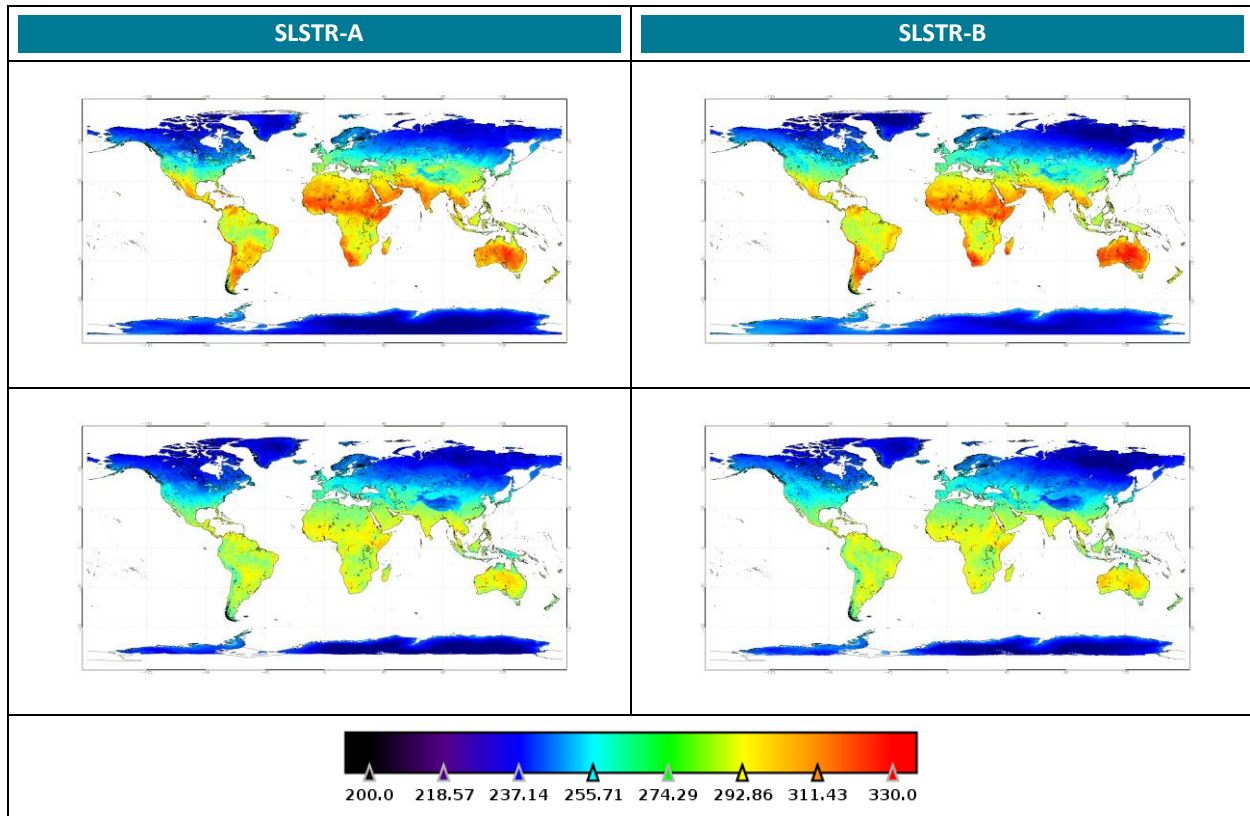


Figure 31: Monthly composites at 0.05° of LST for December 2022 for SLSTR-A (left) and SLSTR-B (right). Daytime composites are in the top row and Night-time composites are in the bottom row.

 <p>OPT-MPC Optical Mission Performance Cluster</p>	<p>Optical MPC</p> <p>Data Quality Report – Sentinel-3 SLSTR</p> <p>March 2023</p>	<p>Ref.: OMPC.ACR.DQR.04.03-2023</p> <p>Issue: 1.1</p> <p>Date: 14/04/2023</p> <p>Page: 51</p>
---	---	--

6.4 References

- Augustine, J.A. and Dutton, E.G. (2013). Variability of the surface radiation budget over the United States from 1996 through 2011 from high-quality measurements. *Journal of Geophysical Research: Atmospheres* 118, 43–53.
- Ghent, D. J., Corlett, G. K., Göttsche, F.-M., & Remedios, J. J. (2017). Global land surface temperature from the Along-Track Scanning Radiometers. *Journal of Geophysical Research: Atmospheres*, 122. <https://doi.org/10.1002/2017JD027161>
- Guillevic, P., Göttsche, F., Nickeson, J., Hulley, G., Ghent, D., Yu, Y., Trigo, I., Hook, S., Sobrino, J.A., Remedios, J., Román, M. & Camacho, F. (2017). Land Surface Temperature Product Validation Best Practice Protocol. Version 1.0. In P. Guillevic, F. Göttsche, J. Nickeson & M. Román (Eds.), *Best Practice for Satellite-Derived Land Product Validation* (p. 60): Land Product Validation Subgroup (WGCV/CEOS), doi:10.5067/doc/ceoswgcv/lpv/lst.001
- Morris, V.R. Infrared Thermometer (IRT) Handbook (ARM TR-015) (2006). Technical report, Atmospheric Radiation Measurement, Climate Research Facility, U. S. Department of Energy.
- Schneider, P., Ghent, D., Corlett, G., Prata, F., and Remedios, J. (2012). AATSR validation: LST validation protocol. Internal publication, UL-NILU-ESA-LST-LVP Issue 1 Revision 0, page 1-39. <http://lst.nilu.no/Portals/73/Docs/Reports/UL-NILU-ESA-LST-LVP-Issue1-Rev0-1604212.pdf>.
- Stoffel, T. Ground Radiation (GNDRAD) Handbook (ARM TR-027) (2006). Technical report, Atmospheric Radiation Measurement, Climate Research Facility, U. S. Department of Energy.
- Trigo, I. F., Monteiro, I. T., Olesen, F., & Kabsch, E. (2008). An assessment of remotely sensed land surface temperature. *Journal of Geophysical Research*, 113(D17), D17108. <https://doi.org/10.1029/2008JD010035>

	<p>Optical MPC</p> <p>Data Quality Report – Sentinel-3 SLSTR</p> <p>March 2023</p>	<p>Ref.: OMPC.ACR.DQR.04.03-2023</p> <p>Issue: 1.1</p> <p>Date: 14/04/2023</p> <p>Page: 52</p>
---	---	--

7 Level 2 FRP validation

7.1 Introduction

Validation of the SLSTR L2 FRP products can be performed using either in-situ data such as airborne measurements or using reference satellite products for inter-comparison. Active fires in situ data are unfortunately not frequent enough to validate fire satellite data products on an operational basis. We are then using NASA Moderate-Resolution Imaging Spectroradiometer (MODIS) as reference fire data for inter-comparisons.

This inter-comparison is aiming at validating two elements:

1. The detection of fire regarding position and extent in time and space.
2. Once a fire has been detected, the computation of the Fire radiative power either for each pixel confirmed as an active fire or for the entire fire cluster.

Level 2 Fire Radiative Power products have been compared with respect to an independent operational reference product (MODIS Terra MOD14 FRP). In particular, to evaluate the performance of the night-time algorithm, an inter-comparison between the SLSTR NTC FRP (both from SLSTR-A and SLSTR-B) and the FRP retrieved from the similar MODIS MOD14 product was designed and conducted, giving important information on both spatial patterns of fire detection and FRP quantification (see previous reports for complete results). The same intercomparison is now performed over daytime products.

The inter-comparison procedure, initially based on previous work from M. Wooster and W. Xu on the FRP Prototype and on the evaluation of SEVIRI fire data, is divided into two main parts, the first one related to active fire (AF) pixel detection and omission and commission fire pixels, and the second to fire clusters. The SLSTR FRP NTC product (both SLSTR-A and SLSTR-B) has been released to the public on the 19th August 2020.

The current processing baseline for SLSTR-A and SLSTR-B FRP products is FRP_NTC.004.08.00 and was deployed in the Land processing centres on 23rd August 2022 for SLSTR-A and on 9th September 2022 for SLSTR-B. Only minor corrections were included, with no impact on data quality. The previous baseline (deployed on 28th February 2022 for both SLSTR-A and SLSTR-B) included an updated FRP algorithm, called FRP V2. This updated algorithm was based on the previous one, with similar night-time algorithm, but includes improved thermal fire detection over daytime products. In addition, fire detection is now also performed using SWIR channels (note however that this functionality is not yet part of this validation report and will be included in the following ones).

This report will first focus on the Fires detected **during night-time** using FRP V2 algorithm **and thermal measurements only**, considering October, November and December 2022 data products (three 27-days orbital cycles). Then a section will be dedicated to the quality of FRP V2 algorithm with validation of **the day-time fire detection using thermal radiometric measurements** between January and March 2023 (three 27-day orbital cycles).

In the current FRP algorithm, AF detection is performed using a mixed thermal band: by default, the S7 brightness temperature are considered. However, the F1 channel is used instead for pixels where the S7 channel saturates. Same replacement is also performed for each neighbour included in a 11 × 11 pixel window centred over this saturated pixel and either having a S7 brightness temperature higher than 300 K or a difference between S7 and S8 brightness temperatures higher than 10 K. The fire detection during night-time remains similar to FRP V1 and the FRP value are computed using F1 measurements.

	Optical MPC Data Quality Report – Sentinel-3 SLSTR March 2023	Ref.: OMPC.ACR.DQR.04.03-2023 Issue: 1.1 Date: 14/04/2023 Page: 53
---	--	---

The SLSTR FRP validation uses inter-comparisons with similar FRP products from other sources such as other satellite sensors, which give important quality information with respect to active fire detection and fire clusters characterisation. Here we compare the SL_2_FRP product from both SLSTR-A and SLSTR-B with the operational MODIS MOD14 FRP product (from MODIS Terra) available from the LAADS DAAC. It is important to note that the employed products have slightly different overpass times, implying that the two sensors do not observe fires in the exact same configuration nor with the same atmospheric conditions. Thus, for these reasons, and for the nature of the procedure delineated below, this inter-comparison should not be interpreted as a full validation exercise but rather as a check of the consistency of the FRP products derived from SLSTR with the ones from MODIS. The inter-comparison procedure is divided into two main parts. The first part is related to omission and commission fire pixels, i.e., fire pixels detected by MODIS without any SLSTR fire pixel in a 7x7 window around it (omissions), and fire pixels detected by SLSTR without any MODIS fire pixel in a 7x7 window around it (commissions). The second part is related to the characterisation of fire clusters, i.e., groups of one or more pixels spatially adjacent to each other and corresponding to a single fire.

The validation procedure is described in the following:

Part 1: omission and commission fire pixels between SLSTR FRP and MODIS MOD14:

- ❖ Select areas of high fire activity during the relevant time period and fetch all the relative SL_2_FRP scenes (both SLSTR-A and SLSTR-B);
- ❖ Discard all scenes that do not contain active fire pixels;
- ❖ Select and download matching MODIS MOD14 data with overpass time within ± 6 minutes of those of SLSTR and covering the same area of interest, and discard all scenes that do not have a matching MOD14 product;
- ❖ Restrict observations to a scan angle of $\pm 30^\circ$ or equivalent pixel area of 1.7 km² to avoid edge-of-swath data, and restrict to the common area of detection between the two products;
- ❖ Discard all scenes that do not contain active fire pixels after the restriction step;
- ❖ Re-project the MODIS pixels to the SLSTR F1 grid. If multiple MODIS active fire pixels (AFP) are present in the same equivalent SLSTR grid cell, their combined FRP is used;
- ❖ Evaluate SLSTR FRP commission fire pixels, i.e., when there is a fire pixel in the SLSTR grid without any MOD14 fire pixel in a 7x7 window around it;
- ❖ Evaluate SLSTR FRP omission fire pixels, i.e., when there is a MOD14 fire pixel without any SLSTR fire pixel in a 7x7 window around it;
- ❖ Find and evaluate fire pixels detected by both sensors.

Part 2: Fire Cluster FRP comparison between SLSTR FRP and MODIS MOD14:

- ❖ Apply an atmospheric correction to MODIS FRP data, calculated using transmittance and water vapour content of the column above the fire pixel;
- ❖ Starting from the fire pixels detected by both sensors, find all the fire clusters detected by both SLSTR and MODIS, i.e., groups of one or more pixels spatially adjacent to each other and corresponding to a single fire; cases where a single SLSTR cluster corresponds to multiple MOD14 clusters and/or vice versa are merged together and the total FRP is used;
- ❖ Compute the total FRP for all active fire pixels in each fire cluster for MODIS and SLSTR data.

- ❖ Check for cloud/water/detection flags around each fire cluster that might affect the FRP value; if none is present, the cluster is flagged as well-detected;
- ❖ If necessary, check the SLSTR S7-S8 difference for possible issues and mismatches with the detected fire clusters;
- ❖ Generate statistics and analysis based on all the fire clusters detected by both MODIS and SLSTR.

Using the procedure delineated above, fire pixels from **five areas of high fire activity between 1st January 2022 and 31st March 2023** were aggregated and compared. In particular, the four areas of interest are: north part of South-America (Colombia, Suriname, Venezuela, Panama), Central Africa (forests band), USA and Central America (Cuba, Guatemala, Mexico) and the south-east of Asia (India, Bangladesh, Myanmar, Thailand, Cambodia, Vietnam,...), see Figure 32. From around three thousand SLSTR scenes encompassing these areas, around 240 products (day-time and night-time) which respected all the criteria delineated above were selected to perform this analysis.

The report includes a study and analysis of the performance of **SLSTR FRP night-time and day-time** algorithms. Summaries of the results are reported respectively in Table 12 and Table 13.

7.2 Night-Time Validation

Night-time validation is performed considering three 27-days orbital cycle and 100 SLSTR FRP (2,154 clusters) products are compared to MODIS MOD14 fire products to identify fires and other thermal anomalies for the months **January, February, and March 2023**.

Note also that the summaries from previous DQRs has been added to the table for information. The comparison must be done with caution as we compare different time periods (validation over 3 months versus over 2 months) and different validation sites (areas of high fire activity are re-evaluated at each period).

Table 12: Summary of the inter-comparison between night-time SLSTR FRP and MODIS FRP – January, February and March 2023. Results from previous comparison obtained between October and December 2022, July and August 2022, April and May 2022 with FRP V2 have been added respectively in the second, third and fourth column for information and comparison.

Variable	Value (Jan. 2023 – Mar. 2023 ; FRP V2)	Value (Oct. 2022 – Dec. 2022 ; FRP V2)	Value (July – Sept. 2022 ; FRP V2)	Value (April – May 2022 ; FRP V2)
Numbers of commission AFP	15,149 (56.3% of Total SLSTR AFP)	13,093 (55.1% of Total SLSTR AFP)	20,092 (62.3% of Total SLSTR AFP)	5,531 (53.7% of Total SLSTR AFP)
Numbers of omission AFP	567 (2.1% of Total SLSTR AFP)	694 (2.9% of Total SLSTR AFP)	883 (2.7% of Total SLSTR AFP)	401 (3.9% of Total SLSTR AFP)
FRP of commission AFP (MW)	37,392	40,359	58,380	20,164
FRP of omission AFP (MW)	14,459	30,641	34,123	7,940
Number of SLSTR AFP detected by both sensors	11,762 (43.7% of Total SLSTR AFP)	10,665 (44.9% of Total SLSTR AFP)	12,147 (37.7% of Total SLSTR AFP)	4,775 (46.3% of Total SLSTR AFP)

Number of MOD14 AFP detected by both sensors	3,481 (86.0% of Total MOD14 AFP)	3,341 (82.8% of Total MOD14 AFP)	4,089 (82.1% of Total MOD14 AFP)	1,798 (81.8% of Total MOD14 AFP)
Total number of AFP detected by SLSTR	26,911	23,758	32,239	10,306
Total number of MOD14 AFP	4,048	4,035	4,972	2,199
Mean number of SLSTR AFP per cluster	6.4	6.4	5.9	5.8
Total SLSTR FRP within clusters (MW)	70,529	81,672	95,704	27,436
Mean SLSTR FRP per cluster (MW)	41.2	54.0	50.4	42.9
Median SLSTR FRP per cluster (MW)	18.9	21.0	21.7	20.3
Mean number of MOD14 AFP per cluster	1.8	1.9	1.9	1.9
Total MOD14 FRP within clusters (MW)	58,894	70,530	85,814	23,367
Mean MOD14 FRP per cluster (MW)	34.8	46.7	45.2	36.5
Median MOD14 FRP per cluster (MW)	11.7	13.6	14.3	13.0
Mean bias of FRP per cluster (MW)	6.9	7.4	5.2	6.4
Median of FRP scatter per cluster (MW)	5.0	6.0	5.2	5.2
Root-mean-square deviation of FRP per cluster	48	59	71	40
25-50-75 percentiles of SLSTR clusters FRP	10.6, 18.9, 34.8	12.1, 21.0, 40.2	12.1, 21.7, 42.6	11.2, 20.3, 43.7
25-50-75 percentiles of MOD14 clusters FRP	7.2, 11.7, 23.3	7.8, 13.6, 29.5	8.1, 14.3, 31.2	7.8, 13.0, 28.7

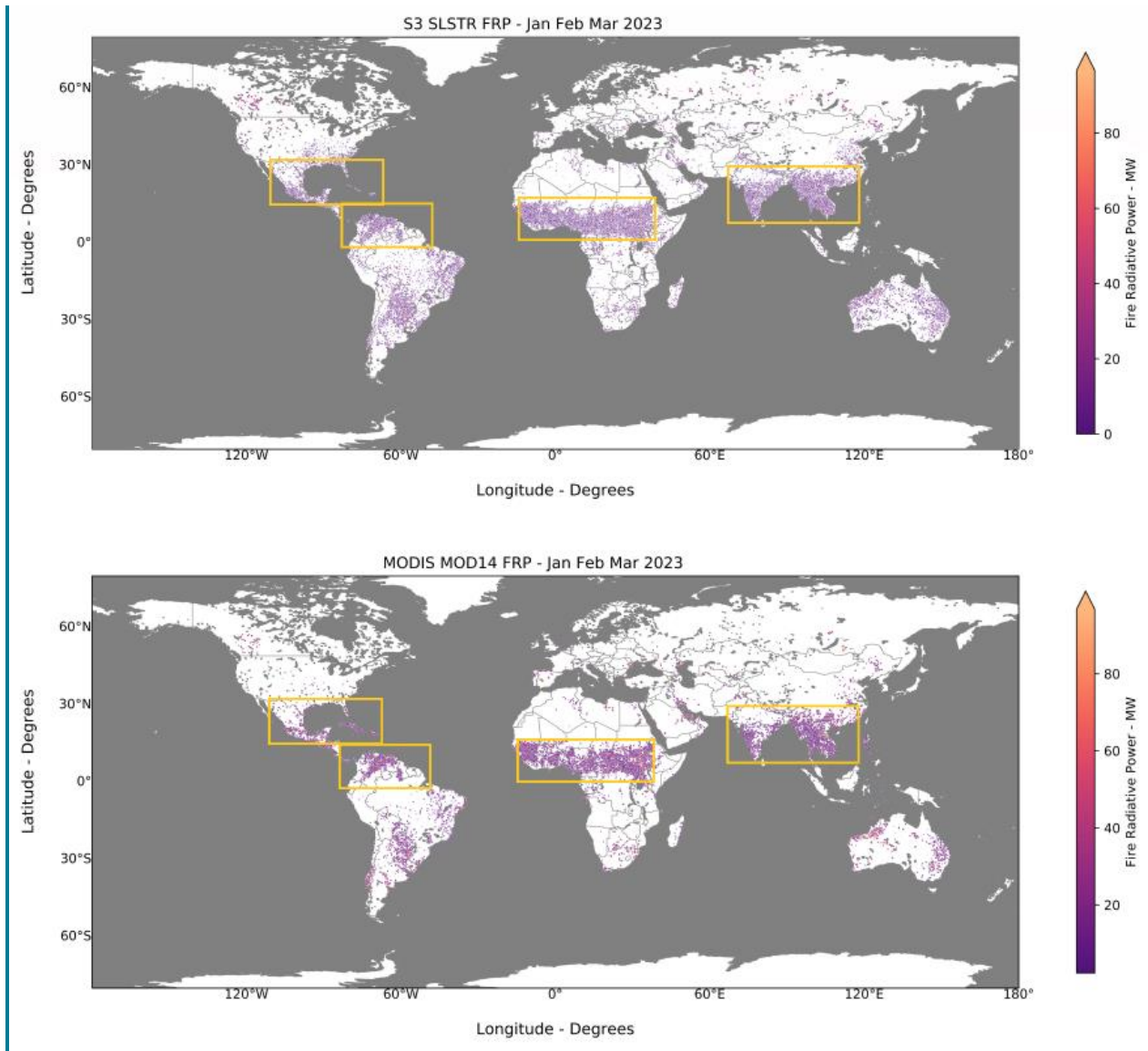


Figure 32: Areas of high fire activity selected for the inter-comparison. The base map shows night-time fires detected by SLSTR (top) and MODIS (bottom) for the months of January, February and March 2023.

Overall, **there is good agreement between SLSTR FRP and MODIS FRP**, as can be seen in Table 12. The comparison shows that SLSTR detects in general more fire pixels than MODIS (26,911 vs 4,048), albeit many of them with very low FRP. Furthermore, there is a large number of commission fire pixels and a low number of omission fire pixels. Such pixels indicate fires that were detected only by one sensor. However, these are not necessarily incorrect/missed detections.

It is important to highlight, that the two sensors observe the scenes at slightly different times (the MODIS product has to be within an interval of ± 6 minutes with respect to the SLSTR acquisition). This difference in time translates into different conditions of the observed fires and also of the cloud coverage. A fire could move, increase/decrease in extent and power, whereas clouds could cover different portions of the image. On the other hand, a fraction of these pixels may represent real fires that are undetected by MODIS but are detected by the SLSTR product -

for example because of the use of the smaller pixel footprint F1 channel – or vice versa. For these reasons, the reported values should not be interpreted as full validation, but rather as indication of the consistency between the two sensors.

It seems that MODIS detects less fires in Northern hemisphere than SLSTR, whereas comparison are quite close in Southern hemisphere. This point will be approached in the third section of this report by studying biome dependencies of the detection. The results show an important number of commission fire pixels in this area and the northern hemisphere provides more commissions than omissions in night-time.

A comparison of fire pixels detected distinctly by Sentinel 3A and Sentinel 3B is visualised in Figure 33.

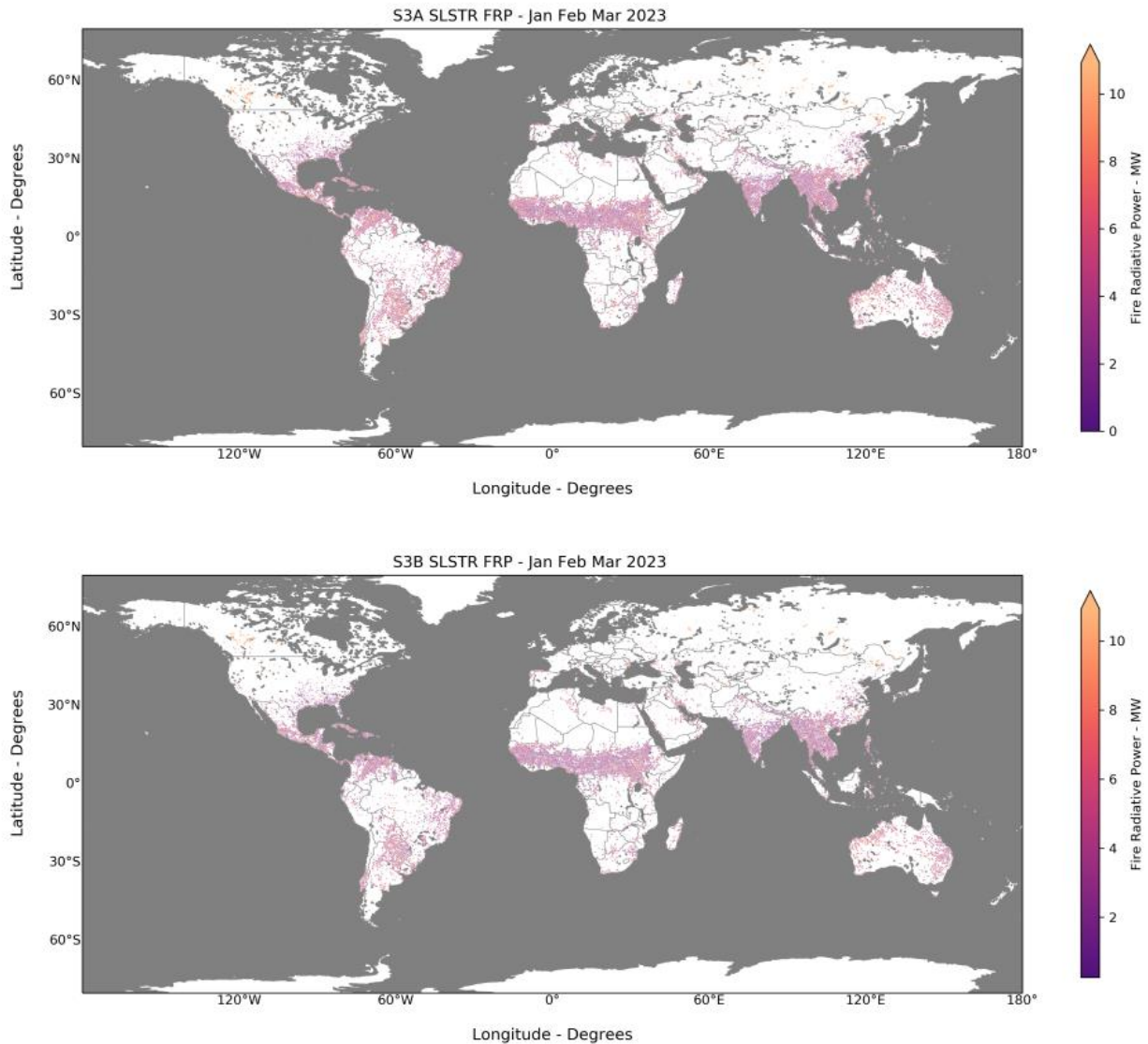


Figure 33: Night-time fires detected by Sentinel 3A (top) and Sentinel 3B (bottom) for the months of January, February and March 2022.

The fire pixels dispersion is similar for both satellites Sentinel A and B in all areas of high fire activity for night-time SLSTR products. However, for night-time and day-time **Sentinel 3B provide respectively 51.4% and 51.9% of the fire pixels detection**. Considering both night-time and day-time MOD14 FRP data, Aqua provides 67.9% of the fire pixels detection. However, Terra and Aqua respectively crosses the equator from north to south at roughly 10:30 a.m. and 1:30 p.m. local time (closer to maximum fire activity).

To gain more insight into the differences between fire detection and FRP estimation, we introduce **the notion of fire clusters**, as illustrated in Figure 34:

- ❖ The left-hand side panel shows all the pixels confirmed as active fires. The FRP product will provide the position and an equivalent FRP value for all these pixels;
- ❖ However, some of these pixels are close enough to be interpreted as a single fire event, called fire cluster (see distribution of the pixels into three distinct fire clusters in the middle panel). Each cluster will then be analysed separately and each single FRP value will be computed taken into account the whole cluster;
- ❖ The right-hand side panel represents 3 fire clusters, each of them associated with a global average FRP and a specific geographical extent (i.e. the number of fire pixel included in this cluster). This cluster distribution will be the basis of the following validation activities.

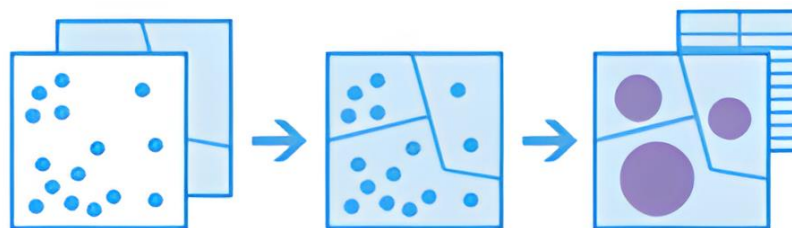


Figure 34: Cluster formation for a specific area. See text for details.

In the following, we are then comparing clusters detected by MODIS and by SLSTR. In particular, if a fire cluster is detected by both satellites, the number of individuals fire pixels inside this cluster can be different for SLSTR and MODIS. These proportions for the two sensors are visualised in Figure 35.

Number of fires detected by SLSTR VS Number of fires detected by MODIS

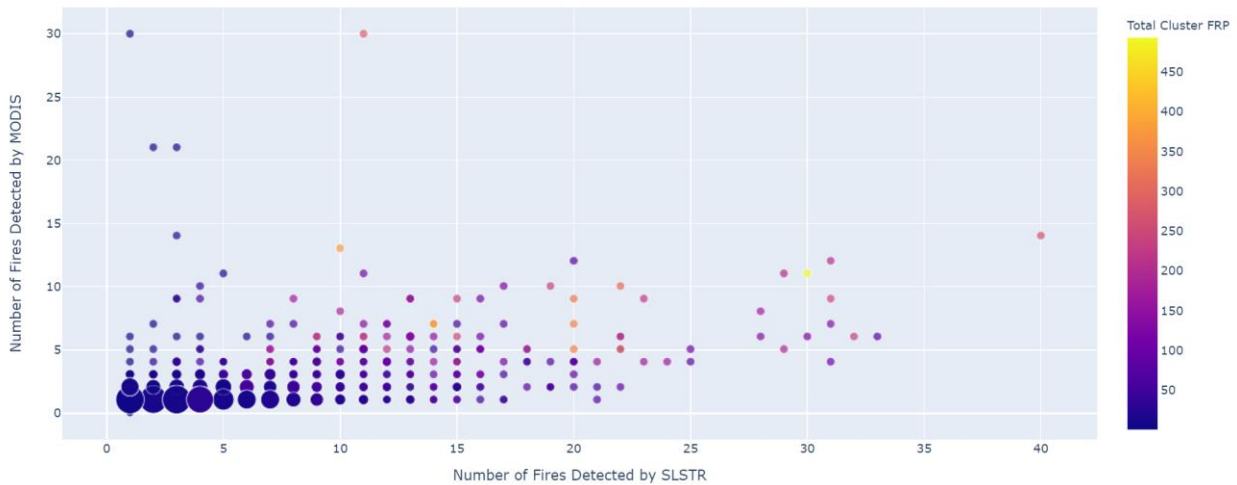


Figure 35: Scatterplot between the number of fires detected by both sensors (night-time). SLSTR values are reported on the x-axis, whereas MODIS ones are on the y-axis.

The graph compares the number of fire pixels detected by SLSTR and MODIS over a single cluster. Each circle counts then for a fire cluster and its coordinates on the graph indicates the number of fire pixels detected by SLSTR (X-axis) and MODIS (Y-axis).

The first information provided by this graph is then that all clusters detected by MODIS are also detected by SLSTR (no circle on the Y axis), where we can have small fire cluster detected by SLSTR and missed by MODIS (see the small point on X-axis).

In addition, the size of each circle specifies the number of cases with a similar MODIS/SLSTR fires detection ratio (i.e. the same couple of coordinates corresponding to the same proportion of fires detected by both sensors) in the manner of a 3D graph. The colour of each point indicates the total Fire Radiative Power of the cluster detected by satellites.

Figure 36 shows that:

- ❖ **SLSTR detects more fire pixels than MODIS in a single cluster.** However, these clusters are associated with low FRPs and with larger circle size indicating a higher sensitivity of SLSTR to smaller fires.
- ❖ Considering large fire clusters, there are always associated with large FRP and the ratio SLSTR/MODIS regarding the number of pixel fires included in these cluster shows again a **higher sensitivity of SLSTR with more individual pixel detected** as active fires.

The **distribution of FRP for fire clusters detected by both sensors is quite similar**, even though MODIS exhibits a higher peak for low FRP values and SLSTR shows a higher curve for intermediate values. Figure 37 further highlights the fact that SLSTR fire clusters include more pixels than for MODIS, many of them with very low FRP, and the total FRP of all clusters is higher for SLSTR. This result is however heavily affected by a few outliers with high FRPs.

Contrary to the case of omission/commission fire pixels, the cluster analysis includes a check on the relevant quality flags, in particular those related to water or clouds in the background window around the fire cluster. Thus, the results of the cluster analysis are more robust against differences in the atmospheric conditions or cloud masking algorithm. Nonetheless, the detections could still be affected by the differences in observation time.

Cyclic Validation Cluster Distribution

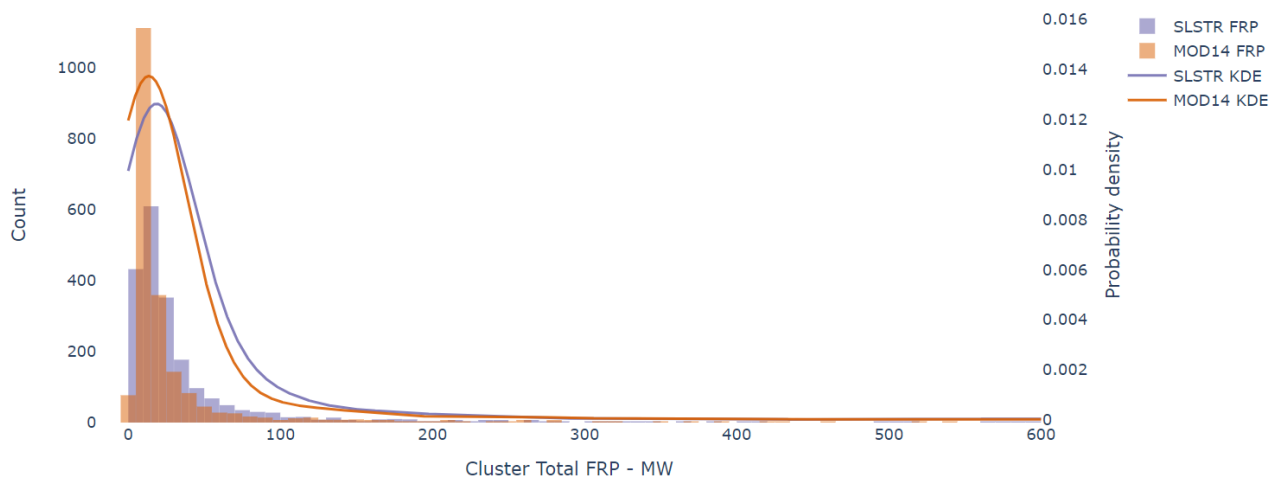


Figure 36: Distribution of the FRP for fire clusters detected by both sensors. The lines represent kernel density estimates (KDE) computed over the bar plot.

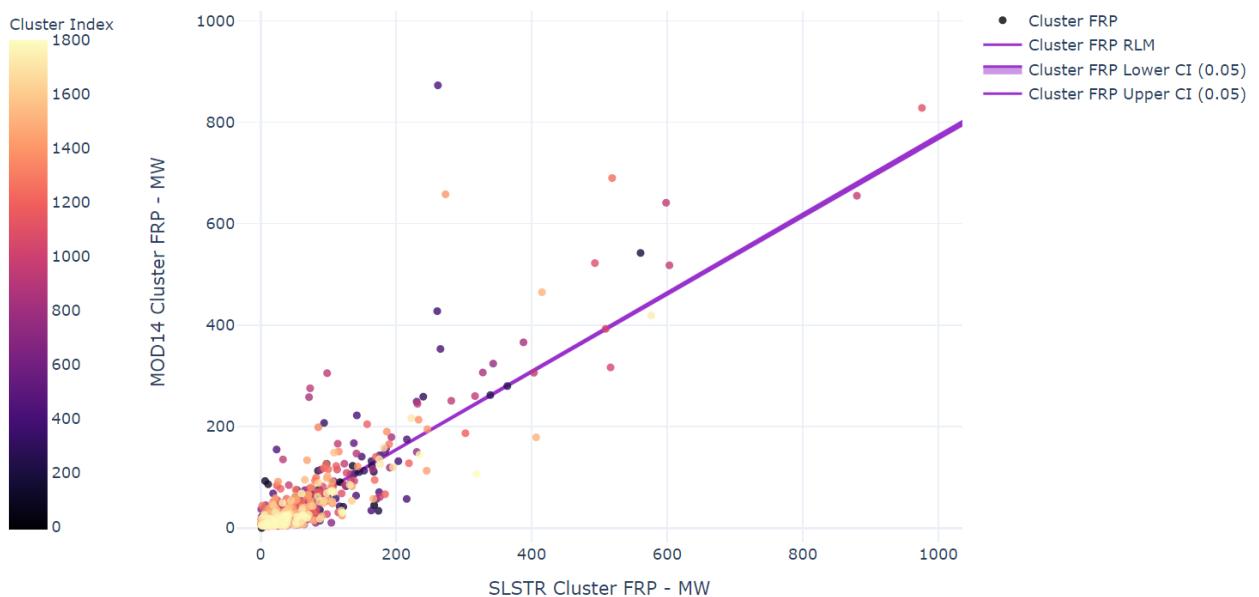


Figure 37: Scatterplot between the FRP of fire clusters detected by both sensors. SLSTR values are reported on the x-axis, whereas MODIS ones are on the y-axis. The regression line (with a shaded 0.05 confidence interval) is obtained with a robust linear method (RLM), which is less affected by outliers. The scatter points are color-coded according to their cluster number, so that they can be traced back to the original datasets. $R = 0.940$, slope of regression line = 0.875.

The ratio SLSTR/MODIS regarding the number of included pixels is also closer to one for large FRP values. It is worth highlighting that high-FRP fire clusters (>800 MW) strongly impact the correlation to the regression line. The coefficient of determination of the regression model R^2 has never been this close to one considering FRP V2 implemented in February 2022.

7.3 Day-Time Validation

Day-time validation is performed considering three 27-days orbital cycle and 123 SLSTR FRP (4,709 clusters) products are compared to MOD14 fire products to identify fires and other thermal anomalies for the months January, February and March 2023.

This additional study has been carried out to evaluate the performance and the sustainability of the implementation of the FRP IPF V2. The main parameters of the inter comparisons between SLSTR and MODIS data remain the same for consistency.

Using the same procedure previously delineated, fire pixels from **five areas of high fire activity between 1st January and 28th March 2023** were aggregated and compared considering the same areas of interest, see Figure 38. A summary of the results is reported in Table 13.

Table 13: Summary of the inter-comparison between SLSTR FRP and MODIS FRP – January, February and March 2023. Results from previous comparison obtained between October and December 2022, July and August 2022, April and May 2022 with FRP V2 have been added respectively in the second, third and fourth column for information and comparison.

Variable	Value (Jan. 2023 – Mar. 2023; FRP V2)	Value (Oct. 2022 – Dec. 2022; FRP V2)	Value (Jul. 2022 – Sept. 2022; FRP V2)	Value (Apr. 2022 – May. 2022; FRP V2)
Numbers of commission AFP	4,326 (26.6% of Total SLSTR AFP)	5,344 (47.9% of Total SLSTR AFP)	7,613 (48.6% of Total SLSTR AFP)	3,071 (42.7% of Total SLSTR AFP)
Numbers of omission AFP	6,226 (38.3% of Total SLSTR AFP)	3,693 (33.1% of Total SLSTR AFP)	5,720 (36.5% of Total SLSTR AFP)	2,484 (31.5% of Total SLSTR AFP)
FRP of commission AFP (MW)	56,702	67,342	96,572	40,883
FRP of omission AFP (MW)	218,462	146,446	191,942	52,621
Number of SLSTR AFP detected by both sensors	11,931 (73.4% of Total SLSTR AFP)	5,819 (52.1% of Total SLSTR AFP)	8,054 (51.4% of Total SLSTR AFP)	4,127 (57.3% of Total SLSTR AFP)
Number of MOD14 AFP detected by both sensors	8,720 (58.3% of Total MOD14 AFP)	4,421 (54.5% of Total MOD14 AFP)	5,845 (50.5% of Total MOD14 AFP)	2,947 (54.2% of Total MOD14 AFP)
Total number of AFP detected by SLSTR	16,257	11,163	15,667	7,198
Total number of MOD14 AFP	14,946	8,114	11,565	5,431
Mean number of SLSTR AFP per cluster	2.8	2.5	2.7	3.0

Variable	Value (Jan. 2023 – Mar. 2023; FRP V2)	Value (Oct. 2022 – Dec. 2022; FRP V2)	Value (Jul. 2022 – Sept. 2022; FRP V2)	Value (Apr. 2022 – May. 2022; FRP V2)
Total SLSTR FRP within clusters (MW)	212,125	73,916	156,059	56,580
Mean SLSTR FRP per cluster (MW)	55.5	48.0	59.0	64.1
Median SLSTR FRP per cluster (MW)	26.9	27.4	27.4	34.0
Mean number of MOD14 AFP per cluster	1.8	1.7	1.8	1.9
Total MOD14 FRP within clusters (MW)	190,612	68,320	143,963	51,904
Mean MOD14 FRP per cluster (MW)	49.9	44.3	54.4	58.9
Median MOD14 FRP per cluster (MW)	21.5	22.3	22.5	25.7
Mean bias of FRP per cluster (MW)	5.6	3.6	4.6	5.3
Median of FRP scatter per cluster (MW)	3.9	3.7	3.4	5.7
Root-mean-square deviation of FRP per cluster	67.3	58.9	64.0	66.0
25-50-75 percentiles of SLSTR clusters FRP	15.4, 26.9, 51.4	17.0, 27.4, 52.0	16.0, 27.4, 54.4	19.2, 33.9, 63.5
25-50-75 percentiles of MOD14 clusters FRP	11.9, 21.6, 45.8	13.0, 22.3, 42.9	12.2, 22.5, 48.6	13.5, 25.7, 50.4

The results remain relatively consistent with the previous one, with more fires detected by SLSTR than MODIS (16,257 vs 14,946) but the gap between satellites drastically decreased. The comparison shows that **SLSTR detects in general more fire pixels than MODIS and many of them with very low FRP**. For the first time since the implementation FRP V2, the number of omissions is higher than the number of commissions (and way higher than for night-time data). It means that there are more fire pixels detected by MODIS without any SLSTR fire pixel than the opposite. Also note that the total SLSTR and MODIS FRP power within clusters are three times higher than for the data in the previous report.

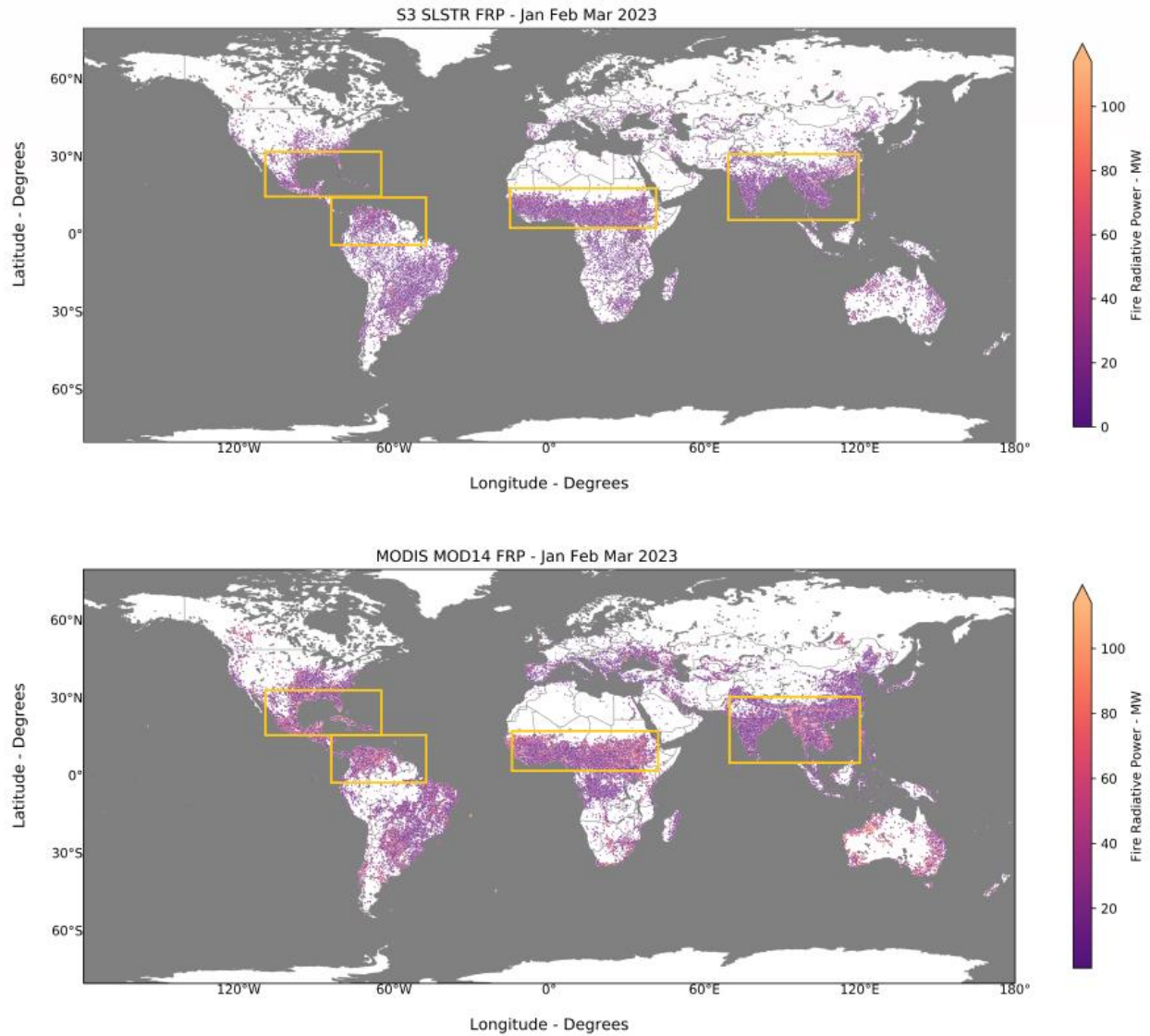


Figure 38: Areas of high fire activity selected for the inter-comparison. The base map shows day-time fires detected by SLSTR (top) and MODIS (bottom) for the months of January, February and March 2023.

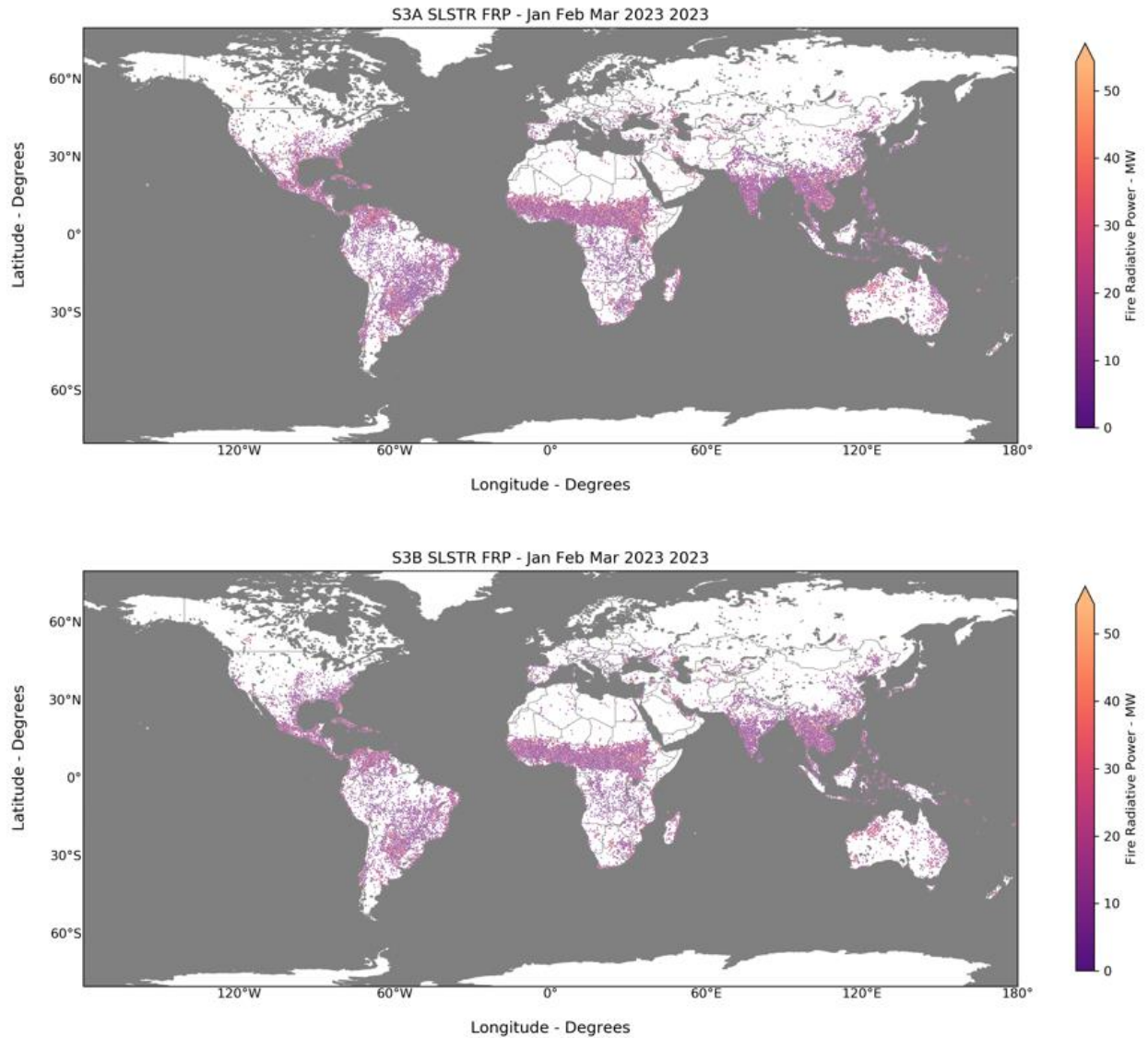


Figure 39: Day-time fires detected by Sentinel 3A (top) and Sentinel 3B (bottom) for the months of January, February and March 2023.

As for night-time data products, the fire pixels dispersion is similar for both satellites Sentinel-3 A and B in all the areas of high fire activity for day-time SLSTR products. But, contrary to night-time data, there are clearly more omissions fire pixels on the whole map.

Number of fires detected by SLSTR VS Number of fires detected by MODIS

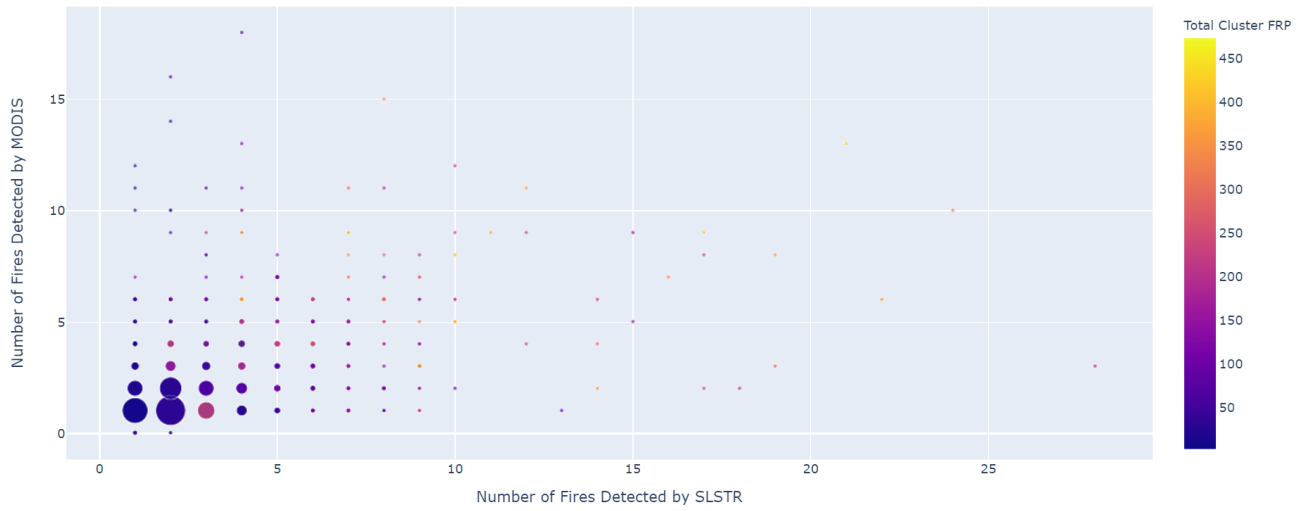


Figure 40: Scatterplot between the number of fires clusters detected by both sensors (day-time). SLSTR values are reported on the x-axis, whereas MODIS ones are on the y-axis.

MODIS detects more high-FRP fires while SLSTR detect more low-FRP fires.

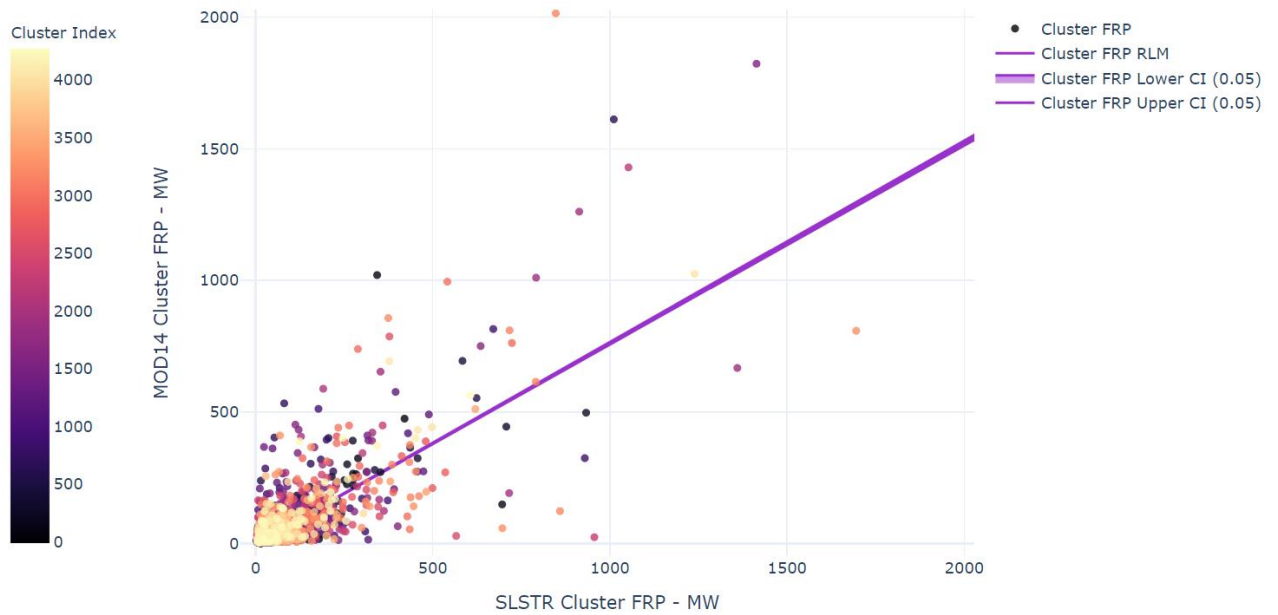


Figure 41: Scatterplot between the FRP of fire clusters detected by both sensors. SLSTR values are reported on the x-axis, whereas MODIS ones are on the y-axis. The regression line (with a shaded 0.05 confidence interval) is obtained with a robust linear method (RLM), which is less affected by outliers.

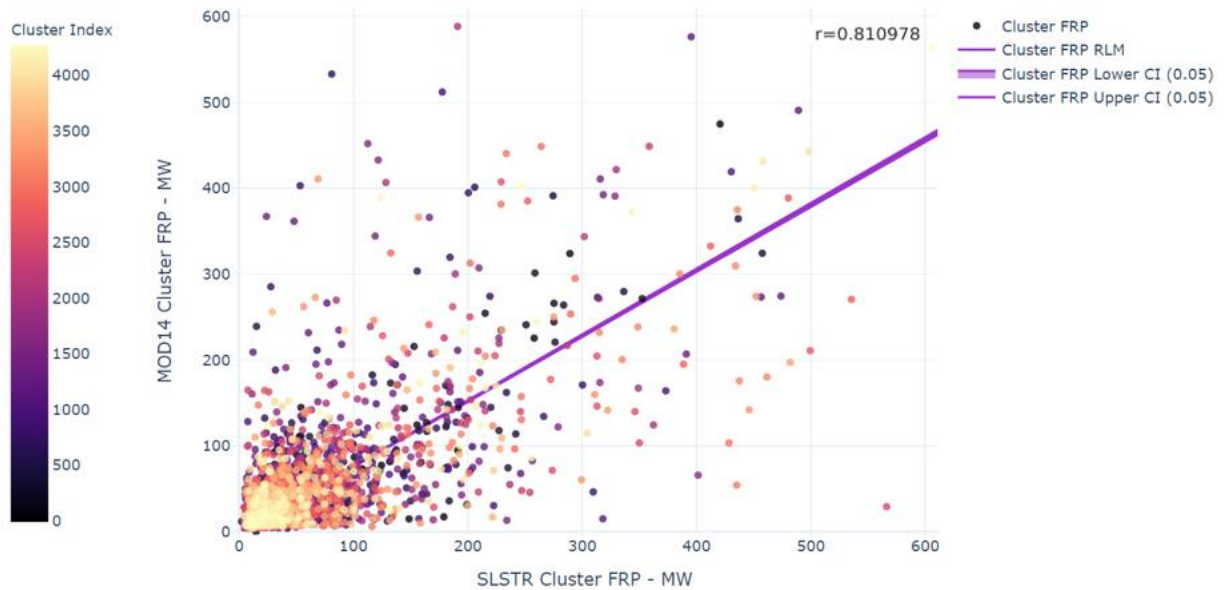


Figure 42: Scatterplot between the FRP of fire clusters detected by both sensors (close-up for FRP < 800 MW). SLSTR values are reported on the x-axis, whereas MODIS ones are on the y-axis. $R = 0.810$, slope of regression line = 0.775.

There is clearly a higher dispersion of the points than for night-time data.

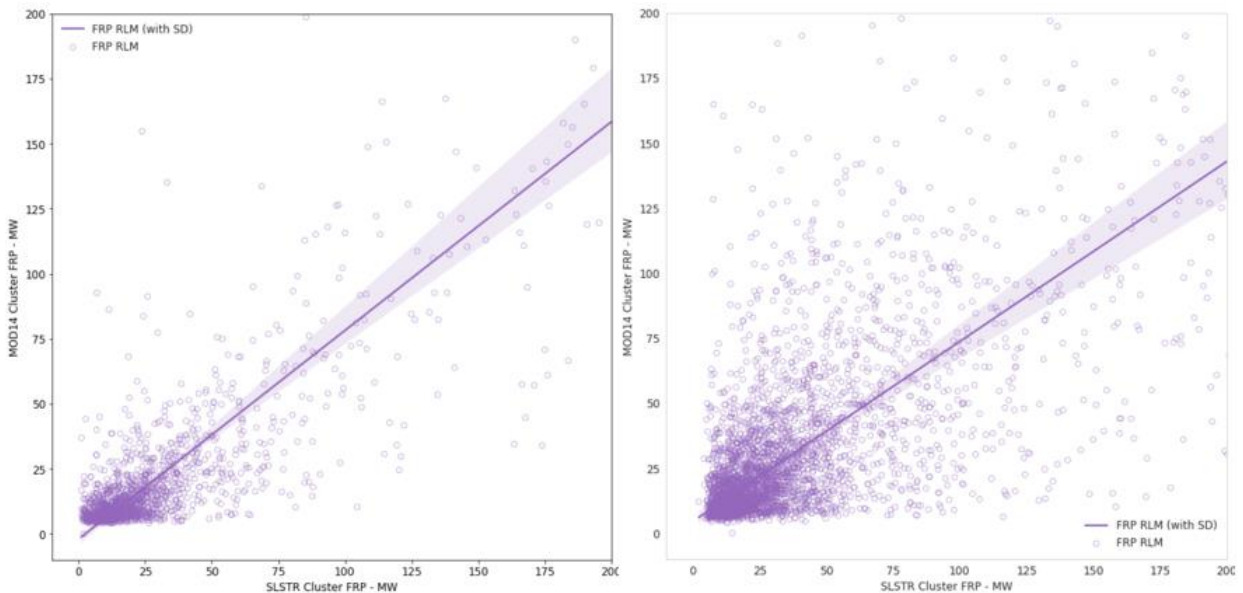


Figure 43: SLSTR vs MODIS clusters (FRP < 200) comparisons with regression line – night-time (left) and day-time (right).

This report has provided a detailed performance evaluation of SLSTR FRP product generated by Sentinel-3 A and Sentinel-3 B. On a “per-fire” basis there is a strong correlation ($r^2 = 0.94$ for night-time data and $r^2 = 0.81$ for day-time data) between the FRP recorded by Sentinel-3 and by MODIS, and a slope of the linear best fit line close to the unity (0.775 for day-time and 0.875 for night-time). Overall, the number of SLSTR AFP detected by both sensors reaches 44% of night-time products and almost 73% of day-time products.

	<p>Optical MPC</p> <p>Data Quality Report – Sentinel-3 SLSTR</p> <p>March 2023</p>	<p>Ref.: OMPC.ACR.DQR.04.03-2023</p> <p>Issue: 1.1</p> <p>Date: 14/04/2023</p> <p>Page: 67</p>
---	---	--

7.4 Biome influence

This part provides a preliminary study on biome influence on active fire detection. The idea is to deliver several statistics regarding detection performance of both MODIS and SLSTR instruments over different biome types. This study is carried out considering three 27-days orbital cycle and more than 200 SLSTR FRP (6,000 clusters overall night-time and day-time). Products are compared to MODIS MOD14 fire products to provide per-biome statistics for the months January, February and March 2023. Biome-based characterization limits the impact of high omission error rates caused by small and cool fires in different landscapes (cf. e.g. “Sentinel-2 MSI data for active fire detection in major fire-prone biomes: A multi-criteria approach”, Xikun Hu, Yifang Ban). It also helps identifying potential commission errors from soil-dominated pixels or highly reflective building rooftops.

The Global Land Cover 2000 classification¹ is used as a reference for this study. A summary of the results is reported in Table 3.

¹ <https://forobs.jrc.ec.europa.eu/products/glc2000/glc2000.php>

GLC Global Class (according to LCCS terminology)
1. Tree Cover, broadleaved, evergreen <i>LCCS > 15% tree cover, tree height > 3m</i> (Examples of sub-classes at regional level* : <i>closed > 40% tree cover; open 15-40% tree cover</i>)
2. Tree Cover, broadleaved, deciduous, closed
3. Tree Cover, broadleaved, deciduous, open <i>(open 15-40% tree cover)</i>
4. Tree Cover, needle-leaved, evergreen
5. Tree Cover, needle-leaved, deciduous
6. Tree Cover, mixed leaf type
7. Tree Cover, regularly flooded, fresh water (& brackish)
8. Tree Cover, regularly flooded, saline water, <i>(daily variation of water level)</i>
9. Mosaic: Tree cover / Other natural vegetation
10. Tree Cover, burnt
11. Shrub Cover, closed-open, evergreen <i>(Examples of sub-classes at reg. level *: (i) sparse tree layer)</i>
12. Shrub Cover, closed-open, deciduous <i>(Examples of sub-classes at reg. level *: (i) sparse tree layer)</i>
13. Herbaceous Cover, closed-open <i>(Examples of sub-classes at regional level* : (i) natural, (ii) pasture, (iii) sparse trees or shrubs)</i>
14. Sparse Herbaceous or sparse Shrub Cover
15. Regularly flooded Shrub and/or Herbaceous Cover
16. Cultivated and managed areas <i>(Examples of sub-classes at reg. level* : (i) terrestrial; (ii) aquatic (=flooded during cultivation), and under terrestrial: (iii) tree crop & shrubs (perennial), (iv) herbaceous crops (annual), non-irrigated, (v) herbaceous crops (annual), irrigated)</i>
17. Mosaic: Cropland / Tree Cover / Other natural vegetation
18. Mosaic: Cropland / Shrub or Grass Cover
19. Bare Areas
20. Water Bodies (natural & artificial)
21. Snow and Ice (natural & artificial)
22. Artificial surfaces and associated areas

Figure 44: Global Land Cover 2000 detailed biome definition.

A detailed study of commission/omission errors for each biome type is in progress. However, the first analyses show similar trends on all biomes with more detections for SLSTR than MODIS sensors for every biome. These detection disparities are accentuated for night-time FRP products.

 <p>OPT-MPC Optical Mission Performance Cluster</p>	<p>Optical MPC</p> <p>Data Quality Report – Sentinel-3 SLSTR</p> <p>March 2023</p>	<p>Ref.: OMPC.ACR.DQR.04.03-2023</p> <p>Issue: 1.1</p> <p>Date: 14/04/2023</p> <p>Page: 70</p>
---	---	--

8 Appendix A

All Data Quality Reports, as well as past years Data Quality Reports and Annual Performance Reports, are available on dedicated pages in Sentinel Online website, at:

- ❖ <https://sentinel.esa.int/web/sentinel/technical-guides/sentinel-2-msi/data-quality-reports>
- ❖ <https://sentinel.esa.int/web/sentinel/technical-guides/sentinel-3-olci/data-quality-reports>
- ❖ <https://sentinel.esa.int/web/sentinel/technical-guides/sentinel-3-slstr/data-quality-reports>
- ❖ [OPT Annual Performance Report Year 2022 \(PDF document\)](#)

End of document